Title

Targeting Ferroptosis as a Novel Therapeutic Strategy for Combating Cancer

Author

Hendricks, Joseph Michael

Publication Date

2023

Peer reviewed|Thesis/dissertation

Targeting Ferroptosis as a Novel Therapeutic Strategy for Combating Cancer

By

Joseph Hendricks

A dissertation submitted in partial satisfaction of the

requirements for the degree of

Doctor of Philosophy

in

Metabolic Biology

in the

Graduate Division

of the

University of California, Berkeley

Committee in charge:

Professor James Olzmann, Chair
Professor Roberto Zoncu
Professor Daniel Nomura

Fall 2023

Abstract

Targeting Ferroptosis as a Novel Therapeutic Strategy for Combating Cancer

By

Joseph Hendricks

Doctor of Philosophy in Metabolic Biology

University of California, Berkeley

Professor James Olzmann, Chair

Cancer is a leading cause of death worldwide and has propensity for rapid mutation, which constantly challenges our ability to treat aggressive forms. There is an unmet need for next generation cancer medicine capable of overcoming chemotherapeutic resistance in cancer. Ferroptosis is a form of regulated cell death that is caused by the iron-dependent peroxidation of lipids[1,2]. The glutathione-dependent lipid hydroperoxidase glutathione peroxidase 4 (GPX4) prevents ferroptosis by converting lipid hydroperoxides into non-toxic lipid alcohols[3,4]. Ferroptosis has been implicated in the cell death that underlies several degenerative conditions[2], and induction of ferroptosis by inhibition of GPX4 has emerged as a therapeutic strategy to trigger cancer cell death[5]. However, sensitivity to GPX4 inhibitors varies greatly across cancer cell lines[6], suggesting that additional factors govern resistance to ferroptosis.

Here in this dissertation, we employ a synthetic lethal CRISPR/Cas9 screen, and we identify ferroptosis suppressor protein 1 (FSP1) (previously known as apoptosis-inducing factor mitochondrial 2 (AIFM2)) as a potent ferroptosis resistance factor. Our data indicate that myristoylation recruits FSP1 to the plasma membrane where it functions as an oxidoreductase that reduces coenzyme Q10 (CoQ), generating a lipophilic radical-trapping antioxidant that halts the propagation of lipid peroxides. We further find that FSP1 expression positively correlates with ferroptosis resistance across hundreds of cancer cell lines, and that FSP1 mediates resistance to ferroptosis in lung cancer cells in culture and in mouse tumor xenografts. Thus, our data identify FSP1 as a key component of a non-mitochondrial CoQ antioxidant system that acts in parallel to the canonical glutathione-based GPX4 pathway. These findings define a new ferroptosis suppression pathway and indicate that pharmacological inhibition of FSP1 may provide an effective strategy to sensitize cancer cells to ferroptosis-inducing chemotherapeutics.

In addition, we screened more than 120,000 compounds using an in vitro FSP1 activity assay and identified 168 compounds that directly inhibit FSP1 oxidoreductase activity. We further characterized 19 FSP1 inhibitors, belonging to 7 structurally distinct groups, and find that these compounds exhibit synthetic lethality with loss of GPX4 in H460 lung cancer cells. The most potent of these FSP1 inhibitors, ferroptosis sensitizer 1 (FSEN1),

acts specifically through inhibition of FSP1 to sensitize cancer cells of different tissue origins to ferroptosis induced by multiple compounds targeting the GSH-GPX4 pathway. Together, our results define several structurally unique FSP1 inhibitors that sensitize cancer cells to ferroptosis, providing tools for the study of FSP1 biology and enabling further exploration of the potential of FSP1 as a therapeutic target.

Dedication

This dissertation is dedicated to my brother Andrew, my mother Denise, my father Chris and to my grandmother Dorothy.

Table of Contents

List of Figures

Tables

Acknowledgments

Many thanks go to my mentor and adviser, Dr. James Olzmann. Thank you for pushing me to strive forward, achieve excellent science goals and for always being a voice of reason. Being able to learn from you and discover new biology along the way has been an honor and an incredibly rewarding experience. I am truly grateful for your mentorship and guidance over the years. Thank you for providing me a space to grow in your lab and to explore / pursue new ideas. Thank you for seeing something I had a difficult time seeing in myself. I appreciate you for always seeing potential in me. In addition, thank you for keeping me on track, for listening to my ideas, helping me shape them and allowing me a space to bring them into reality. You have set a high standard for the kind of scientist, mentor, and leader I aspire to be. I will always be grateful.

I would also like to express gratitude to my qualifying exam committee members: Dr. Dan Nomura, Dr. Roberto Zoncu, Dr. Sarah Stanley, and Dr. Andreas Stahl. Thank you all for your continued support – it was an honor to learn from you.

Thank you to the Department of Nutritional Sciences and Toxicology and the Metabolic Biology Program faculty and staff. Thank you to René Castellanos and Carlos Muñoz for always going above and beyond to help. Many thanks to the UC Cancer Research Coordinating Committee (CRCC) and Bakar Spark fellowship for funding my research, I greatly appreciate this support.

Thank you to the incredible scientists who contributed to the research in this dissertation: my current and former lab mates Breanna Ford, Kirill Bersuker, Zhipeng Li, Kirandeep Deol, Mike Lange, Cody Doubravsky, Eddie Wehri, Julia Schaletzky, Mel Roberts, Irene Lasheras-Otero; and many others who shared reagents, advice, and ideas along the way.

Many thanks to my fantastic lab mates (Olzmabots) and the fellow graduate student researchers who helped me grow as a scientist and lab member. You're all some of the best and brightest people I have had the privilege to know. Lab has always been a meditative / constructive place for me and all of you helped enhance my experience there. Special thanks to my lab twin Alyssa. Thank you for all the late-night philosophical conversations we had in lab and in tissue culture. I will always cherish our time in "Alyssa's Aloha" and the "Joe Zone". Milton for being the resident lab therapist and financial advisor. Mel for providing feedback on my grant applications, posters, and presentations and for being someone I can always count on. Clark for being a great lab brother, roommate, helping me become better at rapping and for taking me snowboarding for the first time. Adam Colorado for being an excellent science mentor, my brother, my legal counsel and always being down to mission. Kirill for being my science mentor and showing me the

way. Thank you for pushing me to always be better, teaching me technique, and helping me break through barriers. Zhipeng for being a great science mentor, providing critical feedback, experimental insight and teaching me more about the flow state. Cody for teaching and inspiring me to be better at science, mentoring, and snowboarding, as well as being a great friend. Viana for always bringing positive vibes wherever you go and for being a great friend. Sanjin for being down since day one, mentoring me in the early days, being a great friend, and helping me find my path.

Thank you to all the professors at West Valley College and Skyline College I met along the way. Many of you helped shape the path I am on today and for that I am grateful.

Finally, I'd like to thank skateboarding and all my friends and brothers in San Jose. Thank you all for always having my back and for always being there for me throughout the years we've grown together. You all provided motivation for me to complete this endeavor and taught me how to never give up. I am forever grateful.

Chapter 1:
Cell death and mechanisms of ferroptosis

1.1 Introduction

Living organisms must metabolize a variety of nutrients to maintain cellular homeostasis, providing substrates for the generation of energy and building blocks for the synthesis of cellular macromolecules. In addition, every living organism must eventually die, therefore it should not be a surprise that the biochemistry of metabolism and cell death are intimately intertwined[7,8]. For mammalian cells to survive they critically rely on a continuous source of energy. The energy source can be extrinsic (taken up from the environment), or when necessary, nutrients are provided from autophagic, lysosomal, or proteasomal degradation of cellular components[7]. If cellular energy sources become critically limited, cellular membrane channels become dysfunctional and subject the cell to passive necrosis (which also occurs due to excessive mechanical / physical damage to the plasma membrane)[7]. The focus of this chapter will be from a mammalian-centric view of the interplay between nutrient concentration, metabolic signaling and regulated cell death pathways.

The classical notion of cell death fundamentally defines two types of cell death modalities: apoptosis, which occurs through a regulated / programmed process, and accidental necrosis, which is not regulated[9]. Originally described in 1972 by Kerr, Wylie and Currie[10], apoptosis has been characterized as a genetically, developmentally programmed and regulated form of cell death. In recent decades several forms of regulated non-apoptotic cell death pathways have been uncovered[11–13]. Collectively termed regulated necrosis, the growing insight of these regulated necrotic cell death pathways have provided an opportunity for the development of novel therapeutic strategies in degenerative diseases, inflammatory conditions and cancer[9]. Both apoptosis and regulated necrosis are triggered by the sudden loss of metabolic stability[7,8]. Comprised of a complex arrangement of signals, sensors, transducers and effectors, all of which are influenced by the cell's nutrient status, gradients of nutrient metabolites and the cell's differentiation state, metabolic checkpoints play a crucial role in cell fate[7].

In this dissertation, I primarily focus on an iron dependent, lipid radical generating non-apoptotic form of regulated necrosis termed, ferroptosis[114]. I will discuss the key metabolic pathways of ferroptosis and how they can be therapeutically targeted in preclinical cancer models.

1.2 Forms of regulated cell death

1.2.1 Apoptosis: Programmed cell death

The term apoptosis describes a characteristic morphology of cell death observed in both developing and adult animal tissues as well as in pathological settings. This phenotype of cell death involves cellular shrinkage, nuclear condensation with DNA fragmentation, and packaging of cytoplasmic contents into individual membrane-bound vesicles, referred to as apoptotic bodies, which shed from the surface of dying cells[10,15]. Nearby cells recognize the budding apoptotic bodies and engulf them in a non-inflammatory process[16].

Apoptosis is organized into extrinsic and intrinsic programs[17] (Figure 1-1). Initiation of the extrinsic program occurs when a specific subset of transmembrane receptors become activated. These transmembrane receptors are known as “death receptors” and include members of the tumor necrosis factor (TNF) receptor gene family[18]. TNF receptor family members share similar cysteine-rich extracellular domains and have a cytoplasmic domain of about 80 amino acids deemed the “death domain”[19]. The death domain plays a critical role in transmission of the death signal from the cell surface to downstream intracellular signaling pathways. In addition to TNF death receptors, several distinct well-known ligands and their corresponding death receptors have been identified and characterized (Table 1)[19–23].

Initiation of the intrinsic program occurs through a diverse array of non-receptor-mediated stimuli. Upon initiation, intracellular signals act directly on targets within the cell and are mitochondrial-initiated events[17]. Downstream signaling of initiating stimuli are described as either positive or negative signaling. Negative signaling occurs in the absence of certain growth factors, hormones, and cytokines, leading to a failure in the suppression of death programs. Positive signaling occurs when the cell is exposed to radiation, toxins, hypoxia, hyperthermia, viral infections, and free radicals. All of these stimuli cause changes in the inner mitochondrial membrane resulting in an opening of the mitochondrial permeability transition (MPT) pore, subsequent loss of mitochondrial transmembrane potential and release of two main groups of pro-apoptotic proteins from the intermembrane space of mitochondria into the cytosol[24]. The first group consists of cytochrome c, Smac/DIABLO, and the serine protease HtrA2[25–28]. These proteins, once released into the cytosol lead to an activation of executioner caspases eventually triggering apoptosis. For example, cytochrome c leaked from mitochondria binds and activates Apaf-1 as well as procaspase-9, forming an “apoptosome”[29,30] (Figure 1-1). The apoptosome will then activate caspase-9, which leads to the activation of caspase-3, 6, and 7.

The execution pathway:
The extrinsic and intrinsic pathways both end at the point of the execution phase, considered to be the final and last stage of apoptosis. Execution caspases activate cytoplasmic endonucleases and proteases that degrade the nuclear and cytoskeletal proteins. Caspase-3, caspase-6, and caspase-7 function as effector proteins or “executioner caspases”, cleaving various substrates including cytokeratins, PARP, plasma membrane cytoskeletal proteins such as α-fodrin, and the nuclear protein NuMA, as well as many other key proteins, (Figure 1-1). This phase of apoptosis ultimately causes the morphologically and biochemically changes observed in apoptotic cells[31].

The key point to take away from this is that programed cell death is initiated by the execution of genomic encoded cellular machinery that activates upon specific stimuli (i.e., death receptor activation and stress signals). A critically defining feature is that the governing machinery of apoptosis can be altered by targeted perturbation of the downstream stimulus, for example, inhibition of executioner caspases will prevent apoptosis induction[17]. As one can infer, apoptosis is both a programed and regulated cell death pathway. Due to the nature of this paradigm, apoptosis is a critical cell death

pathway activated during organism development and homeostasis of tissues in biological systems even in the absence of exogenous stress signals aimed at inducing cell death.

Accidental cell death on the contrary, is necrotic in nature, specifically it is induced by physical and mechanical stresses that result in cellular disintegration and membrane disruption[32]. Therefore, accidental cell death is not regulated by specific genetically encoded biological programs. This type of cell death cannot be modulated or prevented by targeted inhibition of downstream machinery despite exposure to the lethal stimulus. The uncontrolled nature of accidental cell death, for example during traumatic injuries, completely blindsides cellular machinery. In addition to local toxicity from extracellular materials, immunogenic reactions are initiated as the cellular microenvironment responds to the damaging intracellular materials leaked from injured tissue.

1.2.2 Regulated necrosis

Here I will only focus on two types of regulated necrosis, which are relevant to this dissertation.

Necroptosis:

Necroptosis is a regulated form of cell death triggered by infectious disease and is independent of caspases[33]. Interestingly, necroptosis seems to act as a secondary strategy for cell death induction, because it can occur in conditions when apoptosis is inhibited. However, unlike apoptosis, late stage necroptosis involves the release of cytokines and damage-associated molecular patterns (DAMPs), ultimately acting as a pro-inflammatory pathway[34]. As previously mentioned, TNF superfamily receptors such as TNFR1 transmit a cell death signal upon ligand binding through a conserved cytosolic death domain. The first evidence of death receptor induced necroptosis was reported in 2000 by Holler et al. In this research paper, an alternate caspase-8-independent cell death pathway utilizing the kinase RIP (RIPK1) as an effector protein when the TNF death receptor FAS is activated was discovered[35]. However, the term “Necroptosis” was coined in 2005 by Degterev et al, and in this study, a novel compound was identified, Necrostatin-1 (Nec-1), which blocks the ability of the kinase RIPK1 to induce necroptosis in TNF-α treated cells. The discovery of Nec-1 helped introduce a paradigm where necroptosis is defined as a regulated type of necrosis rather than an accidental form of cell death. Since the initial discovery and characterization of RIPK1 in necroptosis, additional machinery has been uncovered, these include two downstream core components RIPK3 and MLKL[36].

The major physiological role of necroptosis is thought to be a secondary cell death process specifically functioning as an activator of an innate immune response due to the presence of bacterial and viral components through a Toll-like receptor (TLR) – TIR domain-containing adaptor inducing interferon β (TRIF) signaling cascade[37] (Figure 1-2). There are also several other additional ways to trigger necroptosis. For instance, if specific apoptotic machinery (cIAP1/2 and caspase-8) are genetically or chemically perturbed and RIPK1/3 are activated by TNFR1 or other death receptors such as TLR3

or ZBP1 (upon dsDNA recognition), a hetero-amyloid structure emerges termed the necrosome (Figure 1-2). The TLR-TRIF signaling cascade induces necroptosis when viral RNAs binding to TLR3 or lipopolysaccharide (LPS) binding to TLR4 activates recruitment of TRIF to the TIR domain of TLRs. TRIF then interacts with RIPK3, which undergoes an autophosphorylation event. This event activates MLKL oligomerization via phosphorylation and subsequent plasma membrane localization[38] (Figure 1-2). The necrosome forms by RIPK1/3, RIP homotypic interaction motif (RHIM) domain interactions, and downstream RIPK3-mediated phosphorylation of the mixed lineage kinase domain-like (MLKL) necroptotic executioner kinase, triggering oligomerization of MLKL and membrane localization[39,40]. Membrane association of this complex leads to plasma membrane damage and the release of DAMPs[39] (Figure 1-2).

Ferroptosis:

Ferroptosis is the primary focus of this dissertation and as of 2012 is considered a form of regulated necrosis[41].

Ferroptosis is an iron dependent and oxidative form of cell death, governed by converging pathways, which are thought to have evolved to mitigate phospholipid membrane damage[1,3,42–44]. Cell death by ferroptosis is unique because it does not share features present in apoptotic, necroptotic or accidental cell death modalities. Specifically, several morphological features characteristic of apoptosis (e.g. chromatin condensation and membrane blebbing), autophagic death (e.g. cytoplasmic vacuolization), or hydrogen peroxide induced necrosis (e.g. organelle swelling)[1,45,46] are absent in ferroptosis. Consistent with this, ferroptosis cannot be circumvented by pan-caspase inhibitors (which inhibit apoptosis), or small molecule inhibitors of autophagy[1,45,46] or necroptosis[47]. More specifically, genetic and or pharmacological perturbation of cyclophilin D, a mitochondrial peptidyl-prolyl cis-trans isomerase critical in controlling mitochondrial permeability transition pore (mPTP)-dependent regulated necrosis, necrosome formation and necroptosis[41,45] does not prevent ferroptosis induction. Supporting the notion that ferroptosis is distinct from other forms of regulated necrosis because it cannot be rescued by targeting downstream effectors in other forms of cell death.

Ferroptosis has only one defining morphological feature which involves ultrastructural modifications of mitochondria, including decreased organelle size and increases in membrane density[1]. At a biochemical scale, heightened concentrations of intracellular labile iron and the catalysis of lipid peroxidation are necessary events for ferroptosis induction[1,3,48]. Ferroptosis is defined by the accumulation of lipid peroxides to toxic levels, which eventually disrupt the structural integrity of the plasma membrane and triggers osmolytic processes that cause the cell to rupture[49]. Cell death by ferroptosis is inhibited by lipophilic radical-trapping antioxidants and iron chelation treatments in tissue culture and in vivo mouse models[48]. This specific modulatory profile is unique to ferroptosis, not only among non-oxidative cell death modalities, but also within oxidative forms of cell death[1]. Intriguingly, reactive oxygen species (ROS)-inducing stimuli most often lead to generation of mitochondrial ROS[50] and ROS in ferroptosis appear to originate from non-mitochondrial and lipid-localized sources[1]. Furthermore, non-ferroptotic ROS-inducers

can be suppressed by hydrophilic antioxidants but are not suppressed by lipophilic antioxidants[1]. This is also true of iron-dependent oxidative cell death forms that otherwise appear like ferroptosis, such as lysosomal iron dependent activation of apoptosis[51]. Differences in both the source and localization of reactive iron and subsequent ROS generation in ferroptosis compared to other oxidative modes of cell death has been suggested to be the basis of this specificity[42]. Therefore, a pair of simple criteria have been defined – suppression by lipophilic antioxidants and or iron chelators – yields a remarkably specific and discriminating functional definition of ferroptosis.

1.3 Mechanisms of ferroptosis

1.3.1 Iron regulation

Iron metabolism:

As indicated by its name, iron plays a critical role in ferroptosis induction; the ability of iron chelators to inhibit ferroptosis induction is one of the foundational features of this mode of cell death[1,48]. Iron is an important trace element in the human body and regulates numerous biological processes[52]. Dysregulation of iron storage or of iron distribution can lead to the accumulation of intracellular iron containing molecules that can damage cells, tissues, and organs[53]. Intricate regulatory mechanisms have evolved to tightly control the release and storage of iron to maintain adequate and safe concentrations in the cell. For example, the human lung contains approximately ~0.4-0.9 mg Fe/g dry weight[54,55], which is comparable to the iron content of the liver (0.2-2 mg Fe/g dry weight)[56,57] but considerably less than that of the heart (2-6 mg Fe/g dry weight)[58]. The exact nature, form, and localization of iron in ferroptosis remain poorly understood[59].

Labile (non-protein bound) pools of iron exist within the cytoplasm, mitochondria and lysosomes of cells, but are kept at low and controlled concentrations[59]. Interestingly, this iron unlike iron sequestered within ferritin or other iron-storing complexes, is redox active and is typically hypothesized to be the primary culprit in catalyzing toxic ROS formation via Fenton chemistry[42]. Redox active iron species also are a component of the active site of many enzymes, where it participates in catalytic enzymatic reactions highly analogous to Fenton chemistry[42]. Two important examples are the lipoxygenase family of enzymes, which catalyze lipid peroxidation reactions using iron as a co-factor, and the cytochrome p450 superfamily of enzymes, which are responsible for hydroxylation and decarboxylation of fatty acids, among other metabolic reactions[59,60]. In addition, the nuclear receptor coactivator 4 (NCOA4) functions as an autophagic cargo receptor that mediates the degradation of ferritin iron storage proteins in autophagosomes through a process referred to as ferritinophagy, and been recently recognized as a promising drug target[61]. This process leads to increased release of ferritin bound iron as free redox active iron (Fe^{2+}) into the labile iron pools, ultimately promoting ferroptosis sensitivity (Figure1-3). Models illustrating lipoxygenase-bound iron as a critical iron source for ferroptosis sensitizing conditions is particularly attractive given the known mechanistic connections between lipoxygenase, lipid peroxidation and GPX4-related cell death[62,63]. However, due to the promiscuity iron chelators to free and active-site reactive iron means that current

models of ferroptosis remain ambiguous about the contribution of enzymatic and non-enzymatic iron-catalyzed reactions toward cell death[42].

1.3.2 Lipid metabolism

Polyunsaturated fatty acids (PUFA) are distinctly sensitive to lipid peroxidation due to the bis-allylic arrangement of their multiple double bonds, which permits hydrogen extraction from acyl chains more readily than from saturated or monounsaturated fatty acyl groups[64]. Acyl-coenzyme A (CoA) synthetase long chain family member 4 (ACSL4) and lysophosphatidylcholine acyltransferase 3 (LPCAT3) are major mediators of polyunsaturated fatty acid phospholipid (PUFA-PL) synthesis[65–67]. ACSL4 catalyzes the ligation of free PUFAs, such as arachidonic acids and adrenic acids, with CoA to generate PUFA-CoAs (such as arachidonic acid-CoA or adrenic acid-CoA)[66,67], are subsequently re-esterfied and incorporated into PLs by LPCAT3 to form PUFA-PLs[67] (Figure1-3). Therefore, ACSL4 and LPCAT3 generate the lipid drivers of ferroptosis.

Lipid peroxidation:

The central role of GPX4, the direct target of the ferroptosis inducer molecule (FIN) RSL3, and an indirect target of erastin-class FINs, is to detoxify lipid hydroperoxides, this highlights the importance of lipid peroxidation as a key molecular feature of ferroptosis[1,3,68]. The lipid peroxidation cycle (Figure 1-4) involves lipid radicals generated through hydrogen abstraction from unsaturated fatty acids[69.] These lipid radicals can react with molecular oxygen radicals to form lipid peroxyl radicals that propagate the cycle of hydrogen abstraction from neighboring unsaturated fatty acids in an unrestrained auto-oxidation cycle[70] (Figure 1-4). Additionally, the more stable byproducts 4-hydroxy-2-nonenal (4-HNE) and malondialdehyde (MDA) from this reaction remain to be highly reactive and can continue the cycle[71] (Figure 1-4). Lipid peroxides can decompose into lipid oxyradicals and lipid hydroxyl radicals, while 4-HNE can add to critical thiols and amino groups of macromolecules[71]. Lipid peroxidation is induced by both enzyme-mediated processes (e.g. lipoxygenases) and non-enzymatic (e.g. labile iron-mediated) processes[72]. The chemistry of lipid peroxidation provides a strong underpinning of observations related to ferroptosis[43].

Like GPX4, which detoxifies lipid peroxides into lipid alcohols and water, the ability of lipophilic antioxidants to suppress ferroptosis is rooted in their capacity to quench lipid radical intermediates through the direct reduction of lipid peroxy radicals to lipid peroxides[73], halting the propagation cycle. The production of $\alpha\beta$-unsaturated aldehyde secondary products (4HNE and MDA) of lipid peroxidation also provide a rationale for the ferroptosis-suppressing effects of aldo-keto reductase (AKR) family members, which play a role in the reduction of toxic aldehydes to alcohols[44,74].

1.3.3 Mechanisms of resistance

To date, several signaling and metabolic pathways that influence the mechanisms of ferroptosis resistance have been characterized – 1) the activity of the antioxidant

response element transcription factor NRF2, 2) the transsulfuration pathway, and 3) mechanistic target of rapamycin (mTOR) mediated pathways. The significance of these pathways are likely cell and context dependent regulators of ferroptosis resistance, nonetheless they highlight the plasticity of ferroptosis resistance and sensitivity.

The nuclear factor-erythroid factor 2-related factor 2 (NRF2) is a master regulator of the antioxidant response element and activates transcription of anti-ferroptotic genes[75]. NRF2 mediated protection is altered across cell types and associated tissues. For example, in pancreatic cancer, NRF2 suppresses ferroptosis through the activation of microsomal GSH S-transferase 1 (MGST1)[76], leading to inhibition of ALOX5. On the contrary, NRF2 can drive resistance to ferroptosis by control of labile iron pool concentrations via ferritin cage regulation[75]. In general, the restriction and heightened regulation of the labile iron pool has also been proposed as an anti-ferroptotic mechanism. Iron-sulfur clusters (ISCs) serve as important cofactors in redox maintenance and general iron homeostasis, and the associated regulatory pathways contribute to ferroptosis evasion in cancer cells by decreasing the labile iron pool[77]. The transsulfuration pathway can drive ferroptosis resistance by producing cysteine from methionine, overcoming the depletion of cysteine induced by the inhibition of system xc^-. Hayano et al, demonstrated that erastin-induced ferroptosis is suppressed through activation of the transsulfuration pathway via siRNA knockdown of cysteinyl-tRNA synthetase (CARS)[78]. The transsulfuration pathway metabolite homocysteine has also been reported to enhance ferroptosis induction rather than drive resistance to ferroptosis when supplemented in methionine depleted cell culture medium[79]. However, further experimental evidence showed homocysteine supplementation was more associated with apoptosis rather than ferroptosis. This suggests that homocysteine can act independently regardless of serving as a source of cysteine, and perhaps represents an area warranting further research to explore crosstalk between simultaneous induction of apoptosis and ferroptosis.

The mTOR pathway promotes ferroptotic resistance by increasing GPX4 protein synthesis[80] and through increasing sterol response element binding protein (SREBP)-mediated lipogenesis[81]. Stearoyl-CoA desaturase-1 (SCD1), is a transcriptional target of SREBP1 and is responsible for generating monounsaturated fatty acids (MUFAs) during lipogenesis, thereby shifting lipid profiles in the cell to be more concentrated in MUFAs, which are known to drive ferroptosis resistance[82].

Cancer cell suppression of PUFA-PL synthesis and peroxidation has also been proposed as a mechanism of resistance. Downregulation of machinery involved in the peroxidation of PUFA-PL levels in cancer cells has been linked to ferroptosis evasion and enhanced tumor growth[83]. The calcium-independent phospholipase A2B (iPLA2β), is a member of the iPLA2 family, and is overexpressed in some human melanoma and osteosarcoma cell lines[84]. iPLA2β depletion has been shown to sensitize cancer cells to ferroptosis and impair xenograft tumor growth[84,85], supporting a model where iPLA2β facilitates cancer cell escape from ferroptosis by hydrolyzing peroxidized PLs. In another study, it was revealed that the expression of the adipokine chemerin, which is frequently upregulated in renal cell carcinoma (RCC), may maintain xenograft RCC growth through suppression

of fatty acid oxidation through activation of hypoxia-inducible factor 2α (HIF-2α) and therefore promotes ferroptosis evasion[86].

Cancer cells are quite tenacious and evade ferroptosis induction through many mechanisms. Ferroptosis resistance can emerge through the modulation of iron homeostasis, ROS abundance, amino acid concentration, and lipid metabolism. The upregulation of cellular antioxidant systems that directly quench lipid peroxides or lipid peroxide radical generation have been deemed as the major mechanisms governing ferroptosis resistance[87–90].

The SLC7A11-GPX4-GSH axis:

Reduced glutathione (GSH) is a thiol-containing tripeptide derived from glycine, glutamate, and cysteine, with cysteine being the rate-limiting precursor[91,92]. Most cancer cells obtain intracellular cysteine primarily through the transporter subunit of system xc^-. System xc^- uptakes cystine, an oxidized dimeric form of cysteine, followed by cystine reduction to cysteine in the cytosol[44,93,94] (Figure 1-3). Solute carrier family 7 member 11 (SLC7A11; also known as xCT) is the transporter subunit in system xc^-[94,95]. Removing cystine from culture media or pharmacologically blocking SLC7A11-mediated cystine transport with small molecules like erastin, imidazole ketone erastin (IKE) or other FINs induces potent ferroptosis in many cancer cell lines[1,95–97].

The SLC7A11-GSH-GPX4 axis is thought to be the major cellular system defending against ferroptosis (Figure 1-3). However, upon GPX4 inactivation, some cancer cell lines remain resistant against ferroptosis[98], suggesting the existence of additional ferroptosis defense systems. GPX4 belongs to the GPX protein family of enzymes and is the only GPX currently known to convert phospholipid hydroperoxides into non-toxic phospholipid alcohols[68,99,100]. There are three main isoforms of GPX4, all with distinctive subcellular localizations, specifically cytosolic, mitochondrial and nuclear GPX4[68]. The three isoforms are encoded by the same GPX4 gene with different transcription initiation sites, resulting in the addition of a mitochondrial or nuclear localization sequence to the N-terminus of the GPX4 protein[68,101–104]. Early studies suggested that only the cytosolic GPX4 was important in preventing ferroptosis, because genetic ablation impacts mouse embryonic development, whereas the mitochondrial and nuclear isoforms are not required for embryonic development[105–109].

GPX4 contains an active site selenocysteine (SEC) residue (U46)[4], coded at an opal (UGA) stop codon. Selenoproteins like GPX4, are subject to a specific form of translational regulation that involves transactivating factors bound to a selenocysteine insertion sequence (SECIS) of the 3' untranslated region of the transcript, which allow for recruitment of Sec-$tRNA^{Sec}$. Recent evidence identified the lipoprotein receptor LRP8 (also known as ApoER2) as a ferroptosis resistance factor[110]. Mechanistically, LRP8 mediates the uptake of selenium into the cell, thereby influencing the abundance of a subgroup of selenoproteins. GPX4 levels rapidly decrease in selenium depleted media due to ribosomal stalling, ribosomal collisions, and early translation termination[110]. These

findings support the existence of a selenoprotein regulatory hierarchy in cancer cells and present a unique therapeutic vulnerability that can sensitize cancer cells to ferroptosis.

FSP1-$CoQH_2$ axis:

After the initial discovery and characterization of ferroptosis in 2012 and 2014, it was thought that GPX4 was the only ferroptosis defense system, however this paradigm shifted 2019 when two groups employing complementary genetic screening strategies[89,90] identified ferroptosis suppressor protein 1 (FSP1) (also known as AIFM2) as a ferroptosis resistance factor. Mechanistically, FSP1 functions as an NAD(P)H-dependent oxidoreductase capable of reducing ubiquinone (also known as coenzyme Q, coenzyme Q10 or CoQ)[104,111] to ubiquinol ($CoQH_2$)[89,90] (Figure 1-3). Through this oxidoreductase activity, FSP1 re-generates lipophilic antioxidants, which subsequently donate a hydrogen to lipid radicals or peroxyl radicals to inhibit the propagation of lipid peroxidation[89,90,112,113] (Figure 1-3). FSP1 is co-translationally, and irreversibly lipidated with myristate at glycine-2 after the removal of the initiator methionine[89,90]. Upon myristoylation, FSP1 localizes to the plasma membrane and lipid droplets[89,90] where the myristate acts as an anchor for membrane entanglement, and is a necessary feature for FSP1 suppression of ferroptosis[89,90]. The mechanisms enabling FSP1 association with specific membranes and dynamic exchange between organelles and degradation mechanisms remains unclear.

Intriguingly, the selective targeting of FSP1 localization to the plasma membrane is sufficient to suppress ferroptosis[89], consistent with the plasma membrane as the primary site of FSP1 action and further highlighting the critical importance of maintaining plasma membrane phospholipid integrity. The current model suggests that FSP1 exerts its potent anti-ferroptosis activity through the regeneration of a non-mitochondrial $CoQH_2$ pool in the plasma membrane as radical-trapping antioxidants[89,90]. CoQ is mainly synthesized in the mitochondria[114] but has been detected in non-mitochondrial membranes including the plasma membrane[115–118]. The first substrate of FSP1 to be identified was CoQ[89,112]. Purified FSP1 reduces oxidized CoQ (i.e., ubiquinone) to hydroquinone form $CoQH_2$ (i.e., ubiquinol) in vitro, at the expense of NAD(P)H, and expression of FSP1 in cells increases the ratio of $CoQH_2$ to CoQ[89,112]. Inhibition of de novo CoQ synthesis sensitizes cells to ferroptosis and deletion of FSP1 under CoQ null conditions does not have any additional effect, highlighting a significant role for CoQ in FSP1-dependent ferroptosis suppression.

The discovery of FSP1 revealed a new anti-ferroptotic mechanism, which involves the local recycling of non-mitochondrial pools of CoQ at the plasma membrane to mitigate oxidative damage to membrane lipids. However, CoQ is highly hydrophobic and how it is transported from the mitochondria to other organelles and membranes remains poorly understood. Researchers recently identified STARD7, which functions as a soluble, cytosolic CoQ binding protein that is important for CoQ trafficking from mitochondria to the plasma membrane[119]. The exact mechanism of how STARD7 mediates this movement of CoQ to specific membranes and if there are additional CoQ transfer proteins involved is unclear. Another protein, UBIAD1, is thought to be involved with the synthesis of non-mitochondrial CoQ pools in the ER and Golgi[120]. However, it has also been

suggested that UBIAD influences CoQ synthesis indirectly through regulation of the mevalonate pathway. Lastly, CoQ contained in circulating lipoproteins may also be a contributing source for FSP1 ferroptosis suppression. However, the intracellular trafficking of CoQ obtained from lipoproteins is also not fully understood.

Since the initial discovery of FSP1 mediated ferroptosis suppression, it has been also shown to reduce other quinone antioxidants including vitamin K, vitamin E, and other quinone molecules[89,90,112,113]. It is currently accepted in the field that these additional antioxidant molecules also contribute to FSP1 ferroptosis resistance in cells. Interestingly, the discovery that FSP1 reduces vitamin K solved a long standing mystery in medicine, identifying the warfarin-resistant oxidoreductase that reduces vitamin K to combat warfarin poisoning[112]. Together, the emerging findings demonstrate that FSP1 acts at specific membranes to locally recycle quinone radical-trapping antioxidants such as CoQ to suppress lipid peroxidation propagation.

GCH1-BH4 axis:

Another critical regulator of ferroptosis has been recently characterized, GTP cyclohydrolase 1 (GCH1)[121,122]. GCH1 mediates the rate-limiting reaction in the tetrahydrobiopterin (BH4) biosynthesis pathway[123] (Figure 1-3). BH4 is a cofactor of aromatic amino acid hydroxylases and other enzymes, and functions as a radical-trapping antioxidant capable of trapping lipid peroxyl radicals. Its function in inhibiting ferroptosis appears to be independent of its role as a cofactor[122]. GCH1 suppresses ferroptosis through the generation of BH4 as a radical-trapping antioxidant and is also able to mediate production of $CoQH_2$ and PLs containing two PUFA tails[121,122].

More research is needed to fully understand the GCH1-BH4 system and any potential therapeutic relevance. For example, the subcellular compartment where GCH1 operates remains to be defined, and whether GCH1 inhibitors will demonstrate effective synergy with other ferroptosis inducing strategies remains to be determined.

1.4 Pathological contexts involving ferroptosis

Ferroptosis has been implicated in many pathologies. It should be noted that the specific cellular and molecular pathophysiological mechanisms triggering ferroptosis and the mechanisms by which ferroptosis causes pathological sequelae (a condition which is the consequence of a previous disease or injury) in several cases remains unclear.

1.4.1 Tumorigenesis

The most frequently mutated tumor suppressor p53[124], has an important role in regulating ferroptosis[96,125]. Specifically, p53 downregulates SLC7A11 expression by directly binding to the SLC7A11 promoter preventing transcription. Additionally, p53 also interacts with ubiquitin-specific processing proteases 7 (USP7) to decrease histone H2B monoubiquitylation levels on the SLC7A11 promoter. This interaction has been shown to

increase cancer cell sensitivity to ferroptosis in an arachidonate 12-lipoxygenase (ALOX12)-dependent manner[96,126–128]. P53 activity has also been linked to ferroptosis promotion through modulating several metabolic targets such as, spermidine/spermine N1-acetyltransferase 1 (SAT1), ferredoxin reductase (FDXR) and glutaminase 2 (GLS2)[129–131]. Interestingly, some mutations in p53 lead to an inability to induce apoptosis, senescence or cell cycle arrest, however, these same mutants are able to promote ferroptosis and mediate tumor suppression in vivo[96]. In contrast, other p53 mutants deficient in ferroptosis regulatory activity also lose their tumor suppression function[131,132]. Intriguingly, this suggests, p53 perhaps plays a dual role in ferroptosis regulation, which is dependent on the cellular context / metabolic profile, as it appears to exert an anti-ferroptosis effect under specific conditions[133,134].

In addition to p53, several other tumor suppressors have been suggested to be involved in ferroptosis regulation. The tumor suppressor BAP1 is a nuclear deubiquitinating enzyme (DUB) that serves to decrease histone H2A ubiquitination (H2Aub) on chromatin[135,136]. Similar to p53, this activity also leads to a decrease in SLC7A11 expression and subsequent promotion of ferroptosis[97]. BAP1 is frequently mutated in several types of cancers, which include uveal melanoma, mesothelioma, and renal cell carcinoma[137], suggesting these cancer types may contain ferroptosis sensitivities. Kelch-like ECH associated protein 1 (KEAP1) is a tumor suppressor often mutated in non-small-cell lung carcinoma[138,139]. KEAP1 functions as a substrate adaptor that targets the transcription factor NRF2 for proteasomal degradation[140,141]. KEAP1 inactivation in cancer leads to NRF2 protein stabilization[140,141]. As a master regulator of antioxidant defense, NRF2 promotes the transcription of many genes governing ferroptosis suppression such as SLC7A11[141–143] and FSP1[144].

While ferroptosis is thought to have tumor-suppression activity, loss of pro-ferroptotic signals is also thought to drive tumorigenesis. A recent study has identified selenocysteine containing proteins as predictors of cancer risk and that selenium is elevated in tumor tissue[145]. This implicates that tumor cells could elevate GPX4 production during tumorigenesis to evade ferroptosis. Lastly, the environment of lymphatic tissues was recently shown to be protective against ferroptosis, for invasive melanoma cells, allowing for increased metastatic spread. In this recent study, it was found that the metastasis of tumor cells through blood subjects the cells to pro-ferroptotic environmental conditions, however, tumor cells travelling through the lymphatic system are protected from ferroptosis, likely due to high levels of oleic acid in lymph[146]. Ultimately, these recent findings suggest a paradigm where genetic and environmental perturbations leading to inactivation of ferroptosis may drive tumorigenesis in various pathological contexts.

1.4.2 Neurodegeneration

Ferroptosis is implicated in a variety of neurodegenerative diseases including Huntington Disease, Alzheimer's Disease, Parkinson's Disease, and amyotrophic lateral sclerosis (ALS)[2]. Recent data support these implications, for instance, GPX4 has been shown to be depleted in post-mortem spinal cords of ALS patients and mouse models, GPX4

overexpression has been shown to extend survival and delay disease onset in the G93A SOD1 model[147,148], and a pre-clinical treatment Cu^{II}(atsm), set to continue phase 2 and phase 3 clinical trials for ALS has been shown to inhibit ferroptosis in primary and immortalized neuronal cell lines[149].

As previously mentioned, glutamate toxicity has been implicated in ferroptosis. In 2001, the term oxytosis was introduced to describe an oxidative cell death in neurons triggered in response to glutamate, which involves protein synthesis, eIF2α, ROS production, cGMP-gated channels, and calcium influx, as well as lipoxygeneases and GSH depletion[150]. The degree of overlap to which mechanisms exercising control over oxytosis and those controlling ferroptosis in various cell types and tissues remains unknown. Although both types of cell death have been shown to involve system xc^- inhibition and GSH depletion, some key features for oxytosis are absent in ferroptosis[151] and include an excess in calcium influx, cGMP-gated channel activities and eIF2α activity, as well as mitochondrial swelling and DNA fragmentation[152]. To further elucidate the distinct features and characteristics shared between oxytosis and ferroptosis, the field of cell death requires a clear set of markers, assays, and reagents for inducing and inhibiting oxytosis and ferroptosis. This would allow for systematic comparisons of the similarities and or differences between the cell death modalities, as well as provide a framework valuable for exploring other modes of cell death[153]. Thus, the degree of overlap to which oxidative glutamate toxicity and/or other mechanisms shared between oxytosis and ferroptosis, remains unclear. It is possible that all these mechanisms are ferroptosis, however more research is needed to define an absolute certainty.

1.5 Therapeutic potential of ferroptosis

The development of potent, selective compounds and biologics capable of modulating ferroptosis sensitivity or resistance, through specific mechanisms is of critical importance. The field needs to continue expanding the set of tools for the reliable detection of ferroptosis and other forms cell death in experimental models[153]. Monitoring lipid peroxidation through a variety of experimental approaches is one means of identifying the presence of ferroptosis; methods of detecting lipid peroxidation include the use of the thiobarbituric acid reactive substances (TBARSs) assay, detection of isoprostanes or lipid peroxidation products directly by LC-MS/MS, oxidation of the C11-BODIPY fluorescent probe, and reactivity with antibodies that detect adducts formed by products of lipid peroxidation, such as with the anti-HNE FerAb antibody[154], the HNEJ-1 antibody[155], and the MDA adduct 1F83 antibody[156]. Additionally, it has been recently reported that increased abundance and plasma localization of TfR1 can be used as a marker for ferroptosis, which is detectable with the 3F3-FMA antibody, as well as with additional anti-TfR1 antibodies[157]. In another recent study, researchers coupled TfR1 staining with machine learning algorithms to distinguish cells undergoing ferroptosis from those undergoing apoptosis[158]. Several genes, which include CHAC1, PTGS2, SLC7A11, and ACSL4, were all upregulated during ferroptosis, while the gene RGS4 was downregulated during ferroptosis. The altered gene expression profiles were detected by qPCR and illustrate a potential approach for accurate ferroptosis diagnostic assays.

These markers can distinguish ferroptosis from apoptosis and necroptosis, however, certain stress events can activate some of these markers in the absence of ferroptosis induction. Therefore, possessing the ability to clearly detect multiple markers that definitively identify ferroptosis induction is going to be an important strategy going forward. For example, detecting markers of lipid peroxidation, TfR1 mobilization, and qPCR of genes known to be altered during ferroptosis collectively represent a means for detecting ferroptosis, while excluding other stress conditions. With these ideas in mind, a definitive criterion for detecting ferroptosis will continue to evolve, as the community's understanding of ferroptosis and the relationships it has related to other biological processes advance.

1.5.1 Therapeutic prevention of ferroptosis in disease

Inhibitors of ferroptosis:

There are several critical defense systems governing ferroptosis induction. Malfunctions in these defense systems may be a targetable underlying factor in certain disease contexts. Therefore potent, and selective therapeutic suppression of ferroptosis may provide a unique opportunity in treating these unique disease manifestations. The process of ferroptosis is driven by peroxidation of specific lipid species, and directly blocking this peroxidation process may be an effective strategy in the treatment of disease. For example, upregulation of GPX4 through selenium supplementation is an indirect means of intervening in ferroptosis. The generation of the substrate lipids for peroxidation through the action of lipid biosynthesis and ACSL4 is a critical control point, and controlling iron availability is also a critical control point. After ferroptosis was discovered, several potential uses of first generation inhibitors of this process were reported: ferrostatin-1 (Fer-1) and liproxstatin were found to inhibit the propagation of lipid peroxidation[159], through a radical-trapping mechanism. They were also shown to be effective in models of glutamate toxicity[1], Huntington Disease[43] premature ventricular leukomalacia[43], kidney injury[43,160] and liver injury[161].

Since the discovery of ferrostatins and liproxstatins, additional inhibitors of ferroptosis have been identified and represent a pool of molecules with therapeutic interest. Interestingly, the hypocholesterolemic drug probucol and its analogs have demonstrated the ability to suppress ferroptosis and to be protective in models of glutamate-induced oxidative cell death[162]. Another molecule, Nec-1, which is a RIPK1 inhibitor that suppresses necroptosis, also has an off-target effect at high concentrations and suppresses ferroptosis. Due to this off-target effect, the Nec-1 analogue Nec-1s, which has higher RIPK1 specificity was identified and is the better inhibitor to use in biological assays[163]. Systemic administration of a blood brain barrier permeable selenopeptide has been shown to suppress ferroptosis during stroke[164]. Lastly, the mitochondrially-targeted nitroxide XJB-5-131 has been shown to suppress both apoptosis and ferroptosis. As well as demonstrated an effective therapeutic strategy in models of traumatic brain injury and Huntington Disease[165]. These examples highlight the importance of driving efforts toward screening existing chemical matter for ferroptosis inhibitors.

1.5.2 Therapeutic induction of ferroptosis in cancer

Inducers and sensitizers of ferroptosis:

Ferroptosis is an attractive cell death modality to develop therapeutics around because it has demonstrated excellent preclinical use in the elimination of problematic cell types, which include cancer cells, inflammatory cells, or activated fibroblasts. It is critical to establish the most vulnerable cell types to induction of ferroptosis. As well as the specific governing mechanisms of induction in one tissue compared to other tissues and if it can be propagated throughout neighboring cell types. Four broad mechanisms have been mechanistically characterized for ferroptosis induction – (1) inhibition of system xc^-, (2) inhibition/degradation/inactivation of GPX4, (3) depletion of reduced CoQ (FSP1 axis), and (4) induction of lipid peroxidation through peroxides, iron, or PUFA overload. Multiple sources have verified that targeted inhibition of system xc^- is a potent mechanism for inducing ferroptosis – multiple structurally distinct small molecule inhibitors of this antiporter, such as erastin, erastin2, sulfasalazine, and glutamate, inhibit system xc^- and trigger ferroptosis (Figure 1-3); furthermore, the depletion of extracellular cystine can also trigger ferroptosis. Like system xc^-, genetic inactivation, chemical perturbation, or degradation of GPX4 induces ferroptosis in multiple cell types. Interestingly, perturbation of CoQ biosynthesis through the inhibition of mevalonate pathway intermediates or inactivation of CoQ oxidoreductases, such as FSP1 have demonstrated a potent ferroptosis synergy in settings where GPX4 is not present or is inhibited through chemical perturbation. Lastly, ferroptosis can be induced by treatment with excess iron, PUFAs, or with endoperoxide containing molecules, such FINO2, which also demonstrate potent synergy when combined with FSP1 inhibition. The lethal effects from ferroptotic lipid peroxidation are mostly or completely suppressed by ferroptosis-specific inhibitors, and markers of other types of cell death are not present during ferroptosis. Making these four mechanisms specific for ferroptosis induction compared to other cell death modalities.

The field of ferroptosis expects there are numerous pathological contexts where the application of that induction will likely be beneficial beyond cancer such as, infectious disease (to clear an infectious pathogen) and fibrosis (demolition of excessive fibrotic tissue). However, to date the most well-studied application thus far is the elimination of various types of cancer cells. FINs are compounds or therapeutic strategies that can trigger ferroptosis in cells and have been categorized into four classes based on their mechanism of action. Class I FINs, include small molecules like erastin and its analogue imidazole ketone erastin (IKE), which inhibit cystine uptake, thereby reducing reduce cysteine and glutathione levels in cells. Class II FINs, block the enzymatic activity of GPX4 and include the small molecules like RSL3, ML162, and ML210. Class III FINs, deplete GPX4 protein and CoQ, and include the molecule FIN56. Class IV FINs, work by oxidizing iron generating radicalized iron intermediates and include small molecules like dihydroartemisinin (DHA) and FINO2. These FINs represent various strategies for inducing ferroptosis in cells, with potential implications for cancer therapy.

FINs such as GPX4 inhibitors and system xc^- inhibitors, have yielded promising preclinical data. For example, a diffuse large B cell lymphoma xenograft was shown to be sensitive

IKE treatment, activated markers of ferroptosis in the tumor xenografts[166]. Genetic knockout of SLC7A11 demonstrated significant benefit in a mouse genetic model of pancreatic cancer, and did not show elevated markers of other cell death modalities beyond ferroptosis[167]. It is possible that additional targets beyond GPX4 and system xc^- in tumor cells exist. Pancreatic cancer cells have been shown to depend on the aspartate aminotransaminase GOT1, and shRNA knockdown of GOT1 sensitized to the pancreatic cancer cells to erastin induced ferroptosis[168]. In addition, it has been shown that NRF2 hyperactivation suppresses ferroptosis in lung tumor spheroids[169].

Beyond their use in specific tumor contexts, synergies between ferroptosis inducers and existing therapeutic strategies like radiotherapy and immunotherapy are starting to be explored. Radiation has been shown to induce ferroptosis, and ferroptosis inducers have been shown to act as radio sensitizers[170,171] as a single agent or in combination with immunotherapy[172]. Epithelial-to-mesenchymal transitioned cancers have been shown to be more susceptible to ferroptosis[98] and cancer resistance to targeted apoptotic agents have been associated with heightened susceptibility to ferroptosis[173]. For example, BRAF amplification can drive sensitivity away from BRAF inhibitors, but in exchange can lead to a ferroptosis vulnerability[174]. In addition, other biomarkers have been suggested such as low levels of transsulfuration metabolites[78], low levels of NADPH[73], susceptibility to photochemical lipid peroxidation[175], absence of PI3K/mTOR pathway activity[81], mutations in the Hippo/Yap pathway[176], expression of the PUFA biosynthesis genes ELOVL5 and FADS1[177], amplification of MDM2/MDMX[178] and clear cell cancer cell morphology[6], have all demonstrated potential use for the selection of patients that are best suitable for ferroptosis-inducing anti-cancer therapies. These studies highlight the importance of pinpointing specific metabolic profiles associated with cancer cell transitions, and the aid of reliable predictive biomarkers where ferroptosis-inducing drugs are most effective.

In this dissertation, I describe the discovery of a novel ferroptosis resistance factor, FSP1 (Chapter 2), and the development of novel small molecule inhibitors of FSP1 that sensitize cells to ferroptosis (Chapter 3).

1.6 Figures

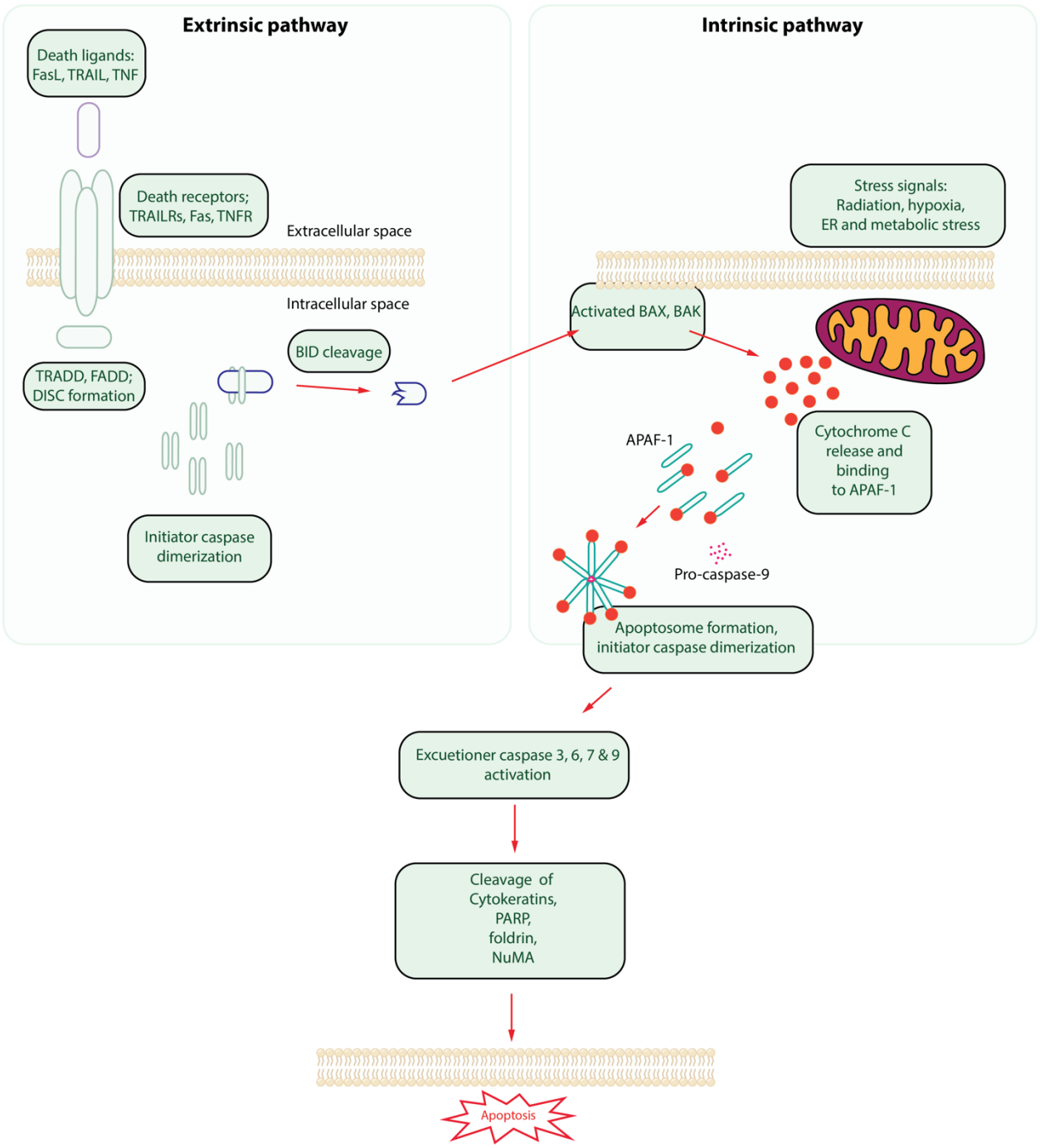

Figure 1-1 Apoptosis

Apoptosis induction via the extrinsic and intrinsic pathways. The extrinsic pathway is activated when pro-apoptotic ligands, such as FasL, TRAIL, and TNF-α bind to their corresponding death receptors and trigger the formation of the death-inducing signaling complex (DISC) in conjunction with initiator caspase dimerization, eventually triggering executioner caspase activation and apoptosis. In contrast, the intrinsic pathway is activated via distinct signal transduction pathways and can be triggered by a variety of cellular stressors (e.g. Radiation, hypoxia, ER and metabolic stress). These cellular

stressors transmit “danger signals” that activate proteins kinases that trigger BAX/BAK oligomerization. The BAX/BAK oligomers localize to the outer mitochondrial membrane where they form pore structures and promote outer membrane permeabilization. This permeabilization leads to the release of Cytochrome C and subsequent binding to APAF-1 to form apoptosome. The apoptosome then activates pro-caspase 9, an initiator caspase, and subsequent executioner caspase activation (caspase 3, 6, 7, and 9). This caspase activity leads to the cleavage and degradation of several host protein components that trigger cell death.

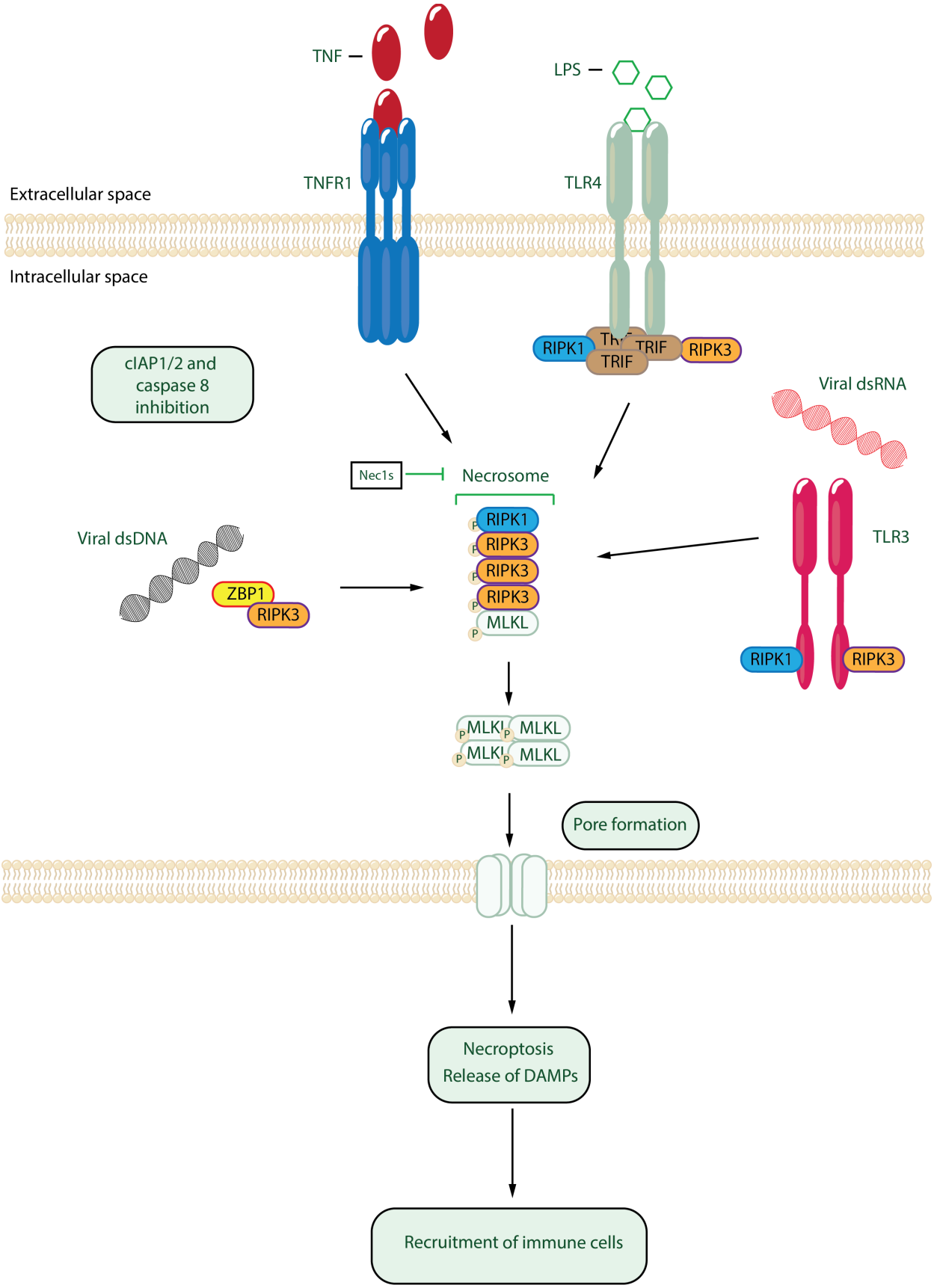
TNF
LPS
TNFR1
TLR4
Extracellular space
Intracellular space
RIPK1
TRIF
RIPK3
cIAP1/2 and caspase 8 inhibition
Viral dsRNA
Nec1s
Necrosome
RIPK1
RIPK3
RIPK3
RIPK3
MLKL
Viral dsDNA
ZBP1
RIPK3
TLR3
RIPK1
RIPK3
MLKL
MLKL
MLKL
MLKL
Pore formation
Necroptosis
Release of DAMPs
Recruitment of immune cells

Figure 1-2 Necroptosis

TNF binding to TNFR1 leads to the formation complex I, in the presence of cIAP1/2 and caspase 8 inhibition. RIPK1 is released from complex I into the cytosol, where it autophosphorylates to become activated and interacts with RIPK3, which is also activated via autophosphorylation. RIPK1 and RIPK3 generate the necrosome. Finally, RIPK3 phosphorylates MLKL, which stimulates pore formation and membrane disruption to execute necroptosis. Viral DNAs can bind to ZBP1, which triggers RIPK3 recruitment and subsequent necrosome formation. Additionally, activation of TLRs also induces necroptosis. Viral RNAs binding TLR3 or lipopolysaccharide (LPS) binding TLR4 recruits TRIF to the TIR domain of the receptor. The TRIF–RIPK3 interaction activates RIPK3 through autophosphorylation and activates MLKL, leading to necroptosis. Small-molecule inhibitors such as Nec1s inhibit necrosome formation and prevent necroptotic cell death.

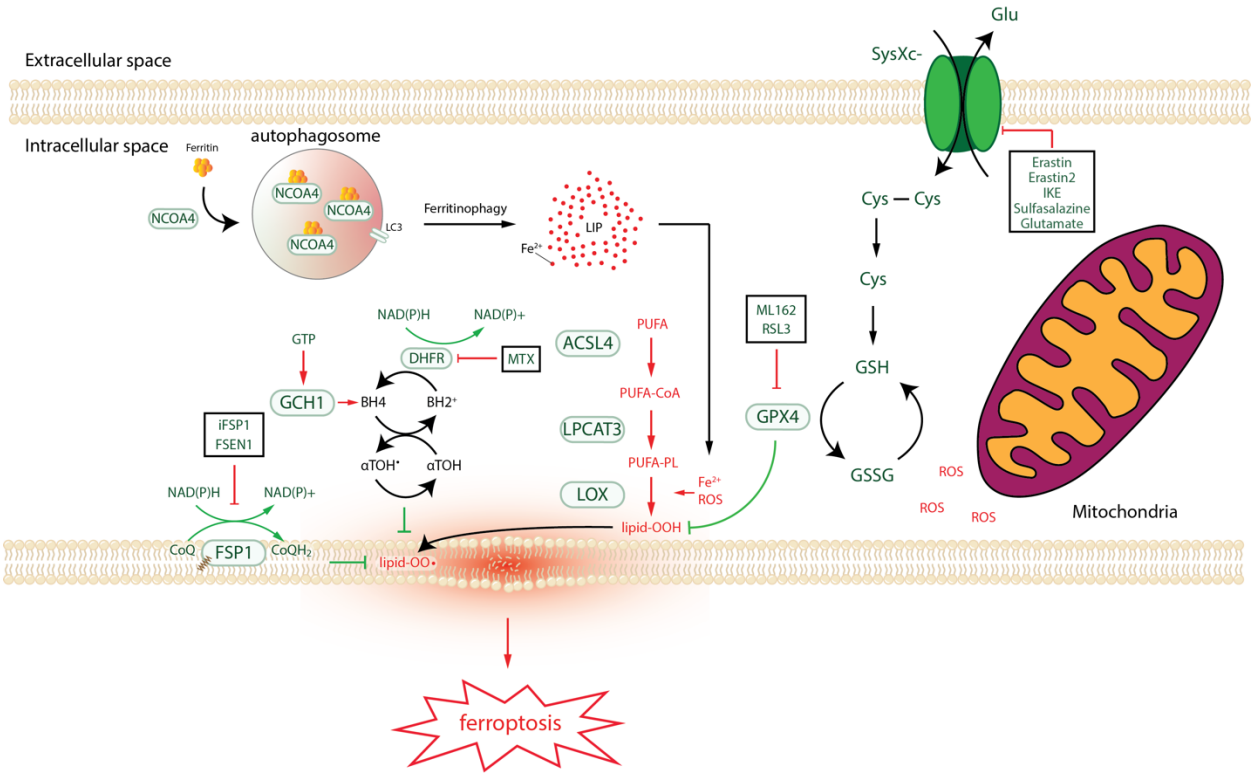

Figure 1-3 Ferroptosis

Excessive accumulation of lipid peroxides on cellular membranes ultimately triggers ferroptosis and cells have evolved at least three defense systems. System xc- imports cystine, which is reduced in the cell to the amino acid cysteine. Cysteine and glutamate are used in the biosynthesis of reduced glutathione, which is in turn used by GPX4 to reduce reactive PUFA phospholipid hydroperoxides (PUFA-PL-OOH) to non-reactive and non-lethal PUFA phospholipid alcohols (PUFA-PL-OH). Small molecule inhibitors such as erastin and IKE inhibit the activity of system xc-. GPX4 is inhibited by the small molecule RSL3. PUFA-PLs are oxidized by labile Fe^{2+} and Fe^{2+}-dependent enzymes such as ALOXs. FSP1-CoQ system operates to regenerate the reduced form of $CoQH_2$, which is used to directly quench radicalized PUFA-PLs in the plasma membrane. FSP1 activity is inhibited by small molecules such as iFSP1 and FSEN1. GCH1-BH_4 system operates to generate tetrahydrobiopterin (BH4) which is used to regenerate the lipophilic antioxidant α-tocopherol, which acts directly to quench radicalized PUFA-PLs in the plasma membrane. GCH1 is inhibited by the small molecule MTX.

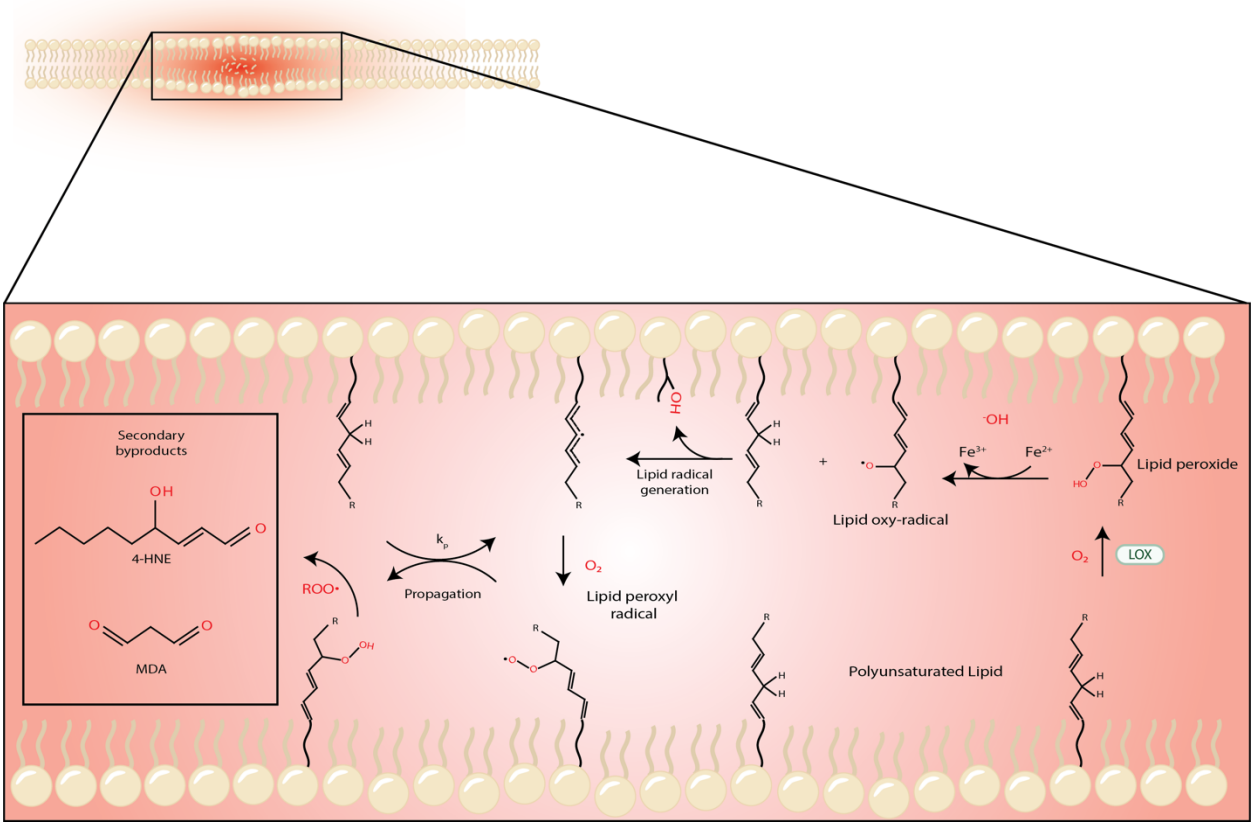

Figure 1-4 Lipid radical auto-oxidation

Starting from right to left; the key steps the of auto-oxidation mechanism, illustrated with a bis-allylic (skipped diene) moiety of a PUFA. Lipoxygenases oxygenate PUFAs both regioselectively and stereoselectively in a three-step mechanism involving hydrogen atom abstraction from the substrate, deoxygenation and hydrogen atom donation to the substrate-derived peroxyl radical. Abstraction of a labile hydrogen atom from the substrate by an initiating radical yield a carbon-centered radical that subsequently reacts with O_2 to yield a peroxyl radical that can propagate the chain reaction by reacting with another molecule of substrate. These propagation reactions compete with termination whereby two peroxyl radicals react to an alcohol, a carbonyl compound and O_2. Initiating radicals can be lipid alkoxyl radicals or hydroxyl radicals derived from one-electron reduction of the hydroperoxide in a Fenton-like reaction. The reductant is a low-valent iron, another redox-active metal ion or another good one-electron donor, iron being the key player in ferroptosis. Alternatively, hydroperoxyl radical (the conjugate acid of superoxide), may serve as an initiating radical. Rate-controlling propagation rate constants (k_p) exist for different PUFAs. In general, increasing the number of C-H bonds of the methylene group flanked by C-C double bonds leads to a corresponding increase in the rate of auto-oxidation of the lipid. Intermediate peroxyl radicals can undergo intramolecular propagation reactions, leading to a wide variety of products however, 4-HNE and MDA are the predominant secondary products can continue the propagation.

Tables

Ligands	Death receptor	Reference
FasL	FasR	Chicheportiche et al., 1997
TNF-α	TNFR1	Ashkenazi et al., 1998
Apo3L	DR3	Peter and Kramer, 1998
Apo2L	DR4	Suliman et al., 2001
Apo2L	DR5	Rubio-Moscardo et al., 2005

Table 1: Table of death ligands and corresponding death receptors

Ferroptosis inducers	Ferroptosis inhibitors	Ferroptosis sensitizers with GPX4 inhibitors
System xc- inhibitors	Lipid peroxidation inhibitors	FSP1 inhibitors
Erastin	Ferrostatin-1	iFSP1
IKE	Tocopherol	FSEN1
Sulfasalazine	DFO	icFSP1
BSO	Idebenone	
GPX4 inhibitors	Tetrahydrobiopterin	
(1S, 3R)-RSL3	Baicalein	
ML210	Ubiquinol ($CoQH_2$)	
FINO2	Liproxstatin-1	
FIN56	UAMC-3203	
	Ciclopirox	

Table 2: Known ferroptosis inducers and inhibitors

Chapter 2:
FSP1 is a CoQ oxidreductase that runs parallel to GPX4 in preventing ferroptosis

Contents in this chapter are modified from the previously published manuscript:

Bersuker K, Hendricks JM, Li Z, *et al.* The CoQ oxidoreductase FSP1 acts parallel to GPX4 to inhibit ferroptosis. Nature. 2019 Nov;575(7784):688-692. doi: 10.1038/s41586-019-1705-2.

2.1 Introduction

In this chapter, I discuss the discovery of a novel ferroptosis resistance factor FSP1 and the key experiments that reveal the molecular mechanisms through which FSP1 prevents ferroptosis.

GPX4 is considered to be the major enzyme responsible for preventing ferroptosis[2]. The resistance of certain cancer cell lines to GPX4 inhibitors[6] led us to search for additional pathways that protect cells against ferroptosis. To identify resistance genes, we used CRISPR/Cas9 technology to screen for genetic deletions that sensitize U-2 OS osteosarcoma cells to the GPX4 inhibitor 1*S*,3*R*-RSL3 (hereafter RSL3) (Figure 2-1A). This screen revealed a significant disenrichment of single guide RNAs (sgRNAs) targeting FSP1 in the RSL3-treated group (Figure 2-1B,C, Figure 2-S1A, Supplementary Table 1[89]), indicating that loss of FSP1 is lethal in combination with RSL3 treatment. FSP1 was originally named AIFM2 based on its homology to apoptosis-inducing factor (AIF or AIFM1), a mitochondrial pro-apoptotic protein[179,180]. However, as reported here, FSP1 lacks the N-terminal mitochondrial targeting sequence in AIF, does not localize to mitochondria, and does not promote apoptosis. Thus, we renamed AIFM2 to FSP1 to reflect its cellular role as described in this study.

2.2 Results

2.2.1 FSP1 is a potent ferroptosis suppressor

Quantification of cell viability using time-lapse microscopy revealed a considerable increase in the sensitivity of FSP1 knockout (FSP1KO) cell lines to RSL3 (Figure 2-1D–F, Figure 2-S1B, Supplementary Table 2[89]), which was rescued by expression of untagged FSP1 (Figure 2-S1C,D). In contrast to previous reports[179,180] the overexpression of FSP1 did not induce apoptosis (Figure 2-S1E, F) and activation of p53 did not increase FSP1 expression (Figure 2-S1G). FSP1KO cells displayed increased sensitivity to additional ferroptosis inducers, including the GPX4 inhibitor ML162 and the system xc− inhibitor erastin2[44] (Figure 2-S1H), but not to the complex I inhibitor rotenone or hydrogen peroxide (Figure 2-S1I–L). The viability of RSL3-treated FSP1KO cells was rescued by the iron chelator deferoxamine (DFO) and by the radical-trapping antioxidants ferrostatin-1 (Fer1) and idebenone (Figure 2-1G), but not by inhibitors of apoptosis (ZVAD(OMe)-FMK) or necroptosis (necrostatin-1) (Figure 2-S1M). Knockout of long-chain acyl-CoA synthetase 4 (ACSL4) in FSP1KO cells (FSP1KO ACSL4KO) restored resistance to RSL3 to an extent similar to that of knockout of ACSL4 alone (ACSL4KO) (Figure 2-1H, Figure 2-S1N), consistent with the requirement for ACSL4-mediated incorporation of PUFAs into phospholipids for ferroptosis[2,5]. Together, these findings demonstrate that FSP1 is a strong suppressor of ferroptosis.

2.2.2 Plasma-membrane FSP1 blocks ferroptosis

FSP1 contains a short N-terminal hydrophobic sequence and a canonical flavin adenine dinucleotide-dependent oxidoreductase domain (Figure 2-S1O). FSP1 has previously

been detected on lipid droplets[181]. To further define the localization of FSP1, we inserted a C-terminal halogenase tag (HaloTag) into the FSP1 genomic locus (Figure 2-2A). Similar to ectopically expressed wild-type FSP1 tagged at the C terminus with green fluorescent protein (FSP1(WT)–GFP) (Figure 2-S2A,B), FSP1–HaloTag localized to the periphery of lipid droplets and to the plasma membrane (Figure 2-2B, Figure 2-S2C, D). FSP1–HaloTag did not co-localize with endoplasmic reticulum labelled with blue fluorescent protein fused to Sec61 (BFP–Sec61) or with mitochondria labelled with MitoTracker (Figure 2-S2G, H), consistent with the absence of an endoplasmic reticulum or mitochondrial targeting motif in FSP1. We noted an N-terminal consensus sequence for myristoylation (Figure 2-2C), a fatty acid modification that is known to function in membrane targeting. FSP1 myristoylation was tested using a click chemistry method that enables affinity purification of myristoylated proteins (Figure 2-S3A). Using this approach, endogenous FSP1 was affinity-purified from buoyant fractions enriched in lipid droplets (Figure 2-S3B) and from whole-cell lysates (Figure 2D). The myristoylation of FSP1(WT)–GFP was blocked by the inhibition of N-myristoyltransferase (NMT), mutation of the glycine-2 of FSP1 to alanine (FSP1(G2A)–GFP) and treatment with the translation inhibitor emetine (Figure 2-2D, Figure 2-S3C). Chemical and genetic perturbations of FSP1 myristoylation blocked FSP1 recruitment to lipid droplets (Figure 2-2E, Figure 2-S3D, E). Although a portion of FSP1(G2A)–GFP was observed in proximity to the plasma membrane by total internal reflection fluorescence (TIRF) microscopy (Figure 2-S2F), the fractionation of organelles in iodixanol (OptiPrep) gradients revealed that FSP1(G2A)–GFP was present at lower levels in fractions enriched in plasma membrane (Figure 2-2F, G, Figure 2-S2I).

Together, these results indicate that the myristoylation of FSP1 mediates the recruitment of this protein to lipid droplets and the plasma membrane. Expression of FSP1(WT)–GFP, but not of FSP1(G2A)–GFP, rescued the resistance of FSP1KO cells to RSL3 (Figure 2-2H, Figure 2-S3F), which indicates that FSP1 must be myristoylated to suppress ferroptosis. We generated fusion proteins that selectively target FSP1(G2A)–GFP to the endoplasmic reticulum (amino acids 100–134 of cytochrome b5; Cb5), the outer mitochondrial membrane (TOM20 signal sequence, TOM20(SS)), lipid droplets (PLIN2) and the plasma membrane (first 11 amino acids of LYN kinase; LYN11) (Figure 2-S4A, B). Only the expression of FSP1 targeted to the plasma membrane (LYN11–FSP1(G2A)–GFP) was sufficient to restore ferroptosis resistance in FSP1KO cells (Figure 2-2I, Figure 2-S4C). By contrast, expression of FSP1(G2A)–GFP targeted to the endoplasmic reticulum, mitochondria or lipid droplets had no effect (Figure 2-2I).

Consistent with previous results in HT1080 cells[82], the depletion of lipid droplets using inhibitors of the diacylglycerol acyltransferase enzymes (DGAT1 and DGAT2) did not affect ferroptosis sensitivity (Figure 2-S5A–C), which provides support for the conclusion that lipid-droplet localization is not required for the FSP1 mediated suppression of ferroptosis. Thus, FSP1 plasma-membrane localization is necessary and sufficient to confer ferroptosis resistance.

2.2.3 FSP1 reduces CoQ to suppress ferroptosis

Under basal conditions, the ratiometric fluorescent lipid peroxidation sensor BODIPY 581/591 C11 exhibited similar levels of oxidation in control and FSP1KO cells (Figure 2-3A, Figure 2-S6A, B). However, a brief treatment with RSL3 strongly increased C11 oxidation in FSP1KO cells relative to control (Figure 2-3A, Figure 2-S6A, B). Glutathione levels were unaffected in FSP1KO cells (Figure 2-S6C–E), indicating that deletion of FSP1 does not inhibit system xc− or glutathione synthesis. FSP1KO cells also did not exhibit higher levels of phospholipids that contain PUFAs (Figure 2-S6F, G, Supplementary Table 3[89]). Levels of phospholipids containing PUFAs were decreased and the corresponding lysophospholipids were increased (Figure 2-S6F, G, Supplementary Table 3[89]), a known lipidomic signature of ferroptosis that reflects the removal of oxidized PUFAs from the sn-2 position of phospholipids[3,182]. These results suggest that the loss of FSP1 results in increased phospholipid oxidation even when GPX4 is functional, and that FSP1 prevents lipid peroxidation through a mechanism that is distinct from glutathione-dependent protective pathways. FSP1 functions as an NADH-dependent CoQ oxidoreductase in vitro[183].

Reduced CoQ can act as a radical-trapping antioxidant, and idebenone—a soluble analogue of CoQ—is sufficient to suppress lipid peroxidation (Figure 2-S7A) and ferroptosis[73] (Figure 2-1G). Previous studies have detected high levels of CoQ in non-mitochondrial compartments, including the plasma membrane[117,184], but the function of this molecule in these compartments remains unclear. To examine the role of FSP1 CoQ oxidoreductase activity in suppressing ferroptosis, we mutated a conserved glutamate residue (E313 in AIF or E156 in FSP1) that is required for the binding of AIF to its cofactor, flavin adenine dinucleotide (Figure 2-S7B, C). Mutation of E156 in FSP1 (FSP1(E156A)–GFP) did not affect FSP1–GFP expression or localization (Figure 2-S3F, Figure 2-S7D, E) but greatly impaired FSP1-mediated reduction of coenzyme Q1 and resazurin in vitro (Figure 2-S7F–H) and abolished the ability of FSP1–GFP to rescue the resistance of FSP1KO cells to RSL3 (Figure 2-3B). Consistent with these findings, the expression of FSP1(WT)–GFP, but not of FSP1(E156A)–GFP, increased the ratio of reduced-to-oxidized CoQ (Figure 2-3C). Acute reduction of cellular CoQ levels by the inhibition of the CoQ biosynthesis enzyme COQ2 with 4-chlorobenzoic acid (4-CBA) strongly sensitized control cells and—to a lesser extent—FSP1KO cells to RSL3-induced ferroptosis (Figure 2-3D, E, Figure 2-S8A). Treatment with 4-CBA also suppressed the ability of FSP1(WT)–GFP to rescue FSP1KO cells (Figure 2-S8B). A similar degree of sensitization to RSL3 was observed after knockout of COQ2 in control, but not in FSP1KO, cells (Figure 2-3F, G, Figure 2-S8C) and COQ2 KO cells exhibited increased C11 oxidation after treatment with RSL3 that was suppressed by DFO and by idebenone (Figure 2-S8D, E).

These data indicate that FSP1 and the CoQ synthesis machinery function in the same pathway to suppress lipid peroxidation and ferroptosis. Deletion of NQO1, a quinone and CoQ oxidoreductase that has previously been proposed to function in ferroptosis[75], did not affect sensitivity to RSL3, but cells that lack both FSP1 and NQO1 (FSP1KO NQO1KO) were more sensitive than FSP1KO cells (Figure 2-S9A–C). NQO1–GFP did not rescue ferroptosis resistance in FSP1KO cells to the same extent as did FSP1–GFP (Figure 2-S9D–G), even when targeted to the plasma membrane (LYN11–NQO1–GFP)

(Figure 2-S9H, I). These results indicate that FSP1 is unique in its ability to suppress ferroptosis through the reduction of CoQ.

2.2.4 FSP1 in cancer ferroptosis resistance

The Cancer Therapeutics Response Portal (CTRP) reports correlations between gene expression and drug resistance for over 800 cancer cell lines[185]. Data mined from the CTRP indicate that FSP1 expression positively correlates with resistance to multiple GPX4 inhibitors (RSL3, ML210 and ML162) (Figure 2-4A, B, Figure 2-S10A, B, Supplementary Table 4[89])—even more so than the system xc− component and erastin target SLC7A119. Thus, FSP1 is a biomarker of ferroptosis resistance in many types of cancer. Consistent with the correlations observed in the CTRP, lung cancer cell lines that express low levels of FSP1 were the most sensitive to RSL3 and cell lines that express high levels of FSP1 were the most resistant (Figure 2-4B, Figure 2-S10C). Knockout of FSP1 in the highly resistant H460 cell line resulted in a notable, approximately 100-fold sensitization to RSL3 (Figure 2-4D, Figure 2-S10D, E) and overexpression of FSP1–GFP in sensitive H1703 and H446 cells increased resistance to RSL3 by about 10–20 fold (Figure 4E, Figure 2-S10F–I).

To examine the possibility that the inhibition of FSP1 could be a clinically relevant approach to sensitize tumors to ferroptosis-activating chemotherapies, we used ferroptosis-resistant H460 lung cancer cells in a preclinical tumor xenograft mouse model. Owing to the poor bioavailability of small-molecule GPX4 inhibitors (such as RSL3), we adopted a recently developed strategy to acutely induce ferroptosis in vivo[98,173] using GPX4 knockout (GPX4KO) cells (Figure 2-S10J). These cell lines were maintained in Fer1-containing medium to prevent the induction of ferroptosis. Fer1 washout had no effect on the viability of the GPX4KO cells but resulted in the rapid death of GPX4KO FSP1KO cells (Figure 2-4F), consistent with our findings that FSP1 compensates for loss of GPX4 activity. Tumor xenografts were generated with GPX4KO and GPX4KO FSP1KO H460 cell lines, and Fer1 was injected daily to allow viable tumors to develop. After tumors were established, Fer1 injections were discontinued in one set of mice to induce ferroptosis. In contrast to the GPX4KO tumors (which continued to increase in size irrespective of Fer1; (Figure 2-S10K), Fer1 withdrawal resulted in a significant reduction in the growth of the GPX4KO FSP1KO tumors (Figure 2-4G). These data demonstrate that FSP1 maintains the growth of H460 lung cancer tumors in vivo when GPX4 is inactivated. To determine whether the growth of FSP1KO tumors can be inhibited by blocking cystine import, we treated H460 cells with IKE, a system xc− inhibitor that can induce ferroptosis in vivo[166]. Although U-2 OS and H460 FSP1KO cells exhibited increased sensitivity to IKE in cell culture (Figure 2-S10I, M), IKE did not inhibit the growth of wild-type H460 and H460 FSP1KO tumor xenografts (Figure 2-S10N, O). Because cells can overcome the effects of cystine depletion through the use of alternative pathways to generate glutathione[78], our results underscore the need for GPX4 inhibitors that are efficacious in vivo.

2.3 Discussion

Ferroptosis has emerged as a potential cause of cell death in degenerative diseases and as a promising strategy to induce the death of cancer cells that are resistant to other therapies[1,2,5]. Our studies and those of a companion paper[90] identify FSP1 as a potent ferroptosis suppressor that operates in parallel to the canonical glutathione-dependent GPX4 pathway. FSP1KO mice are viable and display no obvious mutant phenotypes[186], consistent with the compensatory suppression of lipid peroxidation by GPX4. Mechanistically, our data support a model in which myristoylation targets FSP1 to the plasma membrane where it mediates the NADH-dependent reduction of CoQ, which functions as a radical-trapping antioxidant that suppresses the propagation of lipid peroxides (Figure 2-4H). Our data also reveal that a fundamental role of non-mitochondrial CoQ is to function as an antioxidant that prevents lipid damage, and consequently ferroptosis. Localization of FSP1 at lipid droplets is not required for protection from ferroptosis. One possibility is that the FSP1-mediated regulation of lipophilic radical-trapping antioxidants in lipid droplets is important for the maintenance of lipid quality during prolonged periods of lipid storage, similar to the function of CoQ and tocopherol in preventing the oxidation of circulating lipoprotein particles[187,188].

Finally, our findings indicate that FSP1 expression is important for predicting the efficacy of ferroptosis-inducing drugs in cancers and highlight the potential for FSP1 inhibitors[90] as a strategy to overcome ferroptosis resistance in multiple types of cancer. In Chapter 3, I discuss the development of novel small molecule FSP1 inhibitors that sensitize cancer cells to ferroptosis, which highlights the exciting potential of inducing ferroptosis as a novel therapeutic strategy for combating drug resistant cancer.

2.4 Materials and Methods

2.4.1 Cell lines and culture conditions

U-2 OS T-Rex Flp-In cells, a gift from Dr. Daniel Durocher (The Lunenfeld-Tanenbaum Research Institute), and U-2 OS Tet-ON cells (Clontech) were cultured in DMEM containing 4.5 g/L glucose and L-glutamine (Corning), NCI-H460, NCI-H2291, NCI-H1703 and NCI-H446 cells (ATCC) were cultured in RPMI1640 containing high glucose, L-glutamine and HEPES (ATCC). All media was supplemented with 10% fetal bovine serum (FBS, Thermo Fisher Scientific and Gemini Bio Products) and all lines were grown at 37°C with 5% CO_2.

2.4.2 Generation of doxycycline-inducible cell lines

All U-2 OS expression lines were generated by transfection of U-2 OS T-Rex Flp-In cells with pOG44 Flp-Recombinase plasmid (Thermo Fisher Scientific) and pcDNA5/FRT/TO plasmid at a 9:1 ratio followed by selection in 500 µg/mL hygromycin. H1703 expression lines were generated by infection with pLenti CMV TetR Blast virus (716-1) (Addgene plasmid #17492) and treatment with 8 µg/mL polybrene (Sigma-Aldrich) followed by selection in medium containing 2 µg/mL blasticidin. TetR cells were subsequently infected with pLenti CMV/TO Hygro DEST virus (670-1) (Addgene plasmid #17293) containing the FSP1-GFP fusion construct and were selected in medium containing 250 µg/mL

hygromycin. FSP1-GFP-expressing cells were enriched by fluorescence activated cell sorting of the GFP-positive population.

2.4.3 Generation of CRISPR/Cas9 genome-edited cell lines

U-2 OS FSP1 single knockout lines were generated using CRISPR/Cas9 technology by transfection with pSpCas9(BB)-2A-Puro (PX459), a gift from Feng Zhang (Addgene plasmid #48139), followed by selection in 1 µg/mL puromycin and isolation of individual clones using cloning rings. U-2 OS FSP1/ACSL4 and FSP1/NQO1 double knockout lines were generated by transfecting single FSP1 knockout clonal lines with the respective PX459 plasmids together with pcDNA3.1/Hygro(+) (Thermo Fisher Scientific) at a 20:1 w/w ratio, selection with 500 µg/mL hygromycin, and isolation of individual clones using cloning rings. U-2 OS FSP1-HaloTag knock-in lines were generated by cotransfection of U-2 OS T-Rex Flp-In cells with donor plasmid pUC57 (described below) and PX459 at a 2:1 w/w ratio in media containing 1 µM SCR7 non-homologous end joining (NHEJ) inhibitor for 48 hr, followed by selection with 1 µg/mL puromycin.

H460 FSP1 single knockout lines were generated by infection with lentiCRISPR v2 Blast virus (Addgene plasmid #83489), selection in medium containing 2 µg/mL blasticidin and isolation of single clones using cloning rings. NCI-H460 GPX4 single knockout lines and FSP1/GPX4 double knockout lines were generated by infection with lentiCRISPR v2 hygro virus (Addgene plasmid #98291), selection with 250 µg/mL hygromycin, and isolation of single clones using cloning rings.

2.4.4 Plasmids

Cloning of all expression plasmids and the HaloTag donor plasmid was performed using restriction enzyme-independent fragment insertion by polymerase incomplete primer extension (PIPE)[189]. To generate the FSP1-HaloTag knock-in donor plasmid, 800 base pair homology arms flanking the AIFM2 stop codon were amplified from U-2 OS genomic DNA and inserted 5' and 3' in frame to the linker-TEV-HaloTag sequence in pUC57 (a gift from Robert Tjian, UC Berkeley). The PAM cite corresponding to the sgRNA used to generate the knock-in was subsequently mutated in the Donor sequence using mutagenesis primers to prevent Cas9 cutting of the integrated sequence. FSP1(WT)-GFP was generated by cloning of FSP1-GFP in pDEST47[181] into pcDNA5/FRT/TO, and the FSP1(G2A)-GFP and FSP1(E156A)-GFP were subsequently generated using site-directed mutagenesis. Tom20SS-FSP1(G2A)-GFP and Lyn11-FSP1(G2A)-GFP were generated by insertion of the signal sequence of Tom20 and the first 11 amino acids Lyn kinase, respectively, at the N-terminus of FSP1(G2A)-GFP. FSP1(G2A)-GFP-Plin2 and FSP1(G2A)-GFP-Cb5 were generated by insertion of the full-length sequence for Plin2 and amino acids 100-134 of Cytochrome b5, respectively, at the C-terminus to FSP1(G2A)-GFP. Lyn11-mCherry-FRB was modified from Lyn11-CFP-FRB[190] by replacement of CFP with the sequence for mCherry. BFP-Sec61 and GFP-Sec61 were kind gifts from Gia Voeltz, University of Colorado. FSP1-GFP in pLenti CMV/TO Hygro was generated by insertion of FSP1-GFP into pENTR1A, followed by Gateway recombination cloning (Thermo Fisher Scientific).

Plasmid transfections were performed using Fugene6 (Promega) transfection reagent for U-2 OS cells. Virus was produced by cotransfection of GAG, POL and pLenti expression plasmids at a 1:1:1 w/w/w ratio into HEK293T cells with X-tremeGENE HP (Roche) transfection reagent, and medium containing secreted virus was harvested after 48 hr.

CRISPR guide RNA (sgRNA) sequences targeting FSP1, ACSL4, NQO1 and GPX4 were designed using the online-available CRISPR design tool developed by the Zhang laboratory (http://crispr.mit.edu/). The oligo sequences preceding the protospacer motif were:

Oligo name	Sequence
FSP1 guide 1	5' caccgGAATCGGGAGCTCTGCACG 3'
FSP1 guide 2	5' caccgTCCCGATTCCACCGAGACCT 3'
ACSL4 guide 1	5' caccgTGCAATCATCCATTCGGCCC 3
ACSL4 guide 2	5' caccgTGGTAGTGGACTCACTGCAC 3'
NQO1 guide 1	5' caccgTTTGCAGCACTCACCGACCA 3'
NQO1 guide 2	5' caccgCAGAAGAGCACTGATCGTAC 3'
GPX4 guide	5' caccgAGCCCCGCCGCGATGAGCCT 3'

Nucleotides in lowercase show the overhangs necessary for incorporation of sgRNAs into the BbsI restriction site of vector PX459.

2.4.5 Chemicals and reagents

Reagents used in this study include: 1S-3R-RSL3 (Cayman Chemical), Ferrostatin-1 (Cayman Chemical), idebenone (Cayman Chemical), deferoxamine (Cayman Chemical), (doxycycline (Sigma), erastin2 (also known as compound 35MEW28)[44] (synthesized by Acme, Palo Alto, CA), ML162 (Cayman Chemical), ZVAD(OMe)-FMK (Cayman Chemical), necrostatin-1 (Cayman Chemical), puromycin (Thermo Fisher Scientific), blasticidin (Thermo Fisher Scientific) , BODIPY568-C12 (Thermo Fisher Scientific), BODIPY 493 (Thermo Fisher Scientific), BODIPY 581/591 C11 (Thermo Fisher Scientific), NMT inhibitor DDD85646 (Aobious), 4-CBA (Sigma-Aldrich), OptiPrep (Sigma-Aldrich), SYTOX Green Dead Cell Stain (Thermo Fisher Scientific), MitoTracker Green FM (Thermo Fisher Scientific), MitoTracker Orange CMTMRos (Thermo Fisher Scientific), CellMask Deep Red (Thermo Fisher Scientific), JF549 (kind gift from Luke Lavis, Janelia Research Campus), oleate (Sigma-Aldrich), polybrene (Sigma-Aldrich), myristate (Sigma-Aldrich), YnMyr (Iris Biotech GMBH), AutoDOT (Abgent), DGAT1 inhibitor T863 (Sigma-Aldrich), DGAT2 inhibitor PF-06424439 (Sigma-Aldrich), SCR7 NHEJ inhibitor (Xcess Biosciences, Inc.), TAMRA-Azide-PEG-Biotin (BroadPharm).

2.4.6 Cell death analysis

Cells were plated in triplicate at a density of 2,000-3,000 cells per well in a black 96-well plate (Corning) 48 hr prior to start of imaging. For induced expression of FSP1, 10 ng/ml doxycycline was added to doxycycline-inducible cell lines at the time of plating. After 48 hr, the medium was replaced with fresh medium containing 30 nM SYTOX Green Dead

Cell Stain, doxycycline (if needed) and the indicated drugs. The plates were immediately transferred to an IncuCyte Zoom imaging system (Essen Bioscience) enclosed in an incubator set to 37°C and 5% CO_2. Three images per well were captured in the green and phase channels every 1 or 2 hr over a 48 hr period, and the ratio of SYTOX Green-positive (dead cells) objects to phase objects (total cells) was quantified using Zoom image analysis software (Essen Bioscience). For each treatment condition, the average SYTOX to phase object ratio was plotted against the 48 hr imaging interval, the area under the curve (AUC) was calculated, and AUC was plotted as a function of drug concentration (e.g. RSL3) using Prism (GraphPad). To calculate the EC_{50} values, the AUC curve was fit to a variable slope function comparing drug concentration to response. To quantify death in $NQO1^{KO}$ cells, $NQO1^{KO}$/$FSP1^{KO}$ cells and lung cancer lines, non-normalized SYTOX counts were used to calculate the AUC. To compare cell death between parental lung cell lines, the AUC was normalized to 100%.

For the 4-CBA experiments, cells were treated with vehicle (1% v/v ethanol) or 30 mM 4-CBA during plating. After 48 hr, the media was replaced with fresh media containing 4-CBA and the indicated drugs.

2.4.7 Western blotting

Cells were washed twice with PBS, lysed in 1% SDS, sonicated for 10-30 sec, and boiled for 5 min at 100°C. Protein concentrations were determined using the bicinchoninic acid (BCA) protein assay (Thermo Fisher Scientific), and equal amounts of protein by weight were combined with 1X Laemmli buffer, separated on 4-20% polyacrylamide gradient gels (Bio-Rad Laboratories, Inc.) and transferred onto nitrocellulose membranes (Bio-Rad Laboratories, Inc.). Membranes were washed in PBS with 0.1% Tween-20 (PBST) and blocked in PBST containing 5% (wt/vol) dried milk for 30 min. Membranes were incubated for 24 hr in PBST containing 5% bovine serum albumin (BSA) (Sigma Aldrich) and primary antibodies. After washing with PBST, membranes were incubated with fluorescent secondary antibodies diluted in 5% BSA/PBST at room temperature for 30 min. All immunoblots were imaged on a LI-COR imager (LI-COR Biosciences).

The following blotting reagents and antibodies were used: anti-AIFM2 (Proteintech Group, Inc. and Santa Cruz Biotechnology), anti-α-tubulin (Cell Signaling Technology, Inc.), anti-GPX4 (Cell Signaling Technology, Inc.), ant-ACSL4 (Sigma-Aldrich), anti-GFP (Poteintech Group, Inc.), anti-NQO1 (Proteintech Group, Inc.), anti-GAPDH (EMD Millipore), anti-RAS (Cell Biolabs, Inc.), anti-MDR1 (Cell Signaling Technology, Inc.), IRDye800 conjugated streptavidin (LI-COR Biosciences), anti-rabbit IRDye800 conjugated secondary (LI-COR Biosciences), anti-mouse Alexa Fluor 680 conjugated secondary (Invitrogen).

2.4.8 Fluorescence microscopy

For fluorescence microscopy of PLIN2 and FSP1-GFP in fixed cells, cells grown on coverslips were treated with 200 μM oleate/10% BSA for 24 hr, washed 3X in PBS, fixed for 15 min in PBS containing 4% (wt/vol) paraformaldehyde, and washed again 3X with

PBS. Cells were permeabilized and blocked for 15 min with 1% BSA/PBS containing 0.01% digitonin followed by blocking in 1% BSA/PBS for 15 min. Cells were washed 3X with 1% BSA/PBS and incubated in anti-PLIN2 antibody for 2 hr at room temperature. Cells were washed 3X and incubated for 1 hr in blocking solution containing anti-antibodies conjugated to Alexa Fluor 594 (Thermo Fisher Scientific. Cells were subsequently washed 3X and mounted using Fluoromount G (Southern Biotech). For fluorescence microscopy of membrane localization of FSP-GFP and Lyn-mCherry-FRB, cells were fixed in PBS containing 4% (wt/vol) paraformaldehyde and washed again 3X with PBS prior to imaging.

For live-cell microscopy, cells were grown in 4-well or 8-well Lab-Tek II Chambered Coverglass (Thermo Fisher Scientific). To image LDs, cells were incubated for 24 hr with 1 μM BODIPY-568-C12 (Thermo Fisher Scientific). To image the cell membrane, cells were incubated with 5 μg/mL of CellMask Deep Red for 30 min and the medium was replaced with fresh DMEM/10% FBS without CellMask prior to imaging. To image mitochondria, cells were treated with 100 nM MitoTracker Orange or MitoTracker Green for 15 min and the medium was replaced with fresh DMEM/10% FBS without MitoTracker prior to imaging. For imaging that required prior transfection, cells were transiently transfected with the indicated plasmids in 6-well plates using Fugene6, incubate for 48 hr and seeded in Lab-Tek II chambers prior to imaging. To image FSP1-HaloTag, cells were incubated with 100 nM JF549 dye for 30 min, washed 3X with PBS, and imaged in fresh phenol red-free medium.

Cells were imaged using a Deltavision Elite widefield epifluoresence deconvolution microscope (GE Healthcare) equipped with a 60× oil immersion objective (Olympus) using DAPI, FITC, Tx-Red and Cy5 filters. For live-cell microscopy, cells were imaged in an enclosure heated to 37°C and exposed to a continuous perfusion of a gas mixture containing 5% CO_2, 21% O_2 and 74% N_2 (BioBlend, Praxair). In all cases, a Z-stack of 4-6 μm in total width was acquired that contained 0.2 μm slices for deconvolution using SoftWoRx software (GE Life Sciences). Single deconvolved slices from each channel were analyzed and merged using ImageJ (http://imagej.nih.gov/ij/).

2.4.9 Lipid droplet fractionation

10 15-cm plates of U-2 OS cells stably expressing FSP1-GFP were induced with 10 ng/mL doxycycline for 48 hr. Cells were harvested by scraping into PBS, centrifuged for 10 min at 500 x g, and cell pellets were resuspended for 10 min in cold hypotonic lysis medium (HLM, 20 mM Tris-HCl pH 7.4, 1 mM EDTA) supplemented with 1X cOmplete™, Mini, EDTA-free Protease Inhibitor Cocktail (Sigma-Aldrich). Cells were dounced 80X strokes and lysates were centrifuged at 1000 x g for 10 min. The supernatant was subsequently transferred to Ultra-Clear ultracentrifuge tubes (Beckman-Coulter), diluted to a final concentration of 20% sucrose/HLM, and overlaid by 4 ml of 5% sucrose/HLM followed by 4 ml of HLM. Overlaid samples were centrifuged for 30 min at 15,000 x g in an ultracentrifuge using an SW41 swinging bucket rotor (Beckman-Coulter). Buoyant fractions were isolated using a tube cutter (Beckman-Coulter), additional fractions were pipetted from the top of the sucrose gradient in 1 mL increments, and pellets were

resuspended in 1 mL HLM. 100 µL of 10% SDS was added to each fraction, yielding a final concentration of 1% SDS. Samples were then sonicated for 15 sec and incubated for 10 min at 65°C. Buoyant fractions were additionally incubated at 37°C for 1 hr with sonication every 20 min, followed by a final incubation for 10 min at 65°C.

2.4.10 Plasma membrane fractionation

Plasma membrane subdomains were separated using a continuous OptiPrep gradient as previously described[191]. Briefly, 6 15-cm plates of cells expressing FSP1-GFP were incubated with 10 ng/ml doxycycline for 48 hr and harvested by scraping into PBS, centrifuged for 10 min at 500 x g and resuspended in 1 mL of base buffer (20 mM Tris-HCl pH 7.8, 250 mM sucrose) supplemented with 1 mM $MgCl_2$, 1 mM $CaCl_2$, and 1X cOmplete™, Mini, EDTA-free Protease Inhibitor Cocktail. Cells were passed 40X through a 1.5" 22-gauge needle and centrifuged at 1000 x g for 10 min. The supernatant was retained, and the pellet resuspended in an additional 1 mL base buffer containing 1 mM $MgCl_2$ and 1 mM $CaCl_2$. The resuspended pellet was passed 40X through a 22-guage needle, centrifuged at 1000 x g for 10 min and the supernatant was combined with 1 mL of supernatant from the previous step to make 2 mL total. OptiPrep mixing solution was prepared by combining 60% OptiPrep stock solution with buffer containing 120 mM Tris-HCl pH 7.8, 250 mM sucrose in a 5:1 v/v ratio. OptiPrep mixing solution was combined with 2 mL of sample supernatant from the previous centrifugation steps in a 1:1 v/v ratio to yield 4 mL of a sample containing 25% OptiPrep. This OptiPrep mixed sample was gently pipetted under an 8 mL 5-20% gradient prepared in an UltraClear tube, which was subsequently centrifuged for 90 min at 52,000 x g in a SW41 swinging bucket rotor at 4°C. After centrifugation, individual 0.67 mL fractions were isolated by pipetting from the top of the gradient.

2.4.11 CRISPR/Cas9 synthetic lethal screen

The CRISPR/Cas9 screen was performed as previously described[192–194]. The "Apoptosis and Cancer" sublibrary of sgRNAs[192,193] comprising 31,324 elements, including 29,824 sgRNAs targeting 3,015 genes (~10 sgRNAs per gene) and 1,500 negative control sgRNAs was employed. To generate lentiviral particles, the sublibrary was co-transfected together with 3rd generation lentiviral packaging plasmids (pVSVG, pRSV and pMDL) into HEK293T cells. Medium containing lentivirus was harvested 48 and 72 hr post-transfection, combined, filtered, and then used to infect ~$2.1x10^7$ U-2 OS cells stably expressing Cas9. After 72 hr of growth, infected cells were selected in medium containing 1 µg/mL puromycin until over 90% cells were mCherry positive. Cells were then re-seeded in 500 cm^2 plates (~8×10^6 cells/plate) and recovered in medium lacking puromycin for 24 hr. For the screen, a total of ~3.2×10^7 cells (i.e., ~1000-fold library coverage) were treated with either DMSO or 0.5 µM RSL3 for 5 days. Cells were then trypsinized, collected by centrifugation at 1000 *x* g, washed twice with PBS, and pellets were frozen at -80^{o}C. Genomic DNA was extracted using the QIAamp DNA Blood Maxi Kit (QIAGEN) according to the manufacturer's instructions. sgRNA sequence libraries were prepared from genomic DNA by two rounds of PCR using the Herculase II Fusion DNA Polymerase (Agilent). sgRNA sequences were amplified by the primers oMCB1562 and oMCB1563

then indexed using the Illumina TruSeq LT adaptor sequences AD006 (GCCAAT; DMSO) or AD012 (CTTGTA; RSL-3) for downstream deep sequencing analysis. PCR products were separated on a 2% tris-borate-ethylenediaminetetraacetic acid (TBE)-agarose gel, purified using the QIAquick Gel Extraction Kit (QIAGEN), and assessed for quality using a Fragment Analyzer (Agilent). PCR amplicons from each sample were pooled in a 1:1 ratio based on their concentrations as determined by Qubit Fluorometric Quantification. sgRNA sequences were analyzed by deep sequencing using the primer oMCB1672 on an Illumina MiSeq instrument at the Oklahoma Medical Research Foundation. Sequence reads were aligned to the sgRNA reference library using Bowtie software. For each gene, a gene effect and score (likely maximum effect size and score), and *p*-value were calculated using the casTLE statistical framework as previously described[192–194].

2.4.12 Click chemistry and in-gel fluorescence

To analyze myristoylated proteins in LD-enriched buoyant fractions, 20 15-cm plates of U-2 OS cells were incubated with 100 μM Myristic Acid or 100 μM YnMyr for 48 hr. Buoyant fractions were isolated by sucrose gradient fractionation as described above, combined with 1% SDS, dialyzed into a 0.1% SDS, 1X PBS solution by loading 0.5 mL of the buoyant fraction into a dialysis cassette. A click mixture was prepared by adding reagents in the following order and by vortexing between the addition of each reagent: TAMRA-Azide-PEG-Biotin (BroadPharm) (final concentration 0.1 mM), $CuSO_4$ (final concentration: 1 mM), tris(2-carboxyethyl)phosphine (TCEP) (final concentration: 1 mM), tris(benzyltriazolylmethyl)amine (TBTA) (final concentration: 0.1 mM). 60 μL of click chemistry mixture was then added to the dialyzed samples. The samples were then vortexed and incubated for 1 hr at room temperature. Next, 1 mL ice-cold MeOH and EDTA (final concentration 10 mM) were added to each sample. The samples were briefly vortexed and then stored at -80°C overnight. The samples were centrifuged at 17,000 x g at 4°C for 30 min to pellet precipitated proteins. Pellets were washed twice with 1 mL ice-cold MeOH, dried, and resuspended in 80 μL in PBS containing 1% SDS. Once dissolved, proteins were resuspended in 1X Laemlli loading buffer and analyzed by SDS-PAGE. To visualize proteins by fluorescence, the gel was washed with MilliQ H_2O three times and analyzed using an the ChemiDoc XRS+ Imaging System (Bio-Rad).

To analyze myristoylated proteins in whole cell lysates, U-2 OS cells were incubated 100 μM Myristic Acid or 100 μM YnMyr for 48 hr. After treatment, cells were washed twice with PBS and lysed on ice in buffer containing PBS with 1% SDS and 1 x EDTA-free complete protease inhibitor (Sigma-Aldrich). Equal amounts of sample by weight were diluted to 0.1%/PBS in dialysis cassettes and subjected to click chemistry with TAMRA-Azide-PEG-Biotin as described above.

2.4.13 N-myristoylated protein enrichment and in-gel fluorescence

For enrichment of myristoylated proteins, YnMr-labelled proteins from cell lysate were labelled with TAMRA-Azide-PEG-Biotin using click chemistry as described above. After protein precipitation, the pellet was resuspended in 80 μL of 1% SDS in 1x PBS. Once the pellet was completely dissolved, 65 μL was diluted 10-fold in 0.1% PBST. 15 μL of

Streptavidin Agarose Resin (Thermo Fisher Scientific) were washed 3X with 0.1% PBST. The diluted sample was added to the bead resin and rotated for 3 hr at room temperature. Beads were washed with 5X with 0.1% PBST and bound proteins eluted by boiling for 5 min in 2X Laemlli buffer containing 2 mM biotin.

2.4.14 Lipidomic profiling by liquid chromatography-tandem mass spectrometry

$Cas9^{Ctl}$ and $FSP1^{KO}$ U-2 OS cells (n=4) grown in 10 cm plates were washed twice in PBS, collected by centrifugation at 1000 x g at 4˚C for 5 min, and processed as described previously[186,195]. Internal standards (10 nmol of dodecylglycerol and 10 nmol of pentadecanoic acid) were added and lipids were extracted in a 4 mL solution of 2:1:1 choloroform:methanol:PBS. The organic and aqueous layers were separated by centrifugation at 1000 x g for 5 min. Following the collection of the organic layer, remaining organic material in the aqueous layer was acidified by addition of 0.1% formic acid and re-extracted in 2 mL of chloroform. Extracts were combined, dried down under a stream of nitrogen, and then resolubilized in 120 µL of chloroform prior. 10 µL of sample was analyzed by single reaction monitoring (SRM)-based LC-MS. LC separation was performed using a Luna reverse-phase C5-column and MS analysis was preformed using an Agilent 6400 triple quadrupole (QQQ)-liquid chromatography-mass spectrometry instrument. Metabolites were quantified by integrating the area under the curve and the values were normalized to the internal standards.

2.4.15 Glutathione measurements

The day before the experiment, 200,000 $Cas9^{Ctl}$ or $FSP1^{KO}$ U-2 OS cells/well were seeded into 6-well dishes (Cat# 07-200-83, Corning Life Sciences, Tewksbury, MA). The next day, cells were treated with DMSO (vehicle) or erastin2 (1 µM) for 6 hr or RSL3 (250 nM) for 1 hr. At the end of the treatments, cells were harvested by scraping and prepared for measurement of total intracellular glutathione (GSH+GSSG) using the Cayman Chemical Glutathione Assay Kit (Cat# 703002, Cayman Chemical, Ann Arbor, USA) according to the manufacturer's protocol. The glutathione concentration was calculated using a glutathione standard curve and normalized to total protein level in each sample. Three independent biological replicates were performed for each condition.

2.4.16 BODIPY 581/591 C11 analysis

The day before the experiment, 200,000 $Cas9^{Ctl}$ or $FSP1^{KO}$ U-2 OS cells/well were seeded into 6 well dishes with one 22 mm^2 glass coverslip in each well. The next day, cells were treated with DMSO (vehicle) or RSL3 (250 nM) for 75 minutes. At the end of the time course, the treatment medium was removed and cells were washed once with HBSS. HT-1080 cells were then labelled with 1 mL C11 BODIPY 581/591 (C11, 5 µM) dissolved in HBSS. Cells were incubated at 37 °C for 10 min. After 10 min, the label mixture was removed and 1 mL of fresh HBSS was added to the cells. The cover slip was transferred to a glass microscope slide onto which 25 µL of fresh HBSS had been applied. Confocal imaging and quantification of C11 were performed as described previously[82] and was performed on two independent biological replicates per treatment. Using ImageJ

1.48v (http://imagej.nih.gov/ij/), each nucleus was attributed two regions of interest (ROI), one perinuclear and one plasma membrane-localized. Red and green fluorescence values were quantified for each ROI and background-corrected by measuring the red or green fluorescence in cell-free areas from at least three images and subtracting the background value to calculate the final fluorescence values. The C11 value was calculated as the ratio of the green fluorescence (which indicates oxidized probe) to total (green + red, which indicates total reduced plus oxidized probe) fluorescence.

2.4.17 Tumor xenograft growth studies

Tumor xenografts were established by injection of $GPX4^{KO}$ and $GPX4^{KO}/FPS1^{KO}$ H460 cells into the flank of male C.B17 SCID mice (Taconic Farms) (n=8). Briefly, cells were washed with PBS, trypsinized, and collected in serum-containing medium. Harvested cells were then washed with serum free medium once and resuspended in serum-free medium at a concentration of 2.0×10^4 cells/µL. 100 µL of cells (2×10^6 cells) was injected per animal. Mice were injected intraperitoneally (IP) with Fer1 daily (2 mg/kg) and tumor size was measured using calipers. Fer1 injections were discontinued in one set of mice 5 days after cell injection and tumor size was measured once every 2 days in each mouse for an additional 17 days. All statistical analyses were performed using Prism. Fold change in tumor volume was statistically analyzed using the unpaired, two-way students t-test. Two outliers were identified using the ROUT method and removed from analyses. All animal experiments were conducted in accordance with the guidelines of the Institutional Animal Care and Use Committees (IACUC) of the University of California, Berkeley.

2.4.18 TIRF microscopy

Cells were imaged at room temperature using a Nikon Ti-E inverted microscope (Nikon Instruments) outfitted with a TIRF 60X/1.49 NA oil objective, an Andor Laser Combiner and an electron-multiplying charge-coupled device camera (iXon ULTRA 897BV; Andor Technology). Samples were excited with a 488nm laser line, and emission was collected through a single band-pass filter centered on 510 nm. All images were acquired using iQ3 acquisition software (Andor Technology). The depth of the evanescent field was approx. 150 nm.

2.4.19 CoQ measurements

CoQ measurements were performed as previously described[196]. To simultaneously measure the reduced and oxidized form of CoQ in U-2 OS cells, a cold butylhydroxytoluene (BHT) solution was added to prevent auto-oxidation at the beginning of sample extraction. To each tube containing cells in the frozen state, 100 µL of a cold BHT-in-propanol solution (5 mg/mL) and 600 µL of cold 1-propanol were added. Immediately after this, the mixture was subjected to sonication for 2 min. Then 100 µL of cold ubiquinone-9 solution (2 µg/mL) used as internal standard was added, and the mixture was vortex-mixed for 1 min. It was then centrifuged for 10 min at 3500 rpm and 1°C, and the propanol organic supernatant layer was transferred to an autosampler vial.

100 µL aliquots of the 1-propanol extract were immediately analyzed and the reduced and oxidized CoQ levels were determined using HPLC as previously described.[38] HPLC analysis was performed using an automated Hitachi Chromaster™ system equipped with Model 5110 quaternary pump, Model 5210 autosampler, Model 5310 column oven and ESA CouloChem III detector. The EZChrom Elite® software was used for monitoring output signal and processing result. The analytical column was a 150-mm x 4.6-mm C18 column with 5-*µ*m spherical particles connected to a Security Guard equipped with C18 cartridge (4-mm x 3-mm).

2.4.20 Apoptosis activation assay

Cells grown in 6-cm plates were washed with PBS, trypsinized and centrifuged for 5 min at 500 x g. Cell pellets were resuspended in PBS containing 5% FBS and 5 µM CellEvent™ Caspase-3/7 Green Detection Reagent and were incubated for 30 min at 37°C. Cells were analyzed on a LSRFortessa™ (Becton-Dickinson) flow cytometer, and the raw data was processed using the FlowJo software package (TreeStar). Apoptotic cells were gated using the same FSC threshold across all samples, and FITC fluorescence of the gated populations was determined.

2.4.21 Protein purification and activity assays

Expression vectors were transformed into Rosetta™ DE3 competent cells (EMD Millipore) and LB cultures were inoculated for overnight growth at 37°C while shaking. The following day, the cultures were diluted 1:100 into 500 mL of LB and allowed to grow to OD600 of 0.5, at which point the incubator was set to start cooling to 20°C. The cultures were grown further to an OD600 of 0.7 and induced with 1 mM isopropyl β-D-1-thiogalactopyranoside (IPTG) overnight. Bacterial pellets were resuspended in 2 mL of cold lysis buffer containing 50 mM potassium phosphate, 300 mM KCl, and 30 mM imidazole, supplemented with 1X cOmplete™, Mini, EDTA-free Protease Inhibitor Cocktail. The resuspended cells were sonicated 5X on ice at 50% power for 10 s, with 2 minute incubations on ice in between sonications, and were centrifuged at 20,000 x g for 15 min at 4°C. The supernatant was combined with 200 µL of Ni-NTA agarose beads (Thermo Fisher Scientific) washed 3X with lysis buffer, and the supernatant-bead mixture was rotated for 1 hr at 4°C. The beads were subsequently washed 5X with cold lysis buffer, and bound proteins were eluted by incubating beads for 15 min in 500 uL of cold lysis buffer containing 250 mM imidazole while rotating. The eluted proteins were dialyzed into PBS containing 10% glycerol and snap frozen in liquid N_2. Protein concentration was determined by measuring the absorbance at 280 nm.

To measure NADH oxidation kinetics, recombinant FSP1 was combined with 500 µM NADH and 200 µM coenzyme Q1 in a total volume of 100 µL PBS. A reduction in absorbance at 340 nm, corresponding to NADH oxidation, was determined over the course of 1 hr. To measure resazurin reduction kinetics, recombinant FSP1 was combined with 500 µM NADH and 500 µM resazurin in a total volume of 100 µL PBS. Fluorescence (emission at 590 nm) corresponding to reduced resazurin was determined

over the course of 1 hr. All measurements were taken using a SpectraMax i3 Multi-Mode Platform plate reader (Molecular Devices).

2.4.22 Analysis of CTRP dataset

Data for significant correlations between FSP1 gene expression and resistance to RSL3, ML162, and ML210 was downloaded from the CTRP v2 website. Data for non-hematopoeitic cancer cells was extracted from the v21.data.gex_global_analysis.txt table and plotted using Prism.

2.4.23 Statistical analysis and reproducibility

All figures, including western blots, dose response curves and enzymatic activity assay panels are representative of two biological replicates unless stated otherwise. Images are representative of at least n = 10 imaged cells. P values for pairwise comparisons were calculated using the two tailed t-test. For comparison across multiple experimental groups, P values were calculated using one way ANOVA, and adjusted using Bonferroni correction for multiple comparisons. For Figures 4A,B and 10A,B, the normalized z-scored Pearson correlation coefficients were obtained from CTRP v2 (portals.broadinstitute.org). For xenograft experiments, all mice were randomized following tumor cell injection into treatment groups. Outliers were identified using the Grubbs method and were removed from analyses. To compare between groups of mice in each time point, P values were calculated using the unpaired, two way t-test.

2.5 Figures

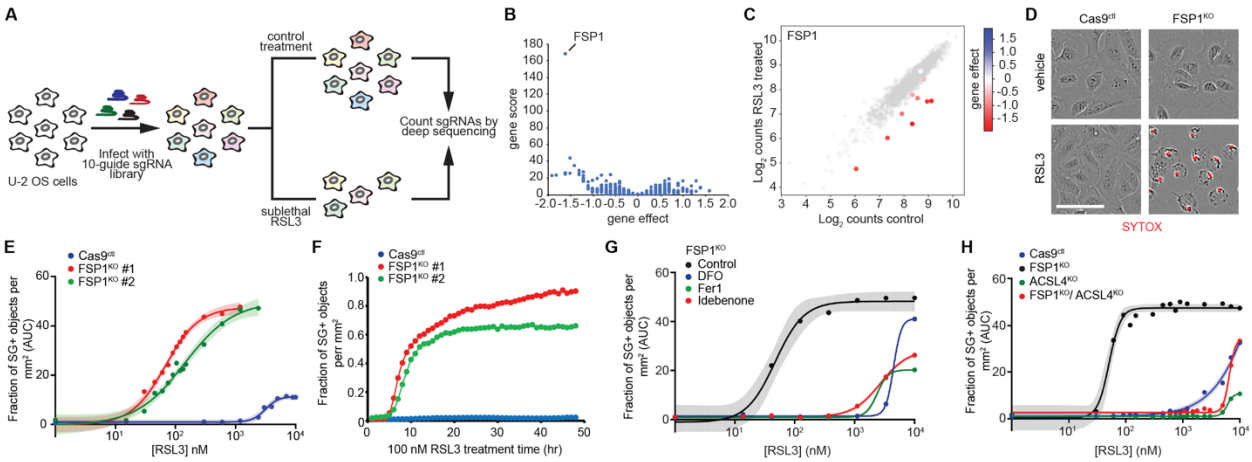

Figure 2-1: A synthetic lethal CRISPR/Cas9 screen identifies FSP1 as a ferroptosis resistance factor

(A). Schematic of the CRISPR/Cas9 screening strategy. (B). Gene effect and gene score calculated for individual genes analyzed in the CRISPR/Cas9 screen. (C). Cloud plot indicating count numbers corresponding to FSP1 (color scale) and control (gray) sgRNAs. The gene effect of individual FSP1 sgRNAs is indicated by the heat map. (D). Live cell imaging of control and FSP1^{KO} cells incubated with SYTOX Green (SG+) and treated with 100 nM RSL3 for 48 hr. Scale bar = 75 μm. (E). Dose response of RSL3-induced cell death of control and FSP1^{KO} cells. (F). Time-lapse cell death analysis of cells treated with 100 nM RSL3 over 48 hr. (G). Dose response of RSL3-induced cell death in the presence of inhibitors of ferroptosis (Fer1: 1 μM, DFO: 100 μM, Idebenone: 10 μM), (H). Dose response analysis of RSL3-induced cell death of the indicated cell lines. ACSL4^{KO} and ACLS4^{KO}/FSP1^{KO} lines shown were generated using ACSL4 sgRNA #1. For figures (E,G,H), shading indicates 95% confidence intervals for the fitted curves and each data point is the average of 3 technical replicates. Panels are representative of 2 biological replicates, except for figures (B,C), which were derived from a single screen.

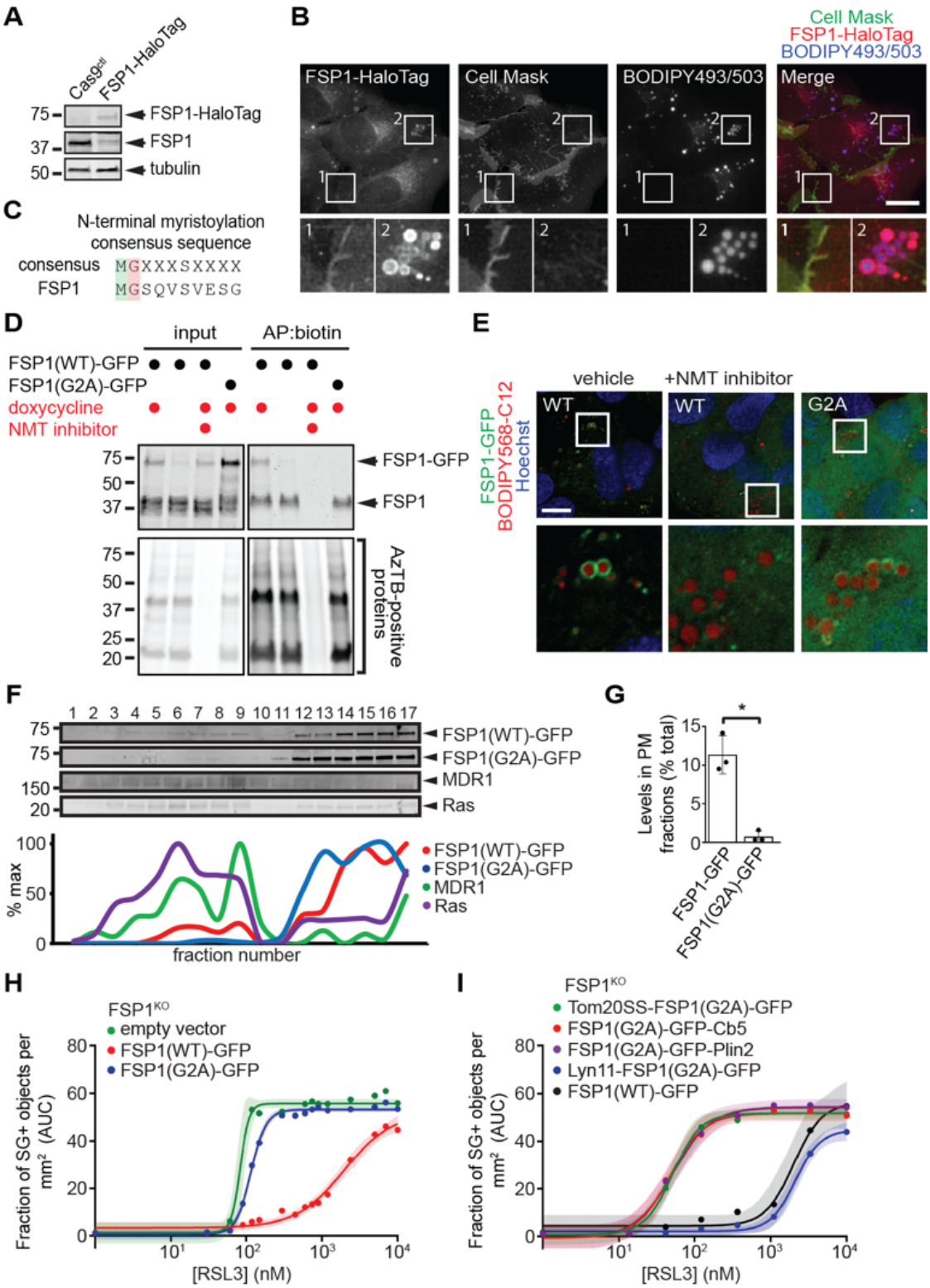

Figure2-2: Myristoylation-dependent recruitment of FSP1 to the plasma membrane promotes ferroptosis resistance

(A), Western blot of lysates from FSP1-HaloTag genomic knock-in cells. (B), FSP1-HaloTag subcellular distribution by live cell microscopy. Cells were incubated with 100

nM JF549 to label FSP1-HaloTag, 5 μg/mL Cell Mask to label the plasma membrane and 1 μg/mL BODIPY 493/503 to label LDs. (C), Consensus myristoylation sequence in FSP1. (D), Analysis of FSP1-GFP myristoylation in whole cell lysates of the indicated cell lines treated for 24 hr with doxycycline to induce FSP1-GFP expression. Where indicated, 10 μM NMT inhibitor was added for 24 hr to inhibit myristoylation. (E),Live cell microscopy of inducible FSP1-GFP cell lines treated with 200 μM oleate and 1 μM BODIPY 558/568 C12. Where indicated, cells were treated concurrently with 10 μM NMT inhibitor. (F), Subcellular fractionation of organelles from cells expressing FSP1-GFP using OptiPrep gradient centrifugation. The densitometry plot shows the distribution of the indicated overexpressed and endogenous proteins. (G), Quantification of FSP1-GFP levels in fractions 1-10 in (F) The graph shows mean ± SD of n = 3 biological replicates. *P = 0.0124 by two-tailed t-test. (H), Dose response of RSL3-induced death of $FSP1^{KO}$ cells pretreated with doxycycline for 48 hr to induce expression of the indicated FSP1-GFP proteins. (I), Dose response of RSL3-induced death of $FSP1^{KO}$ cells expressing the indicated inducible FSP1(G2A)-GFP constructs. For figures (H,I), shading indicates 95% confidence intervals for the fitted curves and each data point is the average of 3 technical replicates. All figures are representative of two biological replicates. Images are representative of at least n = 10 imaged cells. Image scale bars = 10 μm.

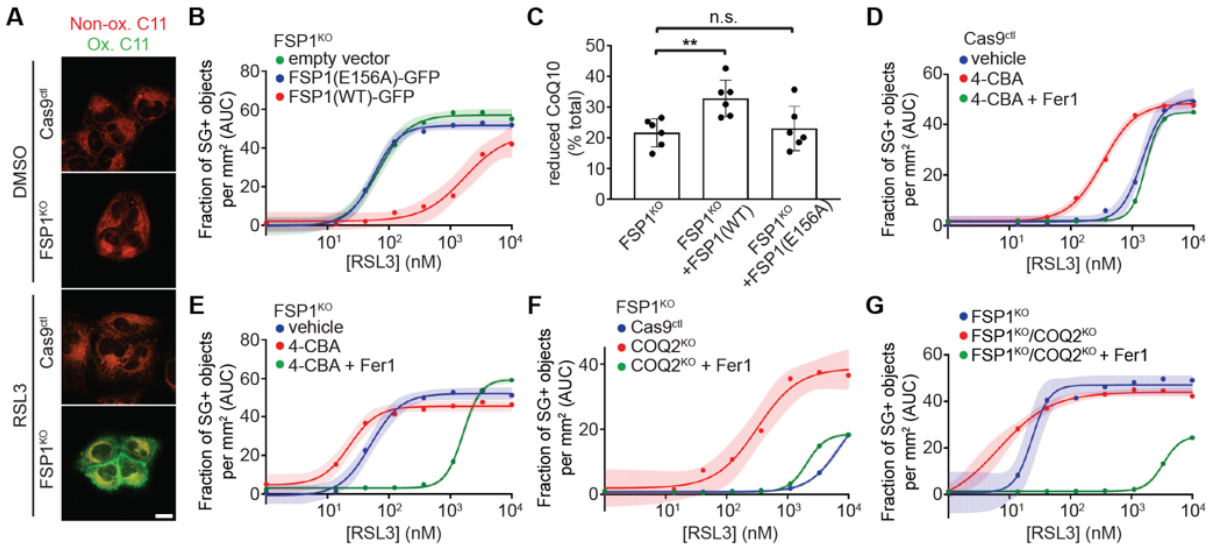

Figure 2-3: FSP1 suppresses lipid peroxidation by reducing CoQ
(A), Control and FSP1^{KO} cells treated with 250 nM RSL3 for 75 min were labeled with BODIPY 581/591 C11 and fixed prior to imaging. Ox. = oxidized; Non-ox. = non-oxidized. Images are representative of at least 30 cells imaged for each treatment condition. Scale bar = 20 μm. (B), Dose response of RSL3-induced cell death of FSP1^{KO} cells expressing the indicated inducible FSP1-GFP constructs. (C), Reduced to oxidized CoQ ratio in FSP1^{KO} and FSP1^{KO} cells expressing the indicated FSP1-GFP constructs. Data represent mean ± SD of n = 6 biological replicates. **P = 0.0178; n.s., P > 0.99 by one-way ANOVA. (D,E), Dose response of RSL3-induced death of control (D) and FSP1^{KO} (E) cells pretreated for 24 hr with 3 mM 4-CBA. (F,G), Dose response of RSL3-induced cell death of COQ2^{KO} (F) and FSP1^{KO}/COQ2^{KO} (G) cells. For figures (B,D-G), shading indicates 95% confidence intervals for the fitted curves and each data point is the average of 3 technical replicates. All figures are representative of two biological replicates.

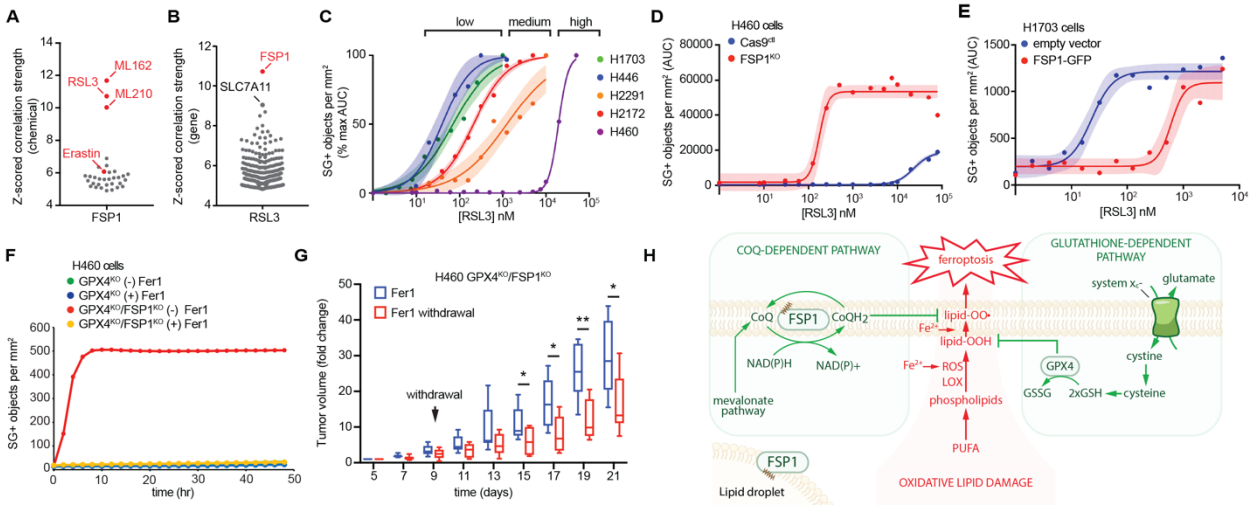

Figure 2-4: FSP1 mediates ferroptosis resistance in lung cancer
(A,B), High expression of FSP1 is correlated with resistance to GPX4 inhibitors in non-hematopoietic cancer cells. Plotted data was mined from the CTRP database that contains correlation coefficients between gene expression and drug sensitivity for 907 cancer cell lines treated with 545 compounds. (A) shows the correlation between FSP1 expression and resistance to individual compounds and (B) shows the correlation between expression levels of individual genes and resistance to RSL3. Plotted values are z-scored Pearson's correlation coefficients. (C), Dose response of RSL3-induced cell death of the indicated cell lines. (D), Dose response of RSL3-induced cell death of control and FSP1^{KO} H460 cells. (E), Dose response of RSL3-induced cell death of FSP1-GFP H1703 cells. (F), Time lapse analysis of cell death of GPX4^{KO} and GPX4^{KO}/FSP1^{KO} H460 cells in the presence and absence of 1 μM Fer1. (G), GPX4^{KO}/FSP1^{KO} H460 tumor xenografts cells were initiated in immune-deficient SCID mice (n = 16). Following 5 days of daily Fer1 injections (2 mg/kg) to allow the cell lines to develop tumors, one set of mice (n = 8) continued to receive daily Fer1 injections and a second set (n = 8) received vehicle injections for the remaining 17 days. The distribution of fold changes in sizes of individual tumors during the treatment is shown. GPX4^{KO}/FSP1^{KO} (−) Fer1, n = 7); GPX4^{KO}/FSP1^{KO} (+) Fer1, n = 8. Box plots indicate median, 25th and 75th percentiles, minima and maxima of the distributions. Day 15, *P = 0.0397; Day 17, *P = 0.0187; Day 18, **P = 0.0025; Day 21, *P = 0.0327 by two-tailed t-test. (H), Model illustrating the mechanism by which FSP1 suppresses ferroptosis. For figures c-e, shading indicates 95% confidence intervals for the fitted curves and each data point is the average of 3 technical replicates. Figures (C-F) are representative of two biological replicates.

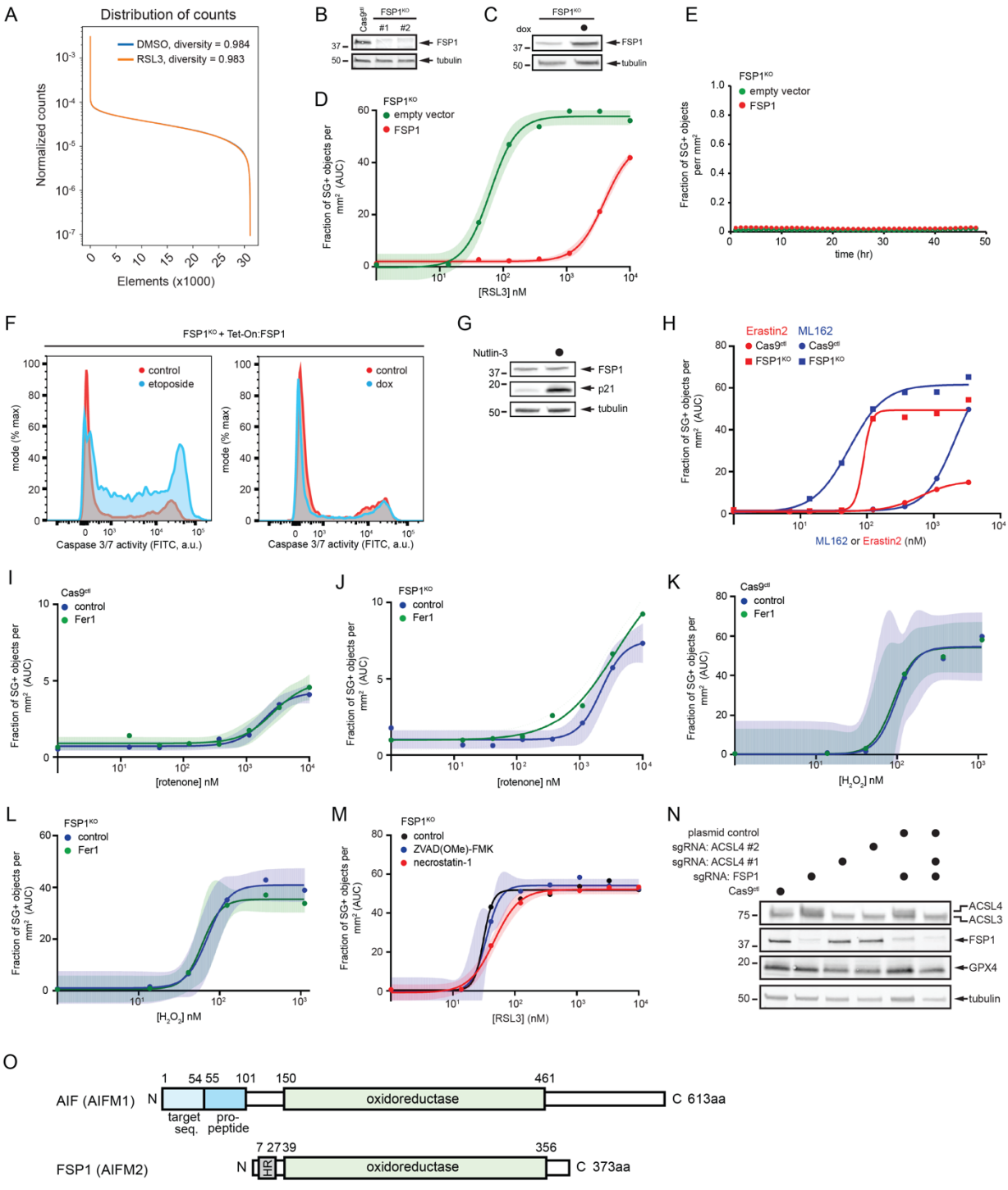

Figure 2-S1: Synthetic lethal screen coverage and validation
(A) Distribution of counts across all sgRNA elements from the CRISPR/Cas9 screen. (B) Western blot of control and FSP1^{KO}cells. (C,D), Western blot analysis (C) and dose response of RSL3-induced death (D) of FSP1^{KO} cells expressing doxycycline-inducible, untagged FSP1. (E) Time-lapse analysis of cell death of FSP1^{KO} cells expressing inducible, untagged FSP1. (F) Flow cytometric analysis of caspase 3/7

activity in FSP1^{KO} cells expressing inducible, untagged FSP1 treated with doxycycline for 48 hr. For a positive control, non-induced cells were treated with 50 μM etoposide for 24 hr prior to analysis. (G) Western blot analysis of lysates from control cells treated with 10 μM Nutlin-3 for 48 hr. (H) Dose response of ML162 and Erastin2-induced cell death. (I,J), Dose response of rotenone-induced death of control (I) and FSP1^{KO} (J) cells. (K,L), Dose response of hydrogen peroxide-induced death of control (K) and FSP1^{KO} (L) cells. (M), Dose response of RSL3-induced cell death in the presence of inhibitors of apoptosis (ZVAD(OMe)-FMK: 10 μM) and necroptosis (necrostatin-1: 1 μM). (N), Western blot analysis of lysates from ACSL4^{KO} and FSP1^{KO}/ACSL4^{KO} cells. (O), Schematic of domains present in AIF and FSP1. For figures d,i-m, shading indicates 95% confidence intervals for the fitted curves and each data point is the average of 3 technical replicates. Figures are representative of two biological replicates except figures (C-E) and (K,L), which show single experiments.

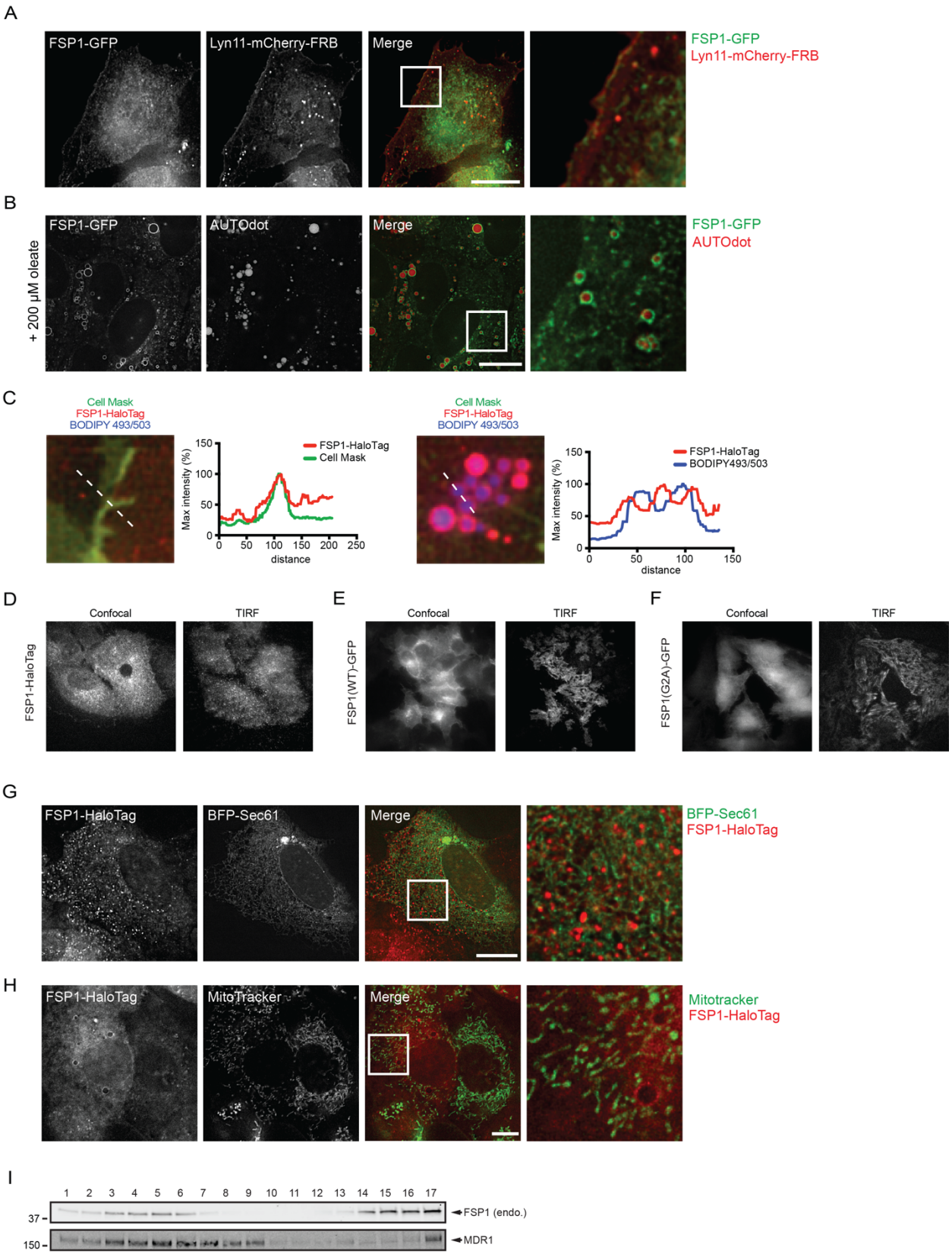

Figure 2-S2: Subcellular distribution of FSP1

(A) Inducible FSP1-GFP cells were transiently transfected with Lyn11-mCherry-FRB for 24 hr, induced with doxycycline for 48 hr and fixed prior to imaging. (B) FSP1-GFP cells were treated with 200 μM oleate for 24 hr to induce LDs and treated with 100 μM AutoDOT to label LDs prior to imaging. (C) Line intensity plots showing colocalization between FSP1-HaloTag and organelle markers. (D-F), Confocal and TIRF microscopy of FSP1-HaloTag (D), and inducible FSP1(WT)-GFP (E) and FSP1(G2A)-GFP (F) cells. (G) FSP1-HaloTag cells were transiently transfected with BFP-Sec61 for 48 hr prior to imaging to label the endoplasmic reticulum. (H) FSP1-HaloTag cells were incubated with 100 nM MitoTracker Green FM to label mitochondria. (I) Plasma membrane subdomains from control cells were enriched by OptiPrep gradient centrifugation. Endo., endogenous FSP1. Western blot is representative of two biological replicates. Images are representative of at least n = 10 imaged cells. Image scale bars = 10 μm.

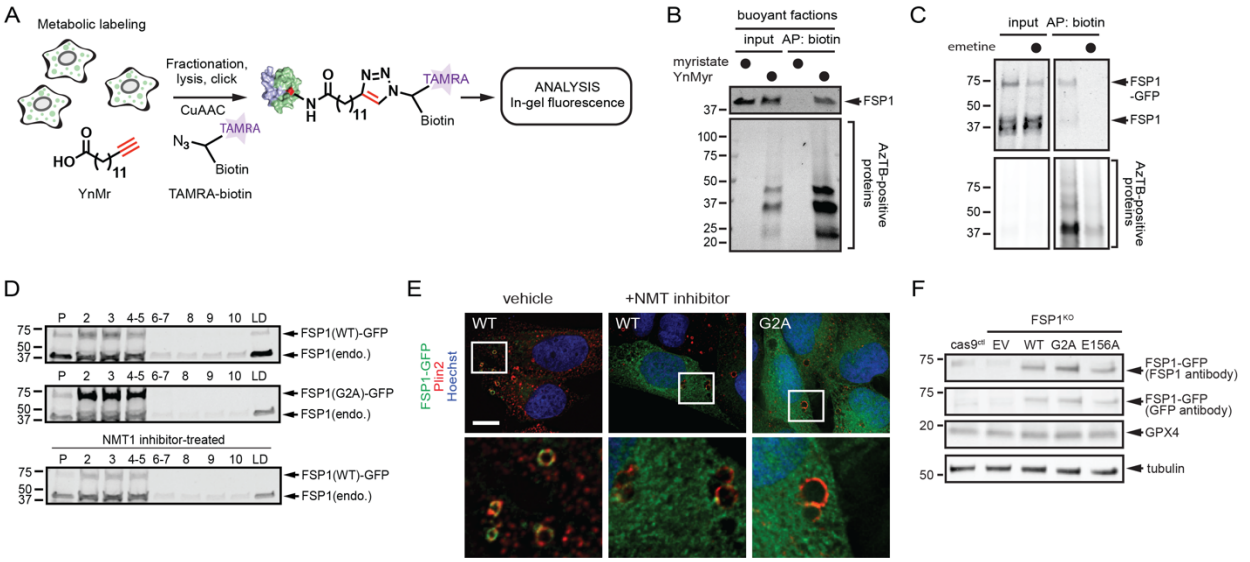

Figure 2-S3: Myristoylation and lipid droplet localization of FSP1

(A) Schematic showing the procedure for metabolic labeling of cells with the myristate-alkyne YnMyr and conjugation of YnMyr-labeled proteins with TAMRA-biotin using click chemistry. (B) Analysis of FSP1 myristoylation in LD-enriched buoyant fractions by streptavidin enrichment of YnMyr-labeled proteins, click chemistry and SDS-PAGE. Cells were treated with 200 μM oleate to induce LDs and with 100 μM YnMyr or 100 μM myristate for 24 hr. (C) FSP1-GFP was induced with doxycycline for 24 hr and cells were incubated with 100 μM YnMyr for an additional 24 hr to label proteins in the presence or absence of 75 μM emetine. YnMyr-labeled proteins were affinity-purified and analyzed by click chemistry and SDS-PAGE. (D) LD-enriched buoyant fractions from cells expressing inducible FSP1-GFP were isolated by sucrose gradient fractionation and analyzed by western blot. Endo., endogenous FSP1. (E) Inducible FSP1-GFP cells were treated with 200 μM oleate in the presence or absence of 10 μM NMT inhibitor, fixed, and stained with anti-PLIN2 antibody prior to imaging. Images are representative of at least n = 10 imaged cells. Scale bar = 10 μm. (F) Western blot analysis of $FSP1^{KO}$ cells induced for 48 hr with doxycycline to express the indicated proteins. All figures are representative of two biological replicates.

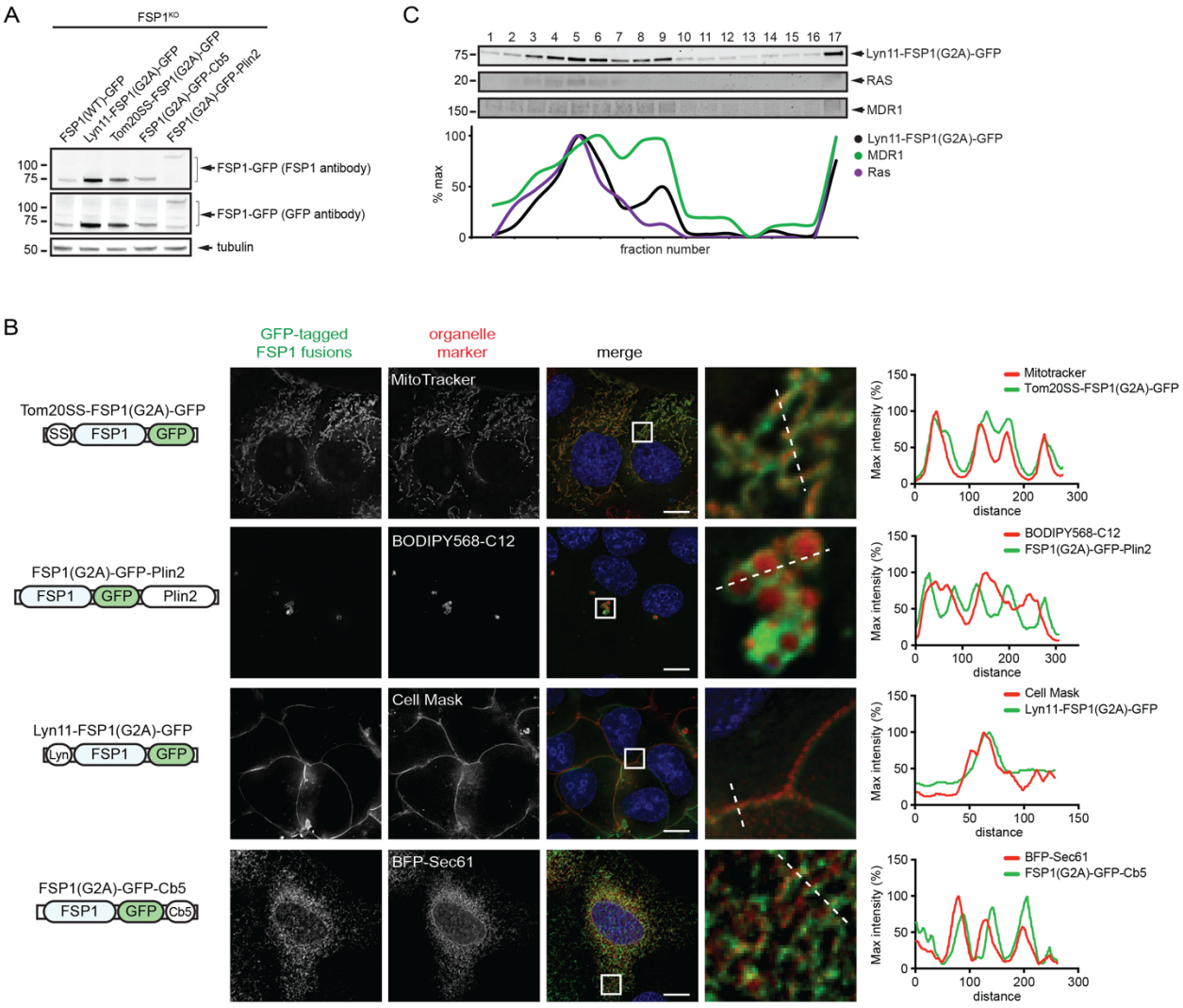

Figure 2-S4: Targeting of FSP1 to subcellular compartments
(A) Western blot analysis of FSP1^{KO} cells induced for 48 hr with doxycycline to express the indicated proteins. (B) Live cell microscopy of cells expressing the indicated FSP1(G2A)-GFP constructs, incubated with 100 nM Mitotracker Orange to label mitochondria, 1 μM BODIPY 558/568 C12 to label LDs or 5 μg/mL Cell Mask to label the plasma membrane. To label the endoplasmic reticulum, cells were transiently transfected with BFP-Sec61 48 hr prior to imaging. Images are representative of at least n = 10 imaged cells. Line intensity plots show colocalization between FSP1 and organelle markers. Scale bar = 10 μm. (C) Plasma membrane subdomains from FSP1^{KO} cells expressing inducible Lyn11-FSP1(G2A)-GFP were enriched by OptiPrep gradient centrifugation. The densitometry plot indicates the distribution of overexpressed and endogenous proteins. Figures are representative of two biological replicates except figure (C), which shows a single experiment.

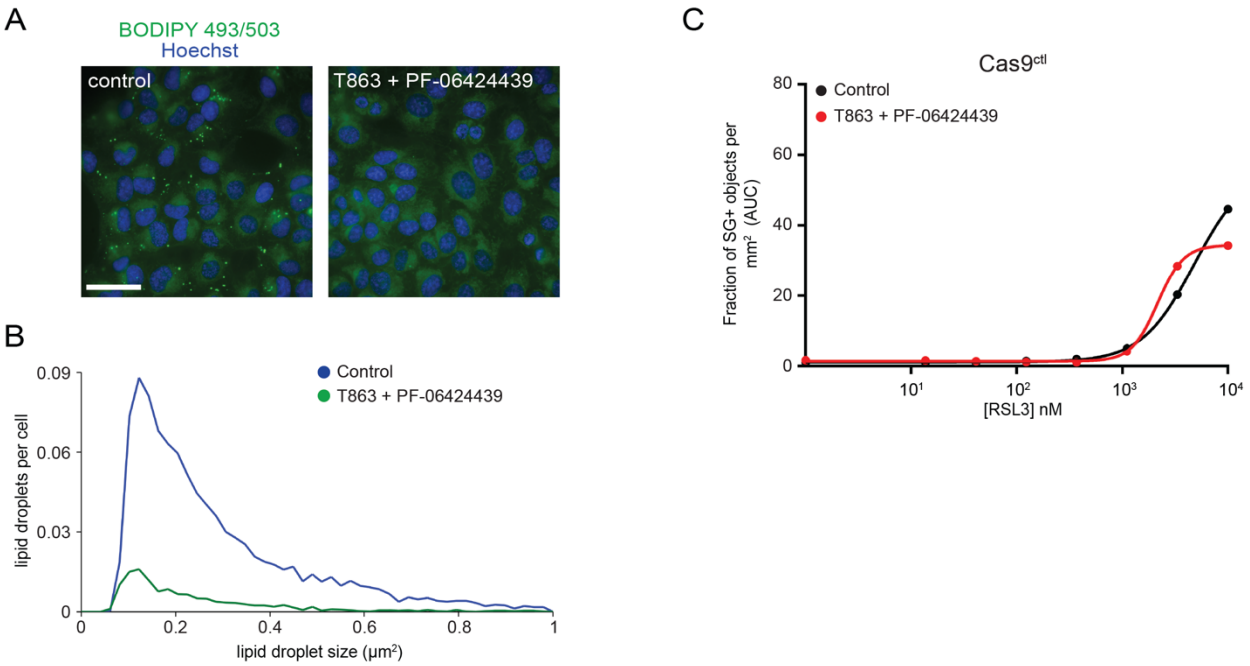

Figure 2-S5: Lipid droplets are not required for inhibition of ferroptosis by FSP1
(A) Control cells were treated with inhibitors of DGAT1 (20 μM T863) and DGAT2 (10 μM PF-06424439) for 48 hr, stained with 1 μM BODIPY 493/503 and imaged by fluorescence microscopy. The image is representative of n = 50 imaged fields. Scale bar = 10 μm. (B), The size and number of LDs were quantified from cells (n > 5000) in panel (a). (C), Dose response of RSL3-induced cell death of control cells pretreated for 48 hr with 20 μM T863 and 10 μM PF-06424439 prior to addition of RSL3. Each data point is the average of 3 technical replicates. All figures are representative of two biological replicates.

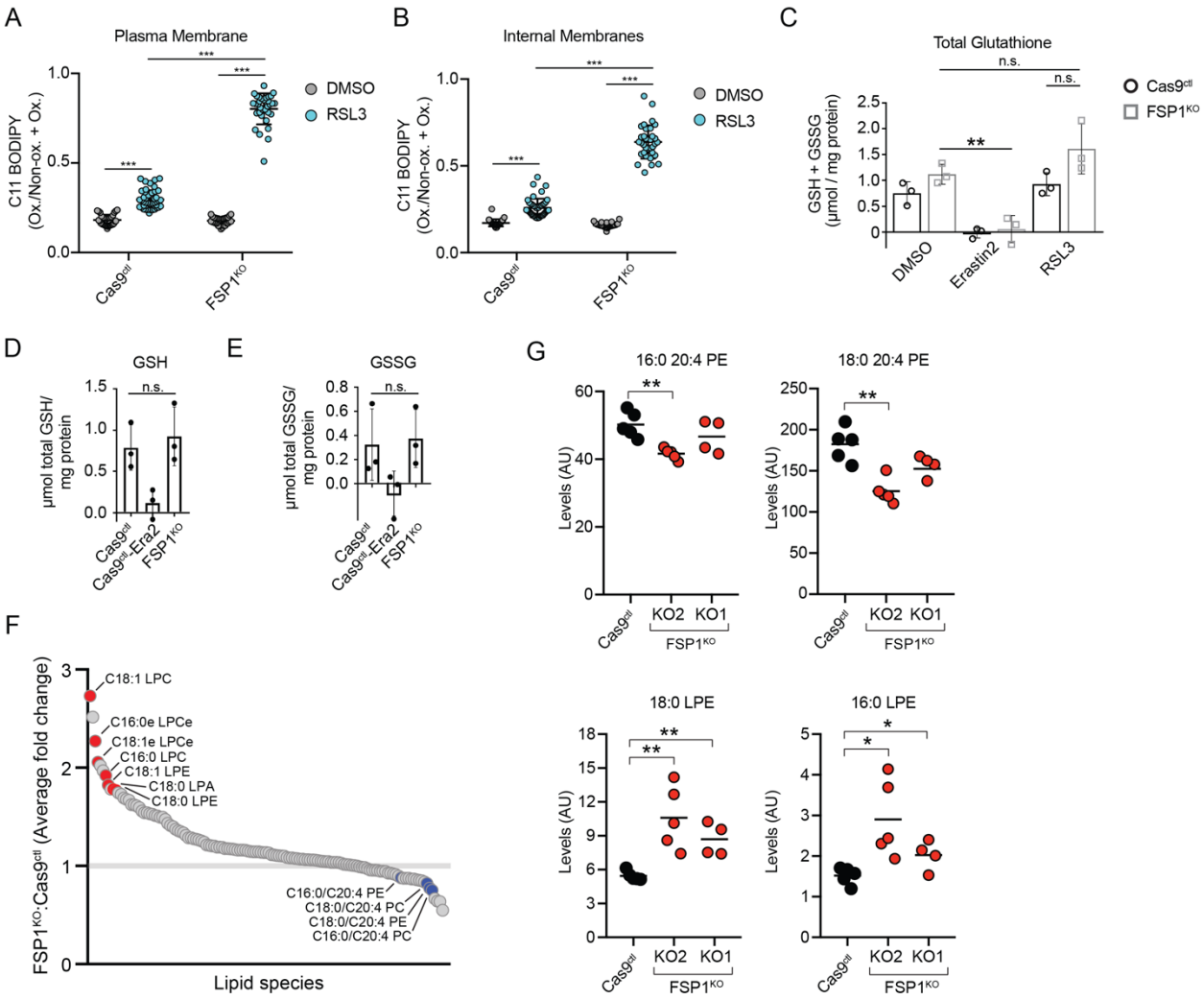

Figure 2-S6: Analysis of lipid peroxidation, glutathione and lipid levels in FSP1^{KO} cells (A,B) Ratio of oxidized to total BODIPY 581/591 C11 from images in figure 3A, at the plasma membrane (B) or at internal membranes (C). Each data point represents an individual cell quantified in one of two biological replicates. For (A), Cas9^{ctl}DMSO, n = 34; Cas9^{ctl} RSL3, n = 45; FSP1^{KO} DMSO, n = 30; FSP1^{KO} RSL3, n = 33; ***P < 0.001 by one-way ANOVA. For (B), Cas9^{ctl} DMSO, n = 33; Cas9^{ctl} RSL3, n = 45; FSP1^{KO} DMSO, n = 30; FSP1^{KO} RSL3, n = 33; ***P < 0.001 by one-way ANOVA. Error bars show mean ± SD. (C) Total intracellular glutathione (GSH + GSSG) levels in control and FSP1^{KO}were determined following treatment with 250 nM RSL3 or 1 µM Erastin2. The graph shows mean ± SD of n = 3 biological replicates. n.s., FSP1^{KO} DMSO versus RSL3, P = 0.7278; n.s., FSP1^{KO} RSL3 versus Cas9^{ctl} RSL3, P = 0.1522, **P = 0.0072 by one-way ANOVA. (D,E), GSH and GSSG levels in control and FSP1^{KO} were measured. Where indicated, cells were treated with 1 µM Erastin2. The graph shows mean ± SD of n = 3 biological replicates. n.s., GSH P = 0.6269; n.s., GSSG P = 0.8284 by two-tailed t-test. (F) The plot shows the average of the fold change in lipids measured in two FSP1^{KO} cell lines, generated using sgRNA 1 and sgRNA 2, relative to control cells. Cas9^{ctl}, n = 5; KO1, n = 4; KO2, n = 5 biological replicates (Supplemental Table

3)[89]. (G) Levels of select lipid species in biological replicates of control and FSP1^{KO} cells measured in (F). The average values are indicated. 16:0 20:4 PE, **P = 0.0017; 18:0 20:4 PE, **P = 0.0011; 18:0 LPE, KO2 **P = 0.0036, KO1 **P = 0.0019; 16:0 LPE, KO2 *P = 0.0133, KO1 *P = 0.0335 by two-tailed t-test.

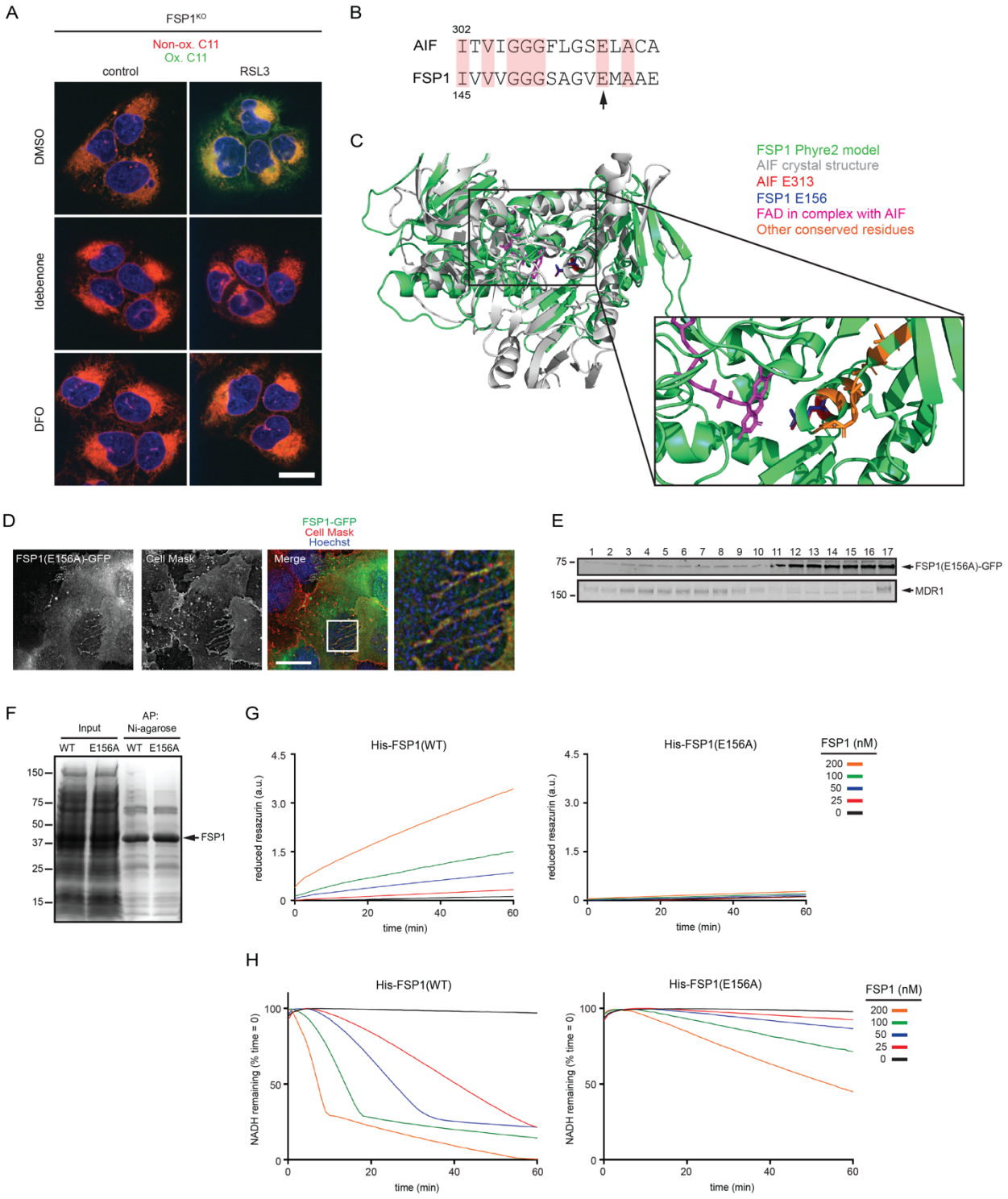

Figure 2-S7: Analysis of the FSP1 oxidoreductase mutant
(A) FSP1^{KO} cells were treated with 250 nM RSL3 and 10 μM idebenone or 50 μM DFO for 75 min, labeled with BODIPY 581/591 C11 and fixed prior to imaging. Ox. = oxidized; Non-ox. = non-oxidized. Images are representative of at least n = 10 cells imaged for each treatment condition. Scale bar = 20 μm. (B) Sequence alignment showing residues

conserved between AIF and FSP1. The arrow points to E313 in AIF (aligns to E156 in FSP1) that functions in FAD binding. (C) Structural alignment between the crystal structure of mouse AIF (PDB 1GV4) and the Phyre2-generated model of FSP1. (D) Live cell microscopy of $FSP1^{KO}$ cells expressing inducible FSP1(E156A)-GFP labeled with 5 µg/mL Cell Mask. The image is representative of at least n = 10 imaged cells. Scale bar = 10 µm. (E) Plasma membrane subdomains from $FSP1^{KO}$ cells expressing FSP1(E156A)-GFP were enriched by OptiPrep gradient centrifugation. (F) SDS-PAGE and Coomassie brilliant blue stain of recombinant His-FSP1(WT) and His-FSP1(E156A) purified with Ni-NTA agarose beads. (G) Reduction of resazurin by recombinant FSP1 in the presence of NADH. (H) Oxidation of NADH by recombinant FSP1 in the presence of coenzyme Q1. Figures (G,H) are representative of two biological replicates, and figure e shows a single experiment.

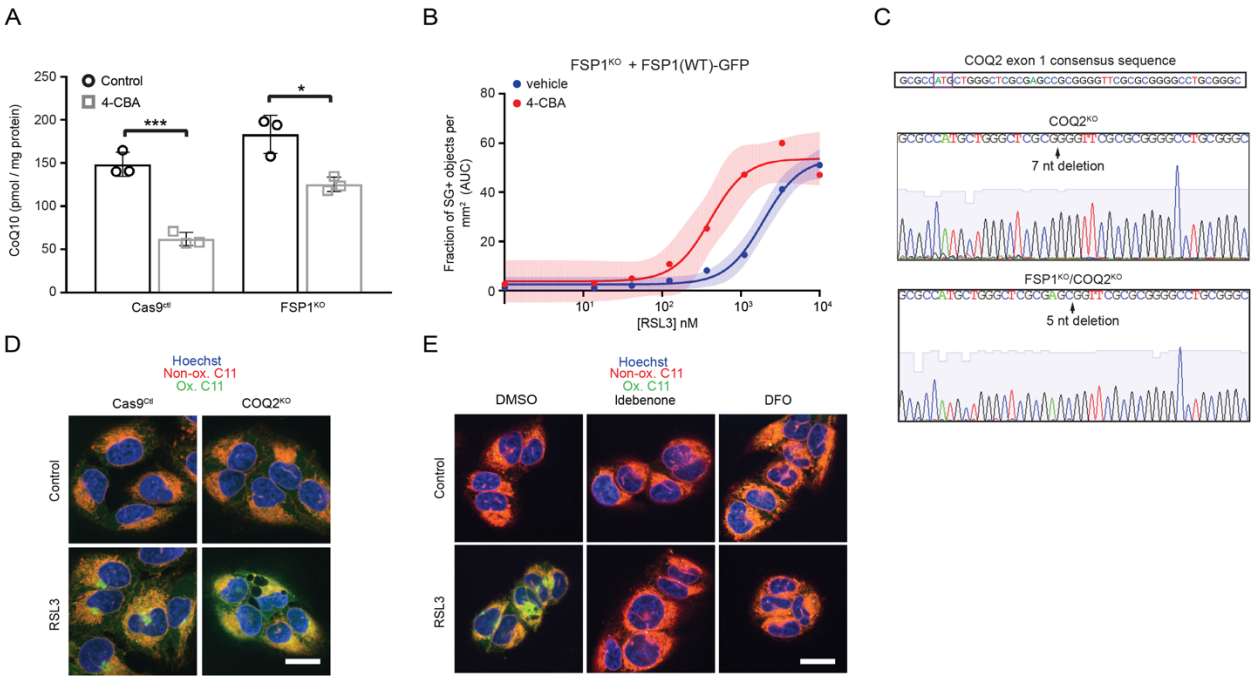

Figure 2-S8: Lipid peroxidation in CoQ-depleted cells
(A)Total CoQ levels in control and FSP1^{KO} cells treated for 48 hr with 3 mM 4-CBA. The graph shows mean ± SD of n = 3 biological replicates. ***P = 0.0007; *P = 0.0132 by two-tailed t-test. (B) Dose response of RSL3-induced death of inducible FSP1-GFP cells pretreated for 48 hr with 3 mM 4-CBA and doxycycline prior to addition of RSL3. Shading indicates 95% confidence intervals for the fitted curves and each data point is the average of 3 technical replicates. The figure is representative of two biological replicates. (C) Genomic sequencing of the COQ2 gene in COQ2^{KO} and FSP1^{KO}/COQ2^{KO}cells. The ATG start codon is boxed in the COQ2 consensus sequence. (D) Control and COQ2^{KO} cells treated with 250 nM RSL3 for 3 hr were labeled with BODIPY 581/591 C11 and fixed prior to imaging. Ox. = oxidized; Non-ox. = non-oxidized. (E) COQ2^{KO} cells were treated with 250 nM RSL3 and 10 μM idebenone or 50 μM DFO for 3 hr, labeled with BODIPY 581/591 C11 and fixed prior to imaging. Ox. = oxidized; Non-ox. = non-oxidized. For figures (D,E), images are representative of at least n = 10 cells imaged for each treatment condition. Image scale bars = 20 μm.

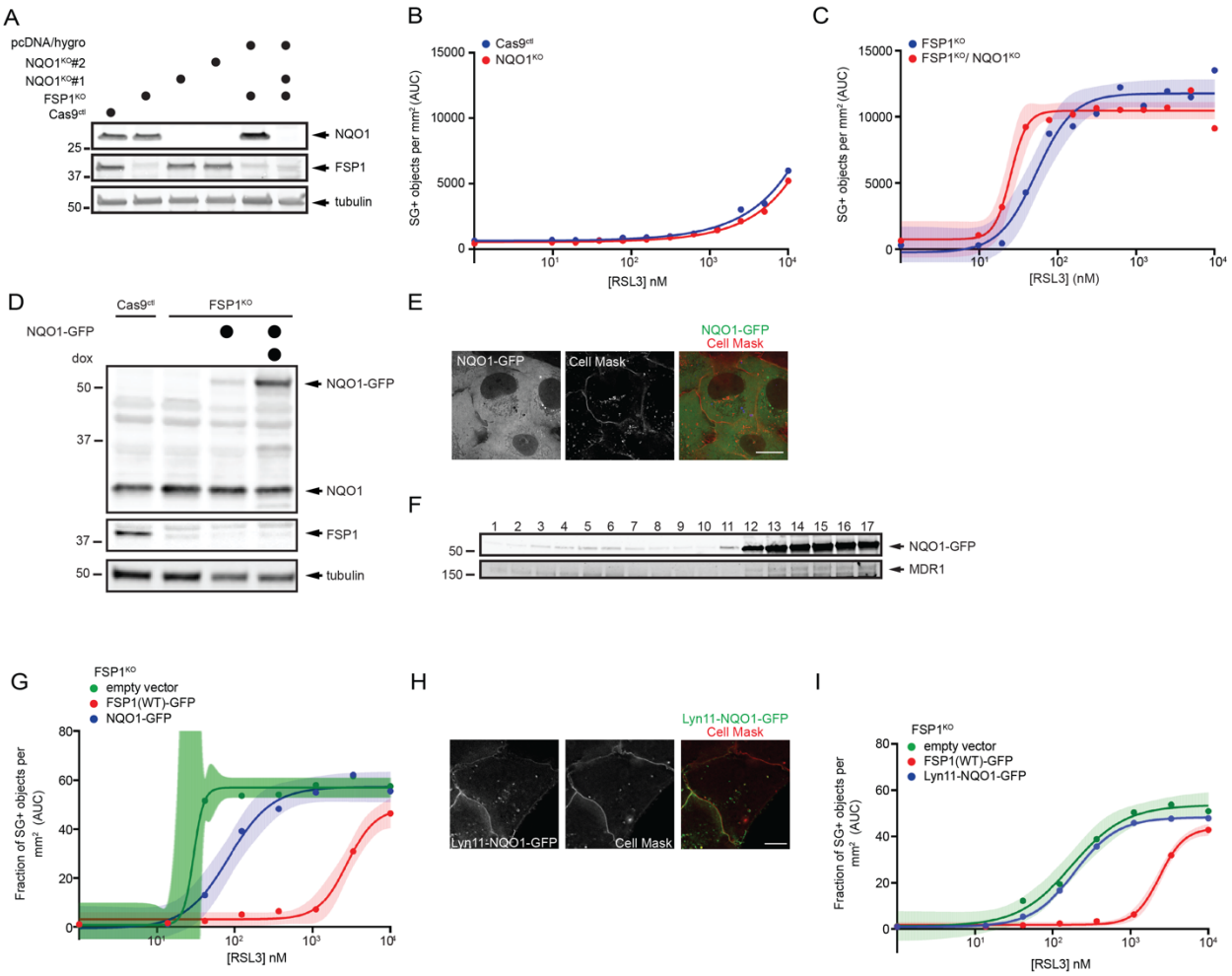

Figure 2-S9: Role of NQO1 in ferroptosis resistance

(A) Western blot analysis of lysates from NQO1^{KO} and NQO1^{KO}/FSP1^{KO} cells. (B) Dose response of RSL3-induced death of control and NQO1^{KO} cells. (C) Dose response of RSL3-induced death of FSP1^{KO} and NQO1^{KO}/FSP1^{KO} cells. Cells in (B,C) were generated using NQO1 sgRNA 1. (D) Western blot analysis of lysates of FSP1^{KO} cells expressing doxycycline-inducible NQO1-GFP. (E) Live cell microscopy of inducible NQO1-GFP cells labeled with 5 μg/mL Cell Mask. (F) Plasma membrane subdomains from FSP1^{KO} cells expressing NQO1-GFP were enriched by OptiPrep gradient centrifugation. (G) Dose response of RSL3-induced death of FSP1^{KO} cells expressing the indicated inducible constructs. (H) Live cell microscopy of FSP1^{KO}cells expressing inducible Lyn11-NQO1-GFP cells labeled with 5 μg/mL Cell Mask. (I) Dose response of RSL3-induced death of FSP1^{KO} expressing the indicated inducible constructs. For figures (B,C,G,I), shading indicates 95% confidence intervals for the fitted curves and each data point is the average of 3 technical replicates. Figures are representative of two biological replicates except figures (F,L), which show the results of single experiments. For figures (E,H), the images are representative of at least n = 10 imaged cells. Image scale bars = 10 μm.

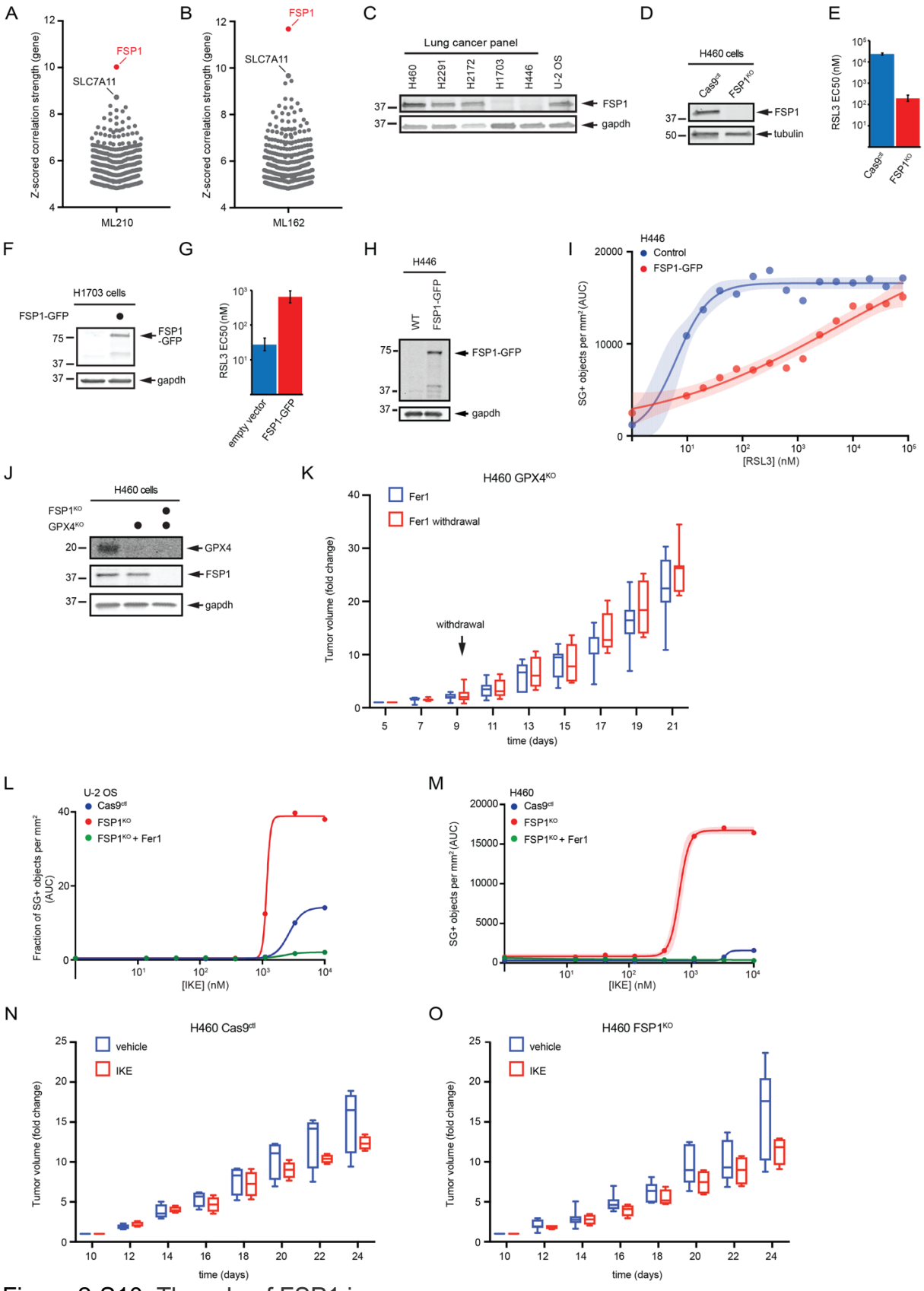

Figure 2-S10: The role of FSP1 in cancer

(A,B) High expression of FSP1 is correlated with resistance to the GPX4 inhibitors ML210 (A) and ML162 (B) in non-hematopoietic cancer cells. Plotted data was mined from the CTRP database that contains correlation coefficients between gene expression and drug sensitivity for 907 cancer cell lines treated with 545 compounds. Plotted values are z-scored Pearson's correlation coefficients. (C) Western blot of FSP1 expression in a panel of lung cancer lines. (D) Western blot of lysates from control and $FSP1^{KO}$ H460 cells. (E) EC50 RSL3 dose for the indicated H460 cell lines was calculated from the results in Figure 1D. Bars indicate 95% confidence intervals. (F) Western blot of lysates from control and H1703 cells. (G) EC50 RSL3 dose for the indicated H1703 cell lines was calculated from the results in Figure 1E. Bars indicate 95% confidence intervals. (H) Western blot analysis of H446 cells expressing doxycycline-inducible FSP1-GFP. (I) Dose response of RSL3-induced death of control and FSP1-GFP H446 cells. (J) Western blot of lysates from $GPX4^{KO}$ and $GPX4^{KO}$/$FSP1^{KO}$ H460 cells. (K) $GPX4^{KO}$ H460 tumor xenografts cells were initiated in immune-deficient SCID mice (n = 16). Following 5 days of daily Fer1 injections (2 mg/kg) to allow lines to develop tumors, one set of mice (n = 8) continued to receive daily Fer1 injections and a second set (n = 8) received vehicle injections for the remaining 17 days. The distribution of fold changes in sizes of individual tumors during the treatment is shown. $GPX4^{KO}$ (−) Fer1, n = 7; $GPX4^{KO}$ (+) Fer1, n = 7. (L) Dose response of IKE-induced death of control and $FSP1^{KO}$ U-2 OS cells. (M) Dose response of IKE-induced death of control and $FSP1^{KO}$ H460 cells. (N,O) Control (N) and $FSP1^{KO}$ (O) H460 tumor xenografts were initiated in immune-deficient SCID mice (n = 16). After 10 days, each group of mice (n = 8) was injected daily with 40 mg/kg IKE or vehicle. The distribution of fold changes in sizes of individual tumors during the treatment is shown. $Cas9^{KO}$ (−) IKE, n = 4; $Cas9^{KO}$ (+) IKE, n = 4; $FSP1^{KO}$(−) IKE, n = 7; $FSP1^{KO}$ (+) IKE, n = 4. For figures (K,N,O) box plots show median, 25^{th} and 75^{th} percentiles, minima and maxima of the distributions. Figures are representative of two biological replicates expect figures (L,M), which show the results of single experiments. For figures (I,L,M) shading indicates 95% confidence intervals for the fitted curves and each data point is the average of 3 technical replicates.

Chapter 3:
Identification of structurally diverse FSP1 inhibitors that sensitize cancer cells to ferroptosis

Contents in this chapter are modified from the previously published manuscript:

Hendricks JM, Doubravsky CE, Wehri E, *et al.* Identification of structurally diverse FSP1 inhibitors that sensitize cancer cells to ferroptosis. Cell Chem Biol. 2023 Sep 21;30(9):1090-1103.e7. doi: 10.1016/j.chembiol.2023.04.007.

3.1 Introduction

In this chapter, I describe the foundational experiments that led to the discovery of novel FSP1 inhibitors that sensitize cancer cells to ferroptosis. Below I provide a summary of ferroptosis and the role of FSP1 as a resistance factor.

Ferroptosis is an iron-dependent, non-apoptotic form of regulated cell death that is associated with the lethal accumulation of oxidatively damaged phospholipids (e.g., lipid hydroperoxides)[1,151]. As the ultimate effectors, phospholipid hydroperoxides, or their breakdown products, mediate membrane rupture and ferroptotic cell death[1,151]. Cellular ferroptosis sensitivity is determined by a variety of metabolic processes, including pathways that regulate labile iron pools and the generation of ROS, the addition and removal of oxidation-sensitive PUFAs to and from phospholipids, and ferroptosis defense systems that suppress the accumulation of lipid hydroperoxides[1,151]. These ferroptosis defense systems function through two mechanisms, the conversion of lipid hydroperoxides into non-toxic lipid alcohols by GPX4[3] and the generation of endogenous antioxidants that prevent lipid radical propagation, such as the enzymatic regeneration of the reduced form of coenzyme Q10 (CoQ) (i.e., ubiquinol) by FSP1[89,90] and dihydroorotate dehydrogenase (DHODH)[197], tetrabiohydropterin by GCH1[121,122], and hydropersulfides by enzymatic and non-enzymatic pathways[198,199].

Ferroptosis serves as a natural mechanism to restrict cancer proliferation and survival that is engaged by tumor suppressors. For example, the expression of the system xc^- antiporter subunit SLC7A11, required for cystine uptake and GSH synthesis, is inhibited by the tumor suppressors BAP1[97], p53[96], and Kelch-like ECH-associated protein 1 (KEAP1)[200]. Inactivating mutations in these tumor suppressors upregulate SLC7A11 and other genes that promote ferroptosis resistance[144]. While oncogene-driven reprogramming of cancer cell metabolism addresses the amplified cellular demands for nutrients and energy, the accompanying increases in ROS, and a consequent overreliance upon ferroptosis defensive systems for survival, yield potential therapeutic vulnerabilities[144,201,202]. Indeed, inhibition of the GSH-GPX4 pathway is effective in killing many cancer cells in vitro and in reducing tumor growth in preclinical models of therapy resistant cancers such as pancreatic ductal adenocarcinoma (PDAC)[167,168], clear cell and chromophobe renal carcinomas[6,203], triple-negative breast cancer[204], MYCN-amplified neuroblastoma[205–208], and drug-resistant persister cancer cells that give rise to relapse[98,173]. Despite these promising findings, some cancer cells are resistant to inhibition of the GSH-GPX4 pathway due to compensation by parallel ferroptosis defense systems. However, in contrast to the GSH-GPX4 pathway[209], few molecular tools are available that target the other ferroptosis defense systems such as the CoQ-FSP1 pathway.

FSP1 is an important ferroptosis resistance factor in cancer that compensates for the loss of GPX4 by mediating NAD(P)H-dependent reduction of ubiquinone (oxidized form of CoQ) to ubiquinol (reduced form of CoQ), which in turn acts as a lipophilic antioxidant to prevent lipid peroxidation propagation[89,90]. FSP1 exhibits high expression in ferroptosis resistant non-small cell lung cancer and its expression correlates with poor patient

prognosis[144]. Genetic disruption of FSP1 sensitizes cancer cells to ferroptosis and impairs tumor growth in a model of KEAP1-deficient lung cancer[89,144]. The tumor suppressor KEAP1 is an adaptor for the cullin-3 E3 ubiquitin-protein ligase that mediates the proteasomal degradation of nuclear factor erythroid 2-related factor 2 (NRF2), a master transcription factor that regulates the expression of an antioxidant gene program[210,211]. Thus, inhibitors of FSP1 have potential therapeutic value as anti-cancer monotherapies or when used in combination with ferroptosis inducers such as compounds targeting the GSH-GPX4 pathway. Consistent with this possibility, an inhibitor of FSP1 (iFSP1) sensitized multiple cancer cell lines to ferroptosis triggered by GPX4 inhibition and radiotherapy[90,144]. iFSP1 provides an important proof of concept, but additional structurally distinct FSP1 inhibitors with improved pharmacokinetic and pharmacodynamic properties are critically needed to fully explore the potential of FSP1 as a therapeutic target.

To address the unmet need for FSP1 inhibitors, we conducted a series of small molecule screens that leverage an in vitro assay of FSP1 CoQ oxidoreductase activity and an orthogonal cell-based assay of FSP1-dependent ferroptosis suppression. These screens identified multiple structurally distinct small molecules that directly inhibit FSP1 CoQ oxidoreductase activity in vitro and sensitize cancer cells to ferroptosis. Moreover, a second screen of U.S. Food and Drug Administration (FDA)-approved and bioactive compounds identified a synergistic relationship of FSP1 inhibition with the endoperoxide-containing drug dihydroartemisinin (DHA) in inducing ferroptosis. Our study provides new molecular tools for the characterization of FSP1 as an anti-cancer therapeutic target and demonstrates the utility of combinatorial treatment regimens targeting FSP1 together with other ferroptosis defense pathways.

3.2 Results

3.2.1 Chemical library screen identifies small molecule inhibitors of FSP1 activity

To identify small molecule inhibitors of FSP1, we conducted a chemical screen employing an in vitro assay of FSP1 activity (Figure 3-1A,B). This assay exploits the change in 355 nm absorbance as NADH is oxidized to NAD+ during the reduction of CoQ1 by recombinant FSP1 (Figure 3-1B,C). As anticipated, the addition of FSP1 to the reaction mix resulted in a decrease in absorbance over time (Figure 3-1C). Moreover, the decrease in absorbance was blocked in a dose-dependent manner by iFSP1 (IC_{50} of 4 μM) (Figure 3-1C, Figure 3-S1A). These data demonstrate that iFSP1 is a direct FSP1 inhibitor and validates our activity assay as a method to identify FSP1 inhibitors.

In the primary screen, the effect of 120,370 small molecules on FSP1 activity was analyzed using the in vitro FSP1 activity assay (Figure 3-1A,D). This screen identified 1,120 candidate FSP1 inhibitors based on a 0.264 normalized absorbance threshold value (Figure 3-1D). Duplicate analyses of the candidate inhibitors were performed for validation (Figure 3-S1B). A control lacking FSP1 protein was included to identify small molecules that altered absorbance independently of FSP1 (Figure 3-S1C). This series of validation steps yielded 323 inhibitors. Finally, triplicate 10-point dose response analyses

were performed to determine the in vitro potency of 168 selected FSP1 inhibitors. 26 of these compounds have a lower IC_{50} than iFSP1 (< 4 μM) and 11 compounds have an IC_{50} below 100 nM.

3.2.2 Small molecule inhibitors of FSP1 trigger cell death in a cancer cell model

To determine whether the 168 candidate FSP1 inhibitors are able to inhibit FSP1 in cells, we developed an orthogonal cell-based assay of FSP1 activity. This assay uses NCI-H460 KEAP1 mutant lung cancer cells expressing mCherry ($H460^{C}$) in which GPX4 was knocked out using CRISPR-Cas9 ($H460^{C}$ $GPX4^{KO}$) or which expressed Cas9 as a control ($H460^{C}$ Cas9) (Figure 3-1E). mCherry was used as a live cell marker, which together with the SYTOX Green cell death marker can be used to calculate the fraction of dead cells (i.e., lethal fraction[75,212]). To validate this assay, $H460^{C}$ Cas9 cells and $H460^{C}$ $GPX4^{KO}$ cells were treated with iFSP1 (Figure 3-1F,G). iFSP1 selectively triggered cell death in $H460^{C}$ $GPX4^{KO}$ cells, but not in the $H460^{C}$ Cas9 cells (Figure 3-1F,G). These data demonstrate that this assay can be used to characterize the ability of FSP1 inhibitors to inhibit FSP1 and induce ferroptosis in cancer cells.

Employing this assay, we analyzed the amount of cell death induced by 168 compounds that inhibited FSP1 oxidoreductase activity in vitro (Figure 3-1A,D) in the $H460^{C}$ Cas9 and $H460^{C}$ $GPX4^{KO}$ cells (Figure 3-1H). $H460^{C}$ Cas9 cells were included to identify any small molecules that kill cells through a ferroptosis-independent mechanism. Triplicate 10-point dose response analyses were performed, and cell death was measured using fluorescence time-lapse imaging (Figure 3-1H). ~50 of the FSP1 inhibitors induced cell death in the $H460^{C}$ $GPX4^{KO}$ cells (Figure 3-1H), but not the $H460^{C}$ Cas9 cells, indicating that these compounds are synthetic lethal with $GPX4^{KO}$ and are not generally toxic to cells.

19 of the most potent compounds were tested again using validated compounds (>95% purity) in 20-point dose response analyses in both the in vitro (Figure 3-S2 and 3-S3) and cell-based FSP1 assays (Figure 3-1I). As observed in our primary and follow up screens, these 19 compounds directly inhibited purified FSP1 in vitro (Figure 3-S2 and 3-S3) and triggered cell death in the $H460^{C}$ $GPX4^{KO}$ cells, but not the $H460^{C}$ Cas9 cells (Figure 3-1I). We named these validated FSP1 inhibitors – ferroptosis sensitizer 1-19 (FSEN1-19). The structures of FSEN1-19, their IC_{50} for inhibition of purified FSP1 activity, and their EC_{50} for triggering cell death in $H460^{C}$ $GPX4^{KO}$ cells are shown in Figure 3-2. These compounds can be organized into seven groups of structurally related compounds. The largest group of compounds (Group 1, red box) share a disubstituted [1,2,4] triazolo-thiazole core scaffold structure (Figure 3-2).

3.2.3 FSEN1 is an uncompetitive inhibitor of FSP1

Amongst the newly identified FSP1 inhibitors, FSEN1 exhibited the highest potency in triggering cell death in the $H460^{C}$ $GPX4^{KO}$ cells (EC_{50} = 69.363 nM) (Figure 3-2). To test the specificity of FSEN1, we examined its ability to inhibit NQO1, another CoQ oxidoreductase that has been implicated in ferroptosis[75]. In contrast to FSP1 (Figure 3-

3A), FSEN1 had no effect on the CoQ oxidoreductase activity of NQO1 (Figure 3-3B), indicating that FSEN1 does not generally inhibit CoQ oxidoreductases and that FSEN1 exhibits selectivity towards FSP1.
To understand the mechanism of FSP1 inhibition by FSEN1, enzyme kinetics were analyzed using the in vitro FSP1 activity assay in the presence of increasing amounts of its substrates, NADH (Figure 3-3C,D) and a fluorescent ubiquinone analogue CoQ-coumarin (Figure 3-3E,F). As FSEN1 concentrations increased, we observed a decrease in Kcat values (Figure 3-3C,E), and the slopes of the Lineweaver-Burke plots were parallel (Figure 3-3D,F). We observed a similar effect of FSEN1 on the Vmax of FSP1 using CoQ1 as a substrate (Figure 3-S4), but this assay was unable to resolve the Km due to limitations in its sensitivity. These findings reveal that FSEN1 is an uncompetitive inhibitor of FSP1. Thus, these data suggest that FSP1 requires binding to its substrates NADH and CoQ first in order to be permissive for FSEN1 binding, which then yields the inactive complex.

3.2.4 FSEN1 triggers ferroptosis in cancer cells by inhibiting FSP1

To characterize the cell death induced by FSEN1 treatment, we further examined its effects on $H460^{C}$ Cas9 lung cancer cells. Treatment with FSEN1 sensitized $H460^{C}$ Cas9 cells to cell death induced by two GPX4 inhibitors, RSL3 and ML162 (Figure 3-4A-C). A checkerboard dose-response matrix of FSEN1 (0-15 μM) and RSL3 (0-15 μM) provided further evidence of synthetic lethality and indicated that the minimal doses that achieve maximal synergy for inducing ferroptosis in $H460^{C}$ Cas9 cells are 0.55 μM FSEN1 together with 0.55 μM RSL3 (Figure 3-4B). Dying cells exhibited characteristic morphologies of ferroptotic cells and the cell death was blocked by ferrostatin-1 (Fer-1) (Figure 3-4C). Consistent with FSEN1 sensitizing these cells to ferroptosis, cell death induced by the co-treatment of FSEN1 and RSL3 was blocked by incubation with known ferroptosis inhibitors, including the radical-trapping antioxidants idebenone, Fer-1, and tocopherol, and the iron chelator deferoxamine (DFO) (Figure 3-4D, Figure 3-S5E). In contrast, the apoptosis inhibitor Z-VAD-FMK and necroptosis inhibitor Nec1s had no effect (Figure 3-4D, Figure 3-S5E). Furthermore, treatment with FSEN1 sensitized cells to lipid peroxidation, as measured using the fluorescent lipid peroxidation reporter dye BODIPY C11 (Figure 3-4E). These findings demonstrate that FSEN1 sensitizes H460 lung cancer cells to lipid peroxidation and ferroptosis induced by GPX4 inhibition.

To determine if FSEN1 sensitizes cells to ferroptosis by inhibiting FSP1, we tested the effect of FSEN1 on RSL3-induced ferroptosis in a $H460^{C}$ cell line in which we knocked out FSP1 using CRISPR-Cas9 ($H460^{C}$ $FSP1^{KO}$ cells). $H460^{C}$ $FSP1^{KO}$ cells were greatly sensitized to RSL3-induced cell death (Figure 3-4F). Importantly, although FSEN1 sensitized $H460^{C}$ Cas9 cells to RSL3-induced cell death, treatment of the $H460^{C}$ $FSP1^{KO}$ cells with FSEN1 did not result in any additional sensitization to RSL3-induced cell death (Figure 3-4F). These data indicate that the effects of FSEN1 are due to on target inhibition of FSP1 and not through inhibition of other ferroptosis resistance factors, including other CoQ oxidoreductases implicated in ferroptosis such as NQO1[75].

High cell densities and cell-cell interactions promote ferroptosis resistance by inducing multiple signaling pathways, including the NF2–YAP[176] and TAZ-EMP1-NOX4[213] pathways, underscoring the importance of testing ferroptosis sensitivity in 3-dimensional (3-D) tumor models. Spheroids are 3-D aggregates of cancer cells that more closely reflect key characteristics of solid tumor biology, including cell-cell interactions, hypoxia, drug penetration, and interactions with deposited extracellular matrix[214]. Importantly, similar to our 2-D culture experiments, RSL3 and FSEN1 synergized to trigger cell death in H460 cells grown in the 3-D spheroids (Figure 3-4G). Together, these findings indicate that FSEN1 sensitizes H460 lung cancer cells to ferroptosis in both 2-D and 3-D culture models.

3.2.5 FSEN1 sensitizes multiple cancer cell lines of different tissue origins to ferroptosis

To examine the role of FSP1 in suppressing ferroptosis in different types of cancer, we measured the impact of FSEN1 on RSL3-induced cell death in a panel of cancer cell lines of various tissue origins, including lung ($A549^N$), breast ($HCC1143^C$), liver ($Huh7^C$), glial ($T98G^N$), bone ($U\ 2\text{-}OS^N$), connective ($HT\text{-}1080^N$), lymphoid (RL, SUDHL5), and skin (A375, SKMEL28, 501-MEL) (Figure 3-5A,B and Figure 3-S5A,B). FSEN1 sensitized all cancer cells to RSL3-induced ferroptosis to varying extents, and in all cases the cell death was rescued by co-treatment with Fer-1. These findings indicate that FSEN1 can sensitize multiple cancer cell lines of different origins to ferroptosis induced by GPX4 inhibition. Notably, FSEN1 had a particularly large sensitizing effect on ferroptosis induction in A549 lung cancer cells (Figure 3-5A). A549, and the H460 cells used in our initial screens, are both lung cancer cell lines with KEAP1 mutations, which results in NRF2-dependent upregulation of FSP1[144]. The prominent role of FSP1 in protecting A549 and H460 cells from ferroptosis correlated with high FSP1 protein levels and low GPX4 levels relative to other cancer cell lines (Figure 3-S5C,D). It was also notable that FSEN1 induced a small amount of ferroptosis in A375 melanoma cells in the absence of an RSL3 co-treatment (Figure 3-5B), indicating that A375 cells have a particularly strong dependence on FSP1 for ferroptosis suppression. The amount of sensitization imbued by FSEN1 likely depends on the expression levels of FSP1 and ferroptosis related factors, such as GPX4, DHODH, GCH1, ACSL3, ACSL4, and others.

3.2.6 Analysis of FSEN1 metabolic stability, in vivo pharmacokinetics, and inhibition of mouse FSP1

To test the in vitro metabolism and in vivo disposition of FSEN1, we measured FSEN1 metabolic stability and pharmacokinetics in mice, respectively. Following a single 20 mg/kg intraperitoneal (I.P.) dose of FSEN1 to mice (n=5), the median (interquartile range; IQR) maximum plasma concentration was 97.6 ng/mL (71.0-123.0), while the median (IQR) elimination half-life was 8.0 hours (6.1 – 8.8) (Figure 3-S6A). FSEN1 also exhibited low intrinsic clearance (CL_{int}) in mouse liver microsomes (11.54 µL/min/mg protein), further indicating adequate metabolic stability (Figure 3-S6B). Collectively these data indicate that FSEN1 may be suitable for in vivo experiments in mice, such as studies examining the impact of FSEN1 on the growth of tumor xenografts.

To examine the ability of FSEN1 to inhibit mouse FSP1 (mFSP1), we expressed mFSP1 in the H460^{C} FSP1^{KO} cells. As expected, mFSP1 overexpression suppressed RSL3 induced ferroptosis (Figure 3-S6C-E). Treatment with 1 μM FSEN1 had no effect on the ferroptosis sensitivity of the FSP1^{KO} cells nor the FSP1^{KO} cells overexpressing mFSP1 (Figure 3-S6D). In addition, increasing the amount of FSEN1 up to 15 μM also had no effect on the sensitivity of FSP1^{KO} cells overexpressing mFSP1 to RSL3 (Figure 3-S6F). Furthermore, FSEN1 had no effect on the CoQ1 oxidoreductase activity of purified mFSP1 in vitro (Figure 3-S6G). Together, these data indicate that despite the high amount of amino acid similarity between human and mouse FSP1, FSEN1 is selective to human FSP1 and does not inhibit the oxidoreductase activity of mFSP1. Future studies examining the two proteins may facilitate the identification of mutations that influence FSEN1 inhibition of human FSP1.

3.2.7 FSP1 and dihydroartemisinin treatment synergize to trigger ferroptosis in cancer cells

As ferroptosis suppression is mediated by several different pathways, it is perhaps not surprising that FSP1 inhibition alone is not sufficient to induce ferroptosis in most cancer cell lines. Furthermore, while FSEN1 is synthetically lethal with GPX4 inhibitors such as RSL3 (Figure 3-4A), the in vivo efficacy of RSL3 is known to be limited due to low solubility and poor pharmacokinetics[144]. Therefore, we conducted a synthetic lethal screen to identify compounds that eliminate cancer cells specifically in the absence of FSP1. H460^{C} Cas9 and H460^{C} FSP1^{KO} cells were treated for 24 h with a library of 5,370 compounds that includes 1,200 FDA approved drugs and 4,170 bioactive compounds, and lethal fraction was quantified by time-lapse fluorescence imaging (Figure 3-6A,B). RSL3 was included as a positive control. As expected, RSL3 was cytotoxic for the H460^{C} FSP1^{KO} cells but not the H460^{C} Cas9 cells (Figure 3-6B), validating the ability of our screening approach to detect synthetic lethal relationships.

Several compounds selectively induced cell death in the FSP1^{KO} cells, including DHA (Figure 3-6B-D). DHA is a sesquiterpene lactone compound (Figure 3-6E) that is the active metabolite of an FDA approved drug (artesunate), which has been widely used as an antimalarial, and that has also been explored as an anti-cancer therapeutic[215]. The endoperoxide bridge within DHA (Figure 3-6E) is known to react with ferrous iron and stimulate the formation of toxic free radicals[215]. In addition, DHA was recently shown to induce ferroptosis in multiple cancer types[216–218]. Similar to DHA, the ferroptosis inducer FINO2 contains an endoperoxide bridge (Figure 3-6E) that oxidizes iron, increases lipid peroxidation, and induces ferroptosis[219]. FSEN1 treatment and FSP1 KO strongly sensitized H460^{C} cells to cell death induced by both DHA and FINO2 (Figure 3-6F,G). FSEN1 had no additional sensitizing effect in the FSP1^{KO} cells (Figure 3-6F,G), indicating that the ability of FSEN1 to sensitize cells to DHA and FINO2 induced cell death is due to its on target inhibition of FSP1. DHA and FSEN1 treatment together induced cell death (DHA EC_{50} = 21.3 μM) that was strongly suppressed by ferroptosis inhibiting radical-trapping antioxidants (Fer-1, tocopherol, idebenone) and completely suppressed by DFO (Figure 3-6H,I).

To characterize the synergy between DHA, RSL3, and FSEN1, we performed a checkerboard dose-response matrix of DHA (0-80 μM) and RSL3 (0-15 μM) in the presence of increasing doses of FSEN1 (0, 0.05, 0.5, 5 μM), and quantified synergy potency using a computational zero interaction potency (ZIP) modeling system[220] (Figure 3-7A). The ZIP synergy scoring system defines compound synergy as a value >10, additive effects -10<0<10, and antagonistic effects <-10 (Figure 3-7A). The combinations of FSEN1 and RSL3 (Mean ZIP score = 38.28) and FSEN1 and DHA (Mean ZIP score = 26.45) exhibited strong synergy (Figure 3-7B,C and Figure 3-S7). In contrast, DHA and RSL3 showed little synergy (Mean ZIP score = 4.11) (Figure 3-7B,C and Figure 3-S7) and a stronger synergy score was observed with all three compounds (Mean ZIP score = 52.69) (Figure 3-7D). Together, these data indicate that FSP1 inhibition increases cancer cell sensitivity to endoperoxide-containing ferroptosis inducers, including DHA. Moreover, these findings demonstrate the potential value of combinatorial therapeutic strategies that combine FSP1 inhibitors with additional ferroptosis inducers to overcome the multitude of cancer ferroptosis defenses.

3.3 Discussion

Induction of ferroptosis has emerged as a promising strategy to treat therapy-resistant cancer[221]. Despite the discovery of multiple cellular ferroptosis defense systems[151,221], current ferroptosis inducers are mostly limited to the GSH-GPX4 pathway, impeding the study and assessment of other ferroptosis regulators as therapeutic targets. Here, we describe the discovery and characterization of structurally distinct small molecule FSP1 inhibitors that directly inhibit FSP1 activity and sensitize cancer cells to ferroptosis. The most potent of these new FSP1 inhibitors, FSEN1, is an uncompetitive FSP1 inhibitor that is synthetic lethal with GPX4 inhibitors and endoperoxide-containing ferroptosis inducers, including FINO2 and DHA, the active metabolite of the FDA approved drug artesunate.

Given that FSP1 expression correlates with resistance to GPX4 inhibitors across many cancer cell lines[89,90], it is likely that FSEN1 will be useful for sensitizing many cancer types to ferroptosis inducers that target the GSH-GPX4 axis. Indeed, FSEN1 sensitized several cancer cell lines of different tissue origins bearing different oncogenic mutations to RSL3. The variable amount of sensitization FSEN1 confers on distinct cancer cell lines indicates that some cancers are more reliant on FSP1 for ferroptosis suppression than others, likely reflecting the contribution of other ferroptosis defense pathways or differences in phospholipid composition and ROS production. Strong sensitization was observed in H460 and A549 cancer cells, which are both lung cancer cell lines with KEAP1 mutations. KEAP1 regulates a canonical pathway that mediates the ubiquitin-dependent proteasomal clearance of NRF2, a master transcriptional factor that governs expression of antioxidant factors, including FSP1[144]. We find that these cell lines have high FSP1 and low GPX4 protein levels, suggesting a means to stratify cancers that will respond more strongly than others to FSP1 inhibition based upon FSP1 and GPX4 levels. A similar increased effectiveness of DHODH inhibition on ferroptosis induction in cancer cells with low GPX4 was previously observed[197]. However, there are many factors that govern

cellular sensitivity to ferroptosis and that while analysis of FSP1 and GPX4 levels may be predictive in some cells, this may not be the case in all cancer cells and additional regulators will need to be considered.

FSP1 inhibition alone was not sufficient to trigger ferroptosis in most of the cell types under the culture conditions that we examined here, except for the A375 melanoma cells. It is worth noting that FSP1 KO slowed tumor growth in an in vivo xenograft model of KEAP1 deficient lung cancer[144], indicating that loss of FSP1 activity is sufficient to induce ferroptosis under some in vivo conditions. This may reflect the unique contribution of the in vivo tumor microenvironment and higher levels of PUFAs and ROS. Importantly, the observation that FSP1 KO impairs tumor growth in vivo raises the possibility that small molecule FSP1 inhibition may be effective as a monotherapy for specific cancers. The result also highlights the importance of future studies to explore FSP1 inhibition in in vivo cancer models. Although FSEN1 does not inhibit mFSP1, FSEN1 exhibits good pharmacokinetics and metabolic stability in mice and it may be useful for in vivo models that employ human cancer cells (i.e., tumor xenografts).

Our findings are consistent with the utility of FSP1 inhibition in combinatorial therapeutic regimes together with inhibitors of the GSH-GPX4 pathway. It is likely that FSP1 inhibition will sensitize cancer cells to standard of care treatments that trigger ROS generation and ferroptosis such as radiotherapy[170,171], photodynamic therapy[222,223], and immunotherapy[172]. Indeed, FSP1 KO and iFSP1 treatment sensitize cancer cells to radiotherapy[144]. Along these lines, we discover that FSP1 inhibition synergizes with DHA to induce ferroptosis. DHA is the active metabolite of a commonly used antimalarial (artesunate), it has been explored as an anticancer drug[215], and several recent studies indicate that DHA is capable of triggering ferroptosis[216–218]. The endoperoxide bridge within DHA reacts with and oxidizes iron, leading to the production of ROS and lipid hydroperoxides[215]. In H460 lung cancer cells, DHA induced minimal amounts of ferroptosis on its own, but its ability to induce ferroptosis was greatly enhanced by co-treatment with FSEN1. It remains possible that DHA operates through multiple mechanisms, oxidizing iron and triggering lipid peroxide formation and indirectly inhibiting GPX4 similar to what was reported for the endoperoxide ferroptosis inducer FINO2[219]. Our findings highlight the potential of endoperoxide containing compounds (e.g., FINO2[219], FINO3[224], DHA as therapeutic agents to induce ferroptosis by increasing iron oxidation, lipid peroxidation, and potentially GPX4 inhibition. Finally, it is worth noting that while the best known role of FSP1 is in the suppression of ferroptosis, FSP1 has also been implicated in the maintenance of glycolysis in muscle and brown adipocytes through its role in regenerating NAD+[225,226]. Thus, FSEN1 may also be lethal in cancer types that depend on glycolysis or may synergize with therapeutics that target glycolytic pathways.

In summary, our findings identify a set of structurally distinct FSP1 inhibitors that are effective in overcoming ferroptosis resistance in several cancer cell lines. Future studies will be necessary to determine whether these FSP1 inhibitors are effective in preclinical mouse models of cancer, as single agent therapeutics under certain conditions, and in sensitizing cancer cells to other treatments that increase ROS and lipid peroxidation, including ferroptosis induced by photodynamic therapy, radiation, and immunotherapy.

3.4 Materials and methods

3.4.1 Cell lines and culture conditions

A549^{N}, HCC1143^{C}, NCI-H460^{C}, NCI-H460^{C} GPX4^{KO} and FSP1^{KO} lines were cultured in RPMI1640 with l-glutamine (Corning, Cat# 10-040CV). HT-1080^{N}, U-2OS^{N}, T98G^{N}, Huh7^{C}, and A375 cells were cultured in DMEM with l-glutamine and without sodium pyruvate (Corning, Cat# 10-017-CM). 501-MEL and SKMEL28 cells were cultured in DMEM high glucose with l-glutamine and without sodium pyruvate (Corning, Cat# 10-017-CMR). Cells (HT-1080^{N}, U-2OS^{N}, T98G^{N}) were generated through stable expression of nuclear-localized mKate2 (denoted by an additional superscript 'N'). All media were supplemented with 10% fetal bovine serum (FBS, Thermo Fisher Scientific and Gemini Bio Products), and all cell lines were grown at 37 °C with 5% CO_2. All cell lines were tested for mycoplasma and were not authenticated.

3.4.2 Generation of cell lines

NCI-H460^{C} FSP1^{KO} lines were generated by infection with lentiCRISPR v2-Blast (Addgene plasmid no. 83489) virus, and NCI-H460^{C} GPX4^{KO} lines were generated by infection with lentiCRISPR v2-Hygro (Addgene plasmid no. 98291) virus, as previously described[89]. Cells expressing sgSAFE-mCherry (denoted by an additional superscript 'C') were generated from the respected parental cells via transduction with the lentiviral sgRNA expression vector with mCherry pMCB320 (Addgene plasmid no. 89359) virus, which directs the expression of cytosolic sgSAFE-mCherry. Polyclonal sgSAFE-mCherry expressing cells were selected for using puromycin or hygromycin respectively. H460^{C} polyclonal pools were selected puromycin and further enriched using FACS (UC Berkeley shared FACS Facility). H460^{C} FSP1^{KO} + mFSP1 OE lines were generated by infection with pLenti-CMV-Hygro-DEST (Addgene plasmid no. 17454) containing mFSP1.

3.4.3 Plasmids

For protein expression, FSP1(WT), lacking the ATG start codon were inserted into the pET-His6-TEV vector (Addgene plasmid no. 29653), as previously described[89]. For protein expression of NQO1, NQO1(WT) lacking the ATG start codon was generated by PCR amplification of NQO1 from an NQO1-GFP pcDNA5/FRT/TO plasmid generated in our previous study[89]. For protein expression of mFSP1, mFSP1(WT) lacking the ATG start codon was generated by PCR amplification of mFSP1 (NM_153779.2, OMu13438D) from mammalian expression cloning vector, pcDNA3.1^{+}/C-(K)-DYK (GenScript, Cat# SC1200). The NQO1(WT) and mFSP1(WT) amplicon was inserted into the pET-His6-TEV vector (Addgene plasmid no. 29653), C-terminal to the His6-TEV tag using restriction enzyme-independent fragment insertion by polymerase incomplete primer extension. Cloning of full length mFSP1(WT) expression plasmid was generated by PCR amplification of mFSP1 (NM_153779.2, OMu13438D) from mammalian expression cloning vector, pcDNA3.1^{+}/C-(K)-DYK (GenScript, Cat# SC1200). The mFSP1(WT) amplicon was inserted into the pENTR1A-GFP-N2 (Addgene plasmid no. 19364) vector

using restriction enzyme-independent fragment insertion by polymerase incomplete primer extension, followed by Gateway recombination cloning (Thermo Fisher Scientific, Cat# 12535-029) into pLenti-CMV-Hygro-DEST (Addgene plasmid no. 17454).

3.4.4 Chemicals and reagents

Reagents used in this study include: RSL3 (Cayman Chemical, Cat# 19288), Fer-1 (Cayman Chemical, Cat# 17729), Idebenone (Cayman Chemical, Cat# 15475), DFO (Cayman Chemical Cat# 14595), ML162 (Cayman Chemical, Cat# 20455), ZVAD(OMe)-FMK (Cayman Chemical, cat.# 14463), Necrostatin-1 (Cayman Chemical Cat# 11658), DHA (Selleck Chemical Cat# S2290), Puromycin (Thermo Fisher Scientific, Cat# A1113802), SYTOX Green Dead Cell Stain (Thermo Fisher Scientific, Cat# S34860), Polybrene (Sigma-Aldrich, Cat# TR-1003), Coenzyme Q_1 (Sigma-Aldrich, Cat# C7956), Resazurin (Thermo Fisher Scientific, Cat# R12204), Bodipy C11 (Thermo Fisher Scientific, Cat# D3861) and NADH (Millipore Sigma, Cat# 481913). A 100,000-member compound Diverse Library and a 15,000 compound Antibacterial Library were obtained from ChemDiv. The 1,200 compound FDA approved, and 4,170 compounds Bioactive libraries were obtained from TargetMol. Compounds were stamped into 384 well Non-Binding Surface (NBS) plates (Corning, Cat# CLS3640) using a Cybio Well Vario liquid handler (Analytik-Jena, Germany).

3.4.5 Small molecule screen for FSP1 inhibitors / Cell death analysis

For the small molecule drug screen, 0.5 µL of compounds were stamped into 384 well NBS plates (Corning, Cat# CLS3640) in dose response diluted 2-fold with a high of 2 mM. 60 mL of purified His tagged FSP1(WT) protein at 50 nM was prepared and 12.5 µL of this protein solution was aliquoted into 384 well NBS-plates (Corning, Cat# CLS3640) containing compound and allowed to incubate for 30 min at room temperature. After 30 min incubation 12.5 µL of reaction buffer (1 mM NADH, 800 µM CoQ1) was added into the 384 well NBS-plates containing protein and compounds for a final concentration of 25 nM His tagged FSP1(WT) protein, 500 µM NADH (Millipore Sigma, Cat# 481913) and 400 µM CoQ1 (Sigma-Aldrich, Cat# C7956). Each well contained a 25 µL mixture and 40 µM compound in the primary screen. All aliquots for in vitro drug screen were completed with an Analytik-Jena Cybio Well Vario liquid handler. 2 mM compounds were stored in 100% DMSO in 384 well plates. Wells were homogenized with a Bioshake 3000 ELM orbital shaker at 2,400 rpm for 45 sec and condensates were allowed to settle for 30 min before scanning. Measurements were taken at 355 nm with a EnVision 2104 multilabel plate reader (PerkinElmer). No Protein control data was used for background subtraction prior to upload to CCDvault for normalization to DMSO vehicle control wells. Compounds with confirmed data that have normalized absorbance values of less than 0.164 were chosen for dose response. Wells that exhibit three standard deviations from the untreated sample and a No Protein control were selected for dose-response screening. The same His-tagged FSP1(WT) protein were tested against candidate drugs using a 10-point serial dilution starting at 40 µM using the same procedure.

For the cell-based screen, cells were seeded in triplicate at a density of 1000-1500 cells per 50 µL per well in black 384-well plates (Thermo Fisher Scientific, Cat# 142761) and (Corning, Cat# CLS3985) 24 hr before start of imaging. After 24 hr, an additional 50 µL of drug infused medium containing 30 nM SYTOX Green Dead Cell Stain was carefully placed into the wells on top of existing medium. The plates were immediately transferred to an IncuCyte S3 imaging system (Essen Bioscience) enclosed in an incubator set to 37°C and 5% CO_2. One image per well were captured in the phase, green, and red channels every 1.5 or 3 hr over a 24 hr period, and the ratio of SYTOX Green-positive objects (dead cells) to SYTOX Green-positive plus Sg-SAFE mCherry-positive objects (total cells) was quantified using S3 image analysis software (Essen Bioscience). For each treatment condition, the SYTOX-to-'SYTOX+mCherry'-object ratio was plotted against the 24 hr imaging interval, the Area Under the Curve (AUC) was calculated and the average AUC was plotted using Prism (GraphPad). To calculate the half-maximal effective concentration (EC_{50}) values, the AUC curve was fit to a variable slope function comparing response to drug concentration.

3.4.6 Lipid peroxidation assay

Cells seeded in a 6-well plate were treated with 200 nM RSL3 for 5 hr and washed once with DPBS containing calcium and magnesium (Gibco, Cat# 14040117). Cells then were incubated in DPBS containing 5 µM BODIPY 581/591 C11 (Invitrogen, Cat# D3861) at 37°C for 10 min and washed 3x with DPBS without calcium or magnesium (Gibco, Cat# 14190144). Cells were detached from the plate with trypsin, and green fluorescence was analyzed by flow cytometry (>10,000 cells) on a BD LSRFortessa. Data were analyzed using FlowJo.

3.4.7 Spheroid / 3D cell culture

2500 NCI-H460 cells with 100 µL full serum RPMI media were seeded in 96-well Black/Clear Round Bottom Ultra-Low Attachment Spheroid Microplate (Corning, Cat# 4515). Cells were incubated at 37°C for 30 min before another 100 µL RPMI media containing 2% Matrigel (Corning, Cat# 354234) was added. Plates were centrifuged at 750x g for 15min and grew at 37°C for 2 days. For FSEN1 and RSL3 treatment, 100 µL RPMI media was slowly removed without disturbing the spheroid. Another 100 µL RPMI media containing 1% Matrigel, 60 nM SYTOX Green dye, 10 µM FSEN1 or 10 µM RSL3 or both was added back into each well. Spheroids were imaged in IncuCyte S3 with a 10x objective.

3.4.8 FDA and Bioactive Library Screen, FSP1KO + mFSP1 overexpression and Synergy experiments

For the FDA and Bioactive Library Screen, FSP1KO + mFSP1 overexpression and Synergy experiments, cells were seeded at a density of 1500 cells per 25 µL per well in black 384-well plates (Thermo Fisher Scientific, Cat# 142761), (Corning, Cat# CLS3985), and (Grenier Bio, Cat# 781091) 24 hr before start of imaging. After 24 hr, an additional 25 µL of drug infused medium containing 30 nM SYTOX Green Dead Cell Stain was

carefully placed into the wells on top of existing medium. The plates were immediately transferred to an IncuCyte S3 imaging system (Essen Bioscience) enclosed in an incubator set to 37°C and 5% CO_2. One image per well were captured in the phase, green, and red channels every 4 hr over a 24 hr period, and the ratio of SYTOX Green-positive objects (dead cells) to SYTOX Green-positive plus mCherry-positive objects (total cells) was quantified using S3 image analysis software (Essen Bioscience). For each treatment condition, the SYTOX-to-'SYTOX+mCherry'-object ratio was plotted against the 24 hr imaging interval, the Area Under the Curve (AUC) was calculated, and the average AUC was plotted as a function of drug concentration (for example, RSL3) using Prism (GraphPad). To calculate the half-maximal effective concentration (EC_{50}) values, the AUC curve was fit to a variable slope function comparing response to drug concentration.

3.4.9 Compound preparation for synergy experiments

Vehicle, RSL3 and DHA combinations were stamped in grid format 1:1 at 4x concentrations. The compounds were then diluted with SYTOX green infused media containing either vehicle, 0.10 µM, 1 µM, or 10 µM FSEN1 to the appropriate 2x concentration (PlateOne, Cat# 1884-2410). Compounds were then homogenized with a Bioshake 3000 ELM orbital shaker at 2,400 rpm for 45 sec prior to treatment.

3.4.10 Protein expression and purification

Expression vectors were transformed into LOBSTR-BL21 (DE3) competent cells (Kerafast, Cat# EC1002) and LB broth was inoculated for overnight growth at 37°C while shaking at 280 rpm. The following day, the cultures were diluted 1:100 into 1L LB broth and allowed to grow at 37°C while shaking at 280 rpm until the cultures reached an optical density at 600 nm (OD_{600}) of 0.6, measured by NanoDrop One (Thermo Fisher Scientific, Cat# 13-400-518). The cultures were then induced with 0.7 mM isopropyl β-D-1-thiogalactopyranoside (IPTG) and grown at 30°C while shaking at 280 rpm overnight. Cultures were then centrifuged for 45 min at 4°C and 4500 rpm to pellet. 1L Bacterial pellets were resuspended in 25 mL lysis buffer (50 mM KH_2PO_4, 300 mM KCl, 10% glycerol, 30 mM imidazole, 1 mg/mL lysozyme, and 1 mM PMSF, pH 8.0) and incubated at 37°C while shaking at 280 rpm for 10 min. The resuspended cells were lysed by passing through a microfluidizer (Microfluidics model: LM10) 3× at 15,000 PSI and collected in an ice-bath-chilled beaker. Lysate was then ultracentrifuged for 30 min at 4°C and 50,000 x g. All subsequent purification steps were carried out at 4°C. The supernatant was passed through an Econo-Pac disposable chromatography column (Bio-Rad Cat: 732-1010) packed and equilibrated with 1 mL HisPur Ni-NTA agarose resin (Thermo Fisher Scientific, Cat# 88221) and washed 4× with 2 mL EQ buffer (50 mM KH_2PO_4, 300 mM KCl, 10% glycerol, and 30 mM imidazole, pH 8.0). Bound proteins were eluted from Ni-NTA resin bed by gravity flowing 5 mL elution buffer (50 mM KH2PO4, 300 mM KCl, 10% glycerol, 250 mM imidazole, pH 8.0) through the column. Using an Amicon Ultra-15 centrifugal filter (Sigma-Aldrich, SKU: UFC910008), the eluted proteins were buffer exchanged into SEC buffer (50 mM HEPES, 100 mM KCl, 2 mM DTT, pH 8.0), spiked with 15% glycerol and 10 mM DTT and further concentrated to 3 mL total volume. Protein sample was then further purified by gel filtration through a HiLoad 16/600 Superdex 75

Pg size exclusion chromatography column (Sigma-Aldrich, SKU: GE28-9893-33) in SEC buffer using a GE Akta Pure FPLC. Fractions were collected in 1.6 mL aliquots and combined based on purity, visualized by Coomassie staining after separation in SDS-page. Combined fractions were then concentrated to 2 mg/mL and snap-frozen in 50 µL aliquots using liquid nitrogen. Protein concentration was determined using a Pierce bicinchoninic acid (BCA) protein assay kit (Thermo Fisher Scientific, Cat# PI23227).

3.4.11 FSP1 Kinetics (CoQ1 and CoQ-Coumarin)

To measure FSP1 kinetics, FSEN1 was dissolved and diluted in DMSO, and recombinant purified FSP1 was diluted in PBS. 0.5 µL FSEN1 and 12.5 µL FSP1 were mixed and incubated for 30 min in a NBS polystyrene 384-well plate (Corning, Cat# CLS3640) at RT. Vehicle control wells included 0.5 µL DMSO and were absent of any FSEN1. NADH (Millipore Sigma, Cat# 481913) was then dissolved and diluted in PBS and added to the plate wells. CoQ-Coumarin (Cayman Chemical, Cat# 29554) was dissolved in DMSO, diluted in PBS, and added to the plate wells to start the reaction. For NADH kinetics the final well volume was 25 µL, and final concentrations were 25 nM FSP1, 10 µM CoQ-Coumarin, 1-50 µM NADH, and 50-500 nM FSEN1. For CoQ-Coumarin kinetics the final well volume was 25 µL, and final concentrations were 6.25 nM FSP1, 1-30 µM CoQ-Coumarin, 200 µM NADH, and 12.5-125 nM FSEN1. Reduced CoQ-Coumarin fluorescence (Ex: 405 nm, Em: 475 nm) was measured as read-out of enzymatic product formation on a kinetic cycle with an interval time of 15 sec at RT. All data was acquired using a Tecan Spark. For CoQ1 final well volume was 25 µL, and final concentrations were 25 nM FSP1, 200-500 µM CoQ1, 500 µM NADH, and 0.05-1 µM FSEN1. NADH Absorbance (355 nm) was measured as an inverse read-out of enzymatic product formation on a kinetic cycle with an interval time of 3 min at RT. All data was acquired using a Tecan infinite M1000.

3.4.12 FSP1 and NQO1 % Activity Curves

To measure in vitro activity of FSP1 and NQO1 for IC_{50} calculation, recombinant purified FSP1 and NQO1 were diluted in PBS. FSEN1 was dissolved and diluted in DMSO, and 0.5 µL FSEN1 and 12.5 µL FSP1 or NQO1 respectively, were mixed on an orbital shaker for 45 sec at 450 rpm and incubated for 30 min in in a NBS polystyrene 384-well plate (Corning, Cat# CLS3640) at RT. NADH (Millipore Sigma, Cat# 481913) was dissolved and diluted in PBS, and CoQ1 (Sigma-Aldrich, Cat# C7956) was dissolved in DMSO and diluted in PBS. Diluted NADH and CoQ1 were combined into a 2X reaction mix and added to the plate wells to start the reaction. Final well volume was 25 µL, and final concentrations were 12.5 nM FSP1, 400 µM CoQ1, 500 µM NADH, and 0.01-20 µM FSEN1. NADH Absorbance (355 nm) was measured as an inverse read-out of enzymatic product formation on a kinetic cycle with an interval time of 2.5 min at RT. All data was acquired using a Tecan infinite M1000. Raw data from three biological replicates were then plotted and initial slopes were calculated using a linear regression in prism (GraphPad). All rates were normalized to vehicle and No Protein controls where the highest and lowest slope values were used as 0 and 100%. Normalized values were then plotted as a function of FSEN1 concentration in log scale, and prism (GraphPad) was

used to perform a non-linear regression curve fit for log (inhibitor) vs. normalized (variable) slopes. IC_{50} values of FSEN1 for FSP1 and NQO1 were obtained from this non-linear regression. Specific activity rates were determined for human and mouse (*Mus musculus*) FSP1 (FSP1 and mFSP1) by measuring NADH Absorbance (355 nm) over time, and similar specific activities were utilized. As such, 125 nM mFSP1 was used to match the specific oxidoreductase activity of 12.5 nM FSP1. Raw data for mFSP1 activity was acquired and analyzed with identical methods to acquisition and analysis of FSP1 to determine percent activity.

3.4.13 Western blotting

Cells were washed two times with PBS prior to lysis in 1% SDS. Samples were then sonicated for 30 sec and incubated for 5 min at 100°C. Protein concentrations were determined using the bicinchoninic acid (BCA) protein assay (Thermo Fisher Scientific, Cat# PI23227), and equal amounts of protein by weight were combined with 1× Laemmli buffer, separated on 4–20% polyacrylamide gradient gels (Bio-Rad Laboratories) and transferred onto nitrocellulose membranes (Bio-Rad Laboratories). Membranes were washed in PBS with 0.1% Tween-20 (PBST) and blocked in PBST containing 5% (w/v) dried milk or 5% (w/v) bovine serum albumin (BSA) for 30 min. Membranes were incubated for 24 hr in PBST containing 5% BSA (Akron Biosciences) and primary antibodies. After washing with PBST, membranes were incubated at room temperature for 30 min in 5% BSA and PBST containing fluorescent secondary antibodies. Immunoblots were imaged on a LI-COR imager (LI-COR Biosciences).

The following blotting reagents and antibodies were used: anti-AMID (Santa Cruz Biotechnology, Cat# sc-377120), anti-AIFM2 (LS bio, Cat# LS-C382008-50), anti-β-actin (Santa Cruz Biotechnology, Cat# sc-47778), anti-GPX4 (Abcam, Cat# ab125066), anti-ACSL4 (Sigma-Aldrich, Cat# SAB2701949), anti-GAPDH (EMD Millipore Corp, Cat# MAB374), anti-rabbit IRDye800 conjugated secondary (LI-COR Biosciences, Cat# 926-32211) and anti-mouse Alexa Fluor 680 conjugated secondary (Invitrogen, Cat# A32723).

3.4.14 In Vivo Pharmacokinetics

Gonadally intact adult male BALB/c mice (*n*=5) weighing 20-25 gm were used to characterize the in vivo pharmacokinetics of FSEN1. Mice were group-housed, five per cage, in a temperature-controlled (22°C) vivarium on a 12 hr/12 hr light/dark cycle with ad libitum access to food and water. Each mouse received a single 20 mg/kg FSEN1 dose administered (I.P.) in a 20% DMSO, 20% Ethanol, 20% PEG40, 40% PBS solution. Whole blood samples were collected via retro-orbital bleeds at 0.5, 1, 2, 4, 8 and 24 hr post-dose. Samples were processed to plasma and FSEN1 concentrations were quantitated using liquid chromatography with tandem mass spectrometry (LC-MS/MS). FSEN1 standards were prepared in blank mouse plasma and used to generate an external calibration curve using linear regression to plot the peak area ratio versus concentration with 1/x weighting ($r2 \geq 0.99$) over the analytically reportable range (9.8 – 313 ng/mL). Pharmacokinetic data were analyzed using non-compartmental methods. All animal procedures were conducted in strict adherence to the National Institutes of Health

Guide for the Care and Use of Laboratory Animals and approved by the University of California San Diego Institutional Animal Care and Use Committee (IACUC).

3.4.15 Metabolic stability in mouse liver microsomes

FSEN1 was incubated at a concentration of 2 μM in 0.5 mg/mL mouse liver microsomes (Xenotech, Cat# M1000). The reaction mixture contained 1.0 mM NADPH. Incubations were performed in triplicate in a final volume of 1.5 mL at 37°C. The incubation system without NADPH was used as a negative control, while midazolam (2 μM) was used as a positive control. Incubation was stopped at 0, 5, 15, 30 and 45 min by taking an aliquot of the reaction mixture and adding it to cold acetonitrile containing the analytical internal standard. Peak area of each analyte was determined by LC-MS/MS and used to calculate % remaining. The natural log (ln) of % remaining was plotted versus incubation time and the elimination rate constant (k) was calculated from linear regression. Half-life (t1/2) was calculated as ln2/k. Intrinsic clearance (CL_{int}, μL/min/mg protein) was calculated as ln2/t1/2 x [volume of incubation (μL)/microsomal protein in incubation (mg)].

3.4.16 Quantification and statistical analysis

Lethal fraction scoring was performed using Microsoft Excel 16.71 (Microsoft Corporation, Redmond, WA). Lethal fraction, in vitro, and in vivo assay plotting and curve fitting were performed using Prism 9.5.1 (GraphPad Software, La Jolla, CA). Flow cytometry data were processed using FlowJo (V10.6.1) (FlowJo LLC, Ashland, OR). Synergy scoring and plotting were performed in RStudio version 2022.07.0 Build 548 using the SynergyFinder R package available from Bioconductor. Figures were assembled using Adobe Illustrator (Adobe Systems, San Jose, CA). Statistical details of experiments and statistical tests used can be found in the main text, figure legends, and STAR Methods.

Limitations of the study:
Our findings indicate that FSEN1 directly inhibits recombinant human FSP1 activity in vitro and inhibits FSP1 suppression of ferroptosis in cultured cancer cells. Although the in vivo pharmacokinetics and metabolic stability of FSEN1 suggest that FSEN1 is suitable for in vivo studies, it remains to be determined whether FSEN1 inhibits FSP1 in vivo and whether FSEN1 treatment has any effect on tumor growth. Furthermore, because FSEN1 appears to be selective for human FSP1, it may not be useful for studying the role of mFSP1 or tumor growth in Genetically Engineered Mouse Models (GEMM) models. It will be important to determine if other FSP1 inhibitors discovered in this study inhibit mFSP1 and to determine their impact on preclinical models of tumor growth.

SIGNIFICANCE:
Emerging evidence suggests that induction of ferroptosis has value for the treatment of therapy-resistant cancers. FSP1 functions as a key cellular defense factor that promotes ferroptosis resistance in cancer. Here, we report the discovery of several structurally diverse FSP1 inhibitors that increase the sensitivity of cancer cells to ferroptosis in vitro. The most potent of these inhibitors, FSEN1 synergizes with multiple ferroptosis inducers and exhibits pharmacokinetics and metabolic stability suitable for in vivo studies. Our

findings provide valuable chemical inhibitors of FSP1 that will be useful for studying the cellular mechanisms of ferroptosis and exploring the potential of FSP1 as a therapeutic target in cancer.

Key resources table

REAGENT or RESOURCE	SOURCE	IDENTIFIER
Antibodies		
Mouse monoclonal Anti-AMID	Santa Cruz Biotechnology	Cat# sc-377120
Mouse monoclonal Anti-β-actin	Santa Cruz Biotechnology	Cat# sc-47778
Rabbit polyclonal Anti-GPX4	Abcam	Cat# ab125066
Rabbit polyclonal Anti-ACSL4	Sigma-Aldrich	Cat# SAB2701949
Rabbit polyclonal Anti-AIFM2	LS Bio	Cat# LS-C382008-50
Mouse monoclonal Anti-GAPDH	EMD Millipore Corp	Cat# MAB374
Bacterial and virus strains		
LOBSTR-BL21 (DE3) competent cells	Kerafast	Cat# EC1002
Stbl3 competent cells	Macrolab at UC Berkeley	N/A
NEB 5DH-α	NEB	Cat# C278H
Biological samples		
Mouse microsomes	Xenotech	Cat# M1000
Chemicals, peptides, and recombinant proteins		
RSL3	Cayman Chemical	Cat# 19288
Fer-1	Cayman Chemical	Cat# 17729
Idebenone	Cayman Chemical	Cat# 15475
Deferoxamine mesylate (DFO)	Cayman Chemical	Cat# 14595
ML162	Cayman Chemical	Cat# 20455
ZVAD(OMe)-FMK	Cayman Chemical	Cat# 14463
Necrostatin-1	Cayman Chemical	Cat# 11658
Dihydroartemisin (DHA)	Selleck Chemical	Cat# S2290
Puromycin	Thermo Fisher Scientific	Cat# A1113802
SYTOX Green Dead Cell Stain	Thermo Fisher Scientific	Cat# S34860
Polybrene	Sigma-Aldrich	Cat# TR-1003
Coenzyme Q_1	Sigma-Aldrich	Cat# C7956
CoQ-Coumarin	Cayman Chemical	Cat# 29554

Resazurin	Thermo Fisher Scientific	Cat# R12204
Bodipy C11	Thermo Fisher Scientific	Cat# D3861
NADH	Millipore Sigma	Cat# 481913
Small Molecule Library	ChemDiv	N/A
FDA-Approved Drug Library	TargetMol	Cat# L4200
Bioactive Compound Library	TargetMol	Cat# L4000
Hygromycin	Thermo Fisher Scientific	Cat# J67371.XF
Bleomycin	Thermo Fisher Scientific	Cat# J60727.MCR
Recombinant FSP1 (Human)	This Study	N/A
Recombinant FSP1 (Mouse)	This Study	N/A
Critical commercial assays		
CellTiter Glo Luminescent Cell Viability Assay	Promega	Cat# G7572
Pierce BCA Protein Assay Kit	Thermo Fisher Scientific	Cat# PI23227
PCR Cloning System with Gateway® Technology	Thermo Fisher Scientific	Cat# 12535-029
Experimental models: Cell lines		
Human: NCI-H460	ATCC	HTB-177
Human: A375	UC Berkeley Cell Culture Facility	N/A
Human: HCC1143	UC Berkeley Cell Culture Facility	N/A
Human: Huh7	UC Berkeley Cell Culture Facility	N/A
Human: SU-DHL-5	ATCC	CRL-2959
Human: RL	ATCC	CRL-2261
Human: NCI-H460^{C}	This Study	N/A
Human: A549^{N}	Forcina et al. 2022	N/A
Human: HCC1143^{C}	Li et al. 2022	N/A
Human: NCI-H460^{C} GPX4^{KO}	This Study	N/A
Human: NCI-H460^{C} FSP1^{KO}	This Study	N/A
Human: HT-1080^{N}	Forcina et al. 2022	N/A
Human: U-2OS^{N}	Forcina et al. 2022	N/A
Human: T98G^{N}	Forcina et al. 2022	N/A
Human: Huh7^{C}	This Study	N/A

Human: 501-MEL	Kind gift from Imanol Arozarena Martinicorena at Navarrabiomed	N/A
Human: SKMEL28	Kind gift from Imanol Arozarena Martinicorena at Navarrabiomed	N/A
Human: NCI-H460^{C} FSP1^{KO} mFSP1 OE	This Study	N/A
Experimental models: Organisms/strains		
BALB/c mice	Envigo	N/A
Oligonucleotides		
See Table S1		
Recombinant DNA		
pET-His6-TEV vector	Addgene	Cat# 29653
hFSP1-pET-His6-TEV vector	Bersuker et al. 2019	N/A
mFSP1-pET-His6-TEV vector	This paper	N/A
NQO1-pET-His6-TEV vector	This paper	N/A
GenEZ ORF Clone: Aifm2_OMu13438D_pcDNA3.1+/C-(K)-DYK	GenScript	Cat# SC1200
CSII-prEF1a-mCherry-3xNLS	Addgene	Cat# 125262
mCherry pMCB320	Addgene	Cat# 89359
pENTR1A-GFP-N2	Addgene	Cat# 19364
mFSP1-pENTR1A	This paper	N/A
pLenti CMV mFSP1 Hygro	This paper	N/A
Software and algorithms		
Prism 9	GraphPad Software	N/A
R Studio	Posit Software, PBC	https://posit.co/download/rstudio-desktop/
Microsoft Excel	Microsoft Corporation	N/A
FlowJo	Becton, Dickinson & Company	N/A
SynergyFinder R package	Bioconductor	https://www.bioconductor.org/packages/release/bioc/html/synergyfinder.html

3.5 Figures

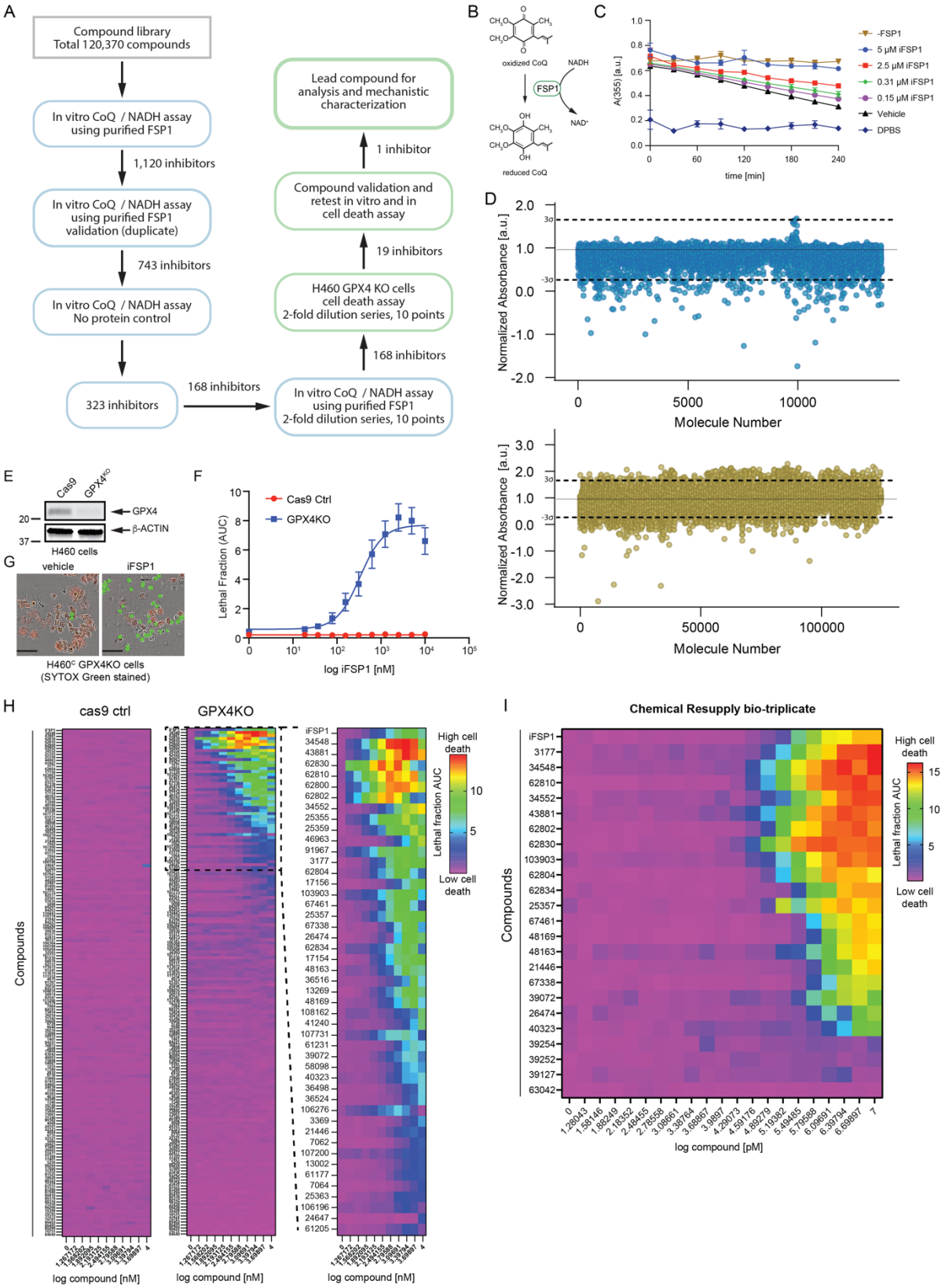

Figure 3-1 Small molecule screens identify FSP1 inhibitors

(A) Flow chart of the chemical screens and experimental validation employed to identify FSP1 inhibitors. (B) Schematic of the in vitro activity assay using purified recombinant FSP1. (C) FSP1 activity was measured using NADH absorbance in the presence of increased amounts of iFSP1. Data are mean ± SEM (n = 3 technical replicates). (D) Scatterplots of 15,000 antibacterial compounds and 100,000 diverse + 5,370 FDA and Bioactive compounds assayed with in vitro absorbance-based assay of FSP1 activity. ‘‘Hits’’ are defined by a normalized absorbance value of <0.267. Dashed lines represent SD of 3-sigma cutoff defined by activity range of vehicle and no protein control. (E) Western blot analysis of $H460^{C}$ Cas9 and $GPX4^{KO}$ cells. (F) Representative images of H460 $GPX4^{KO}$ cells treated with vehicle and iFSP1. Dead cells are marked with SYTOX Green. Scale bar represents 50 μm. Images from one of three independent experiments are shown. (G) Dose response of iFSP1 induced cell-death in $H460^{C}$ Cas9 and $GPX4^{KO}$ cells. Lethal fraction (LF) was calculated by IncuCyte quantification of the ratio of dead cells over the total amount of cells over 24 hr. Data are mean ± SEM (n = 3 biological replicates). (H) LF (the Area Under the Curve [AUC]) was calculated in $H460^{C}$ Cas9 and $GPX4^{KO}$ cells incubated with increasing doses of 168 small molecules that inhibited FSP1 in vitro. The heatmap reflects mean values from n = 3 biological replicates. (I) LF was calculated $H460^{C}$ $GPX4^{KO}$ cells incubated with increasing doses of the most potent 19 FSP1 inhibitors and iFSP1. Resupplied, validated small molecules were used. The heat map reflects mean values from n = 3 biological replicates.

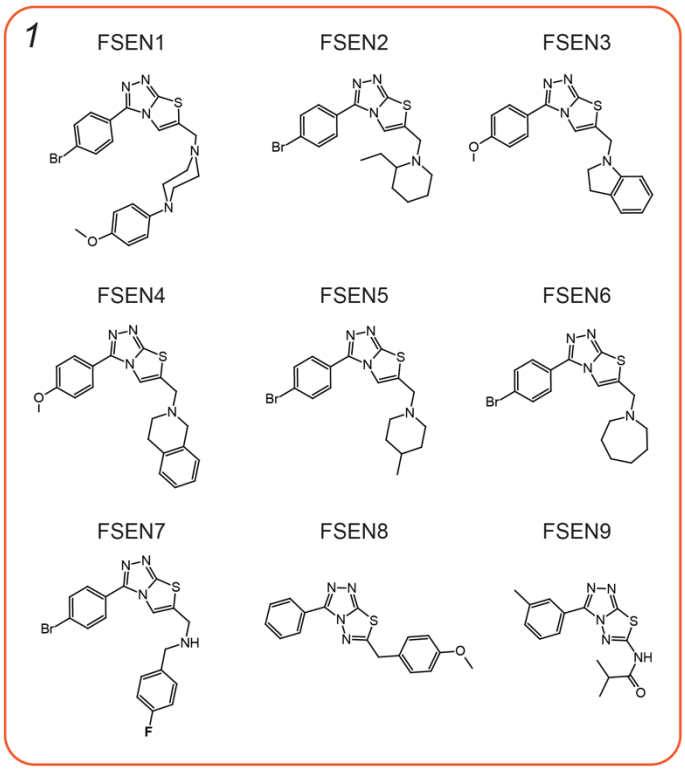

Compound	Biochemical IC_{50} (nM)	Cellular EC_{50} (nM)
FSEN1	313	69.363
FSEN2	1150	124.960
FSEN3	90.1	150.203
FSEN4	738	221.345
FSEN5	822	239.845
FSEN6	786.5	290.882
FSEN7	1575	785.278
FSEN8	1003	1753.723
FSEN9	667	5190.714
FSEN10	25000	994.478
FSEN11	39200	1746.624
FSEN12	14300	121.765
FSEN13	606	302.612
FSEN14	1360	333.298
FSEN15	1680	676.044
FSEN16	738	127.878
FSEN17	14100	2679.986
FSEN18	7440	761.134
FSEN19	127.878	1582.887

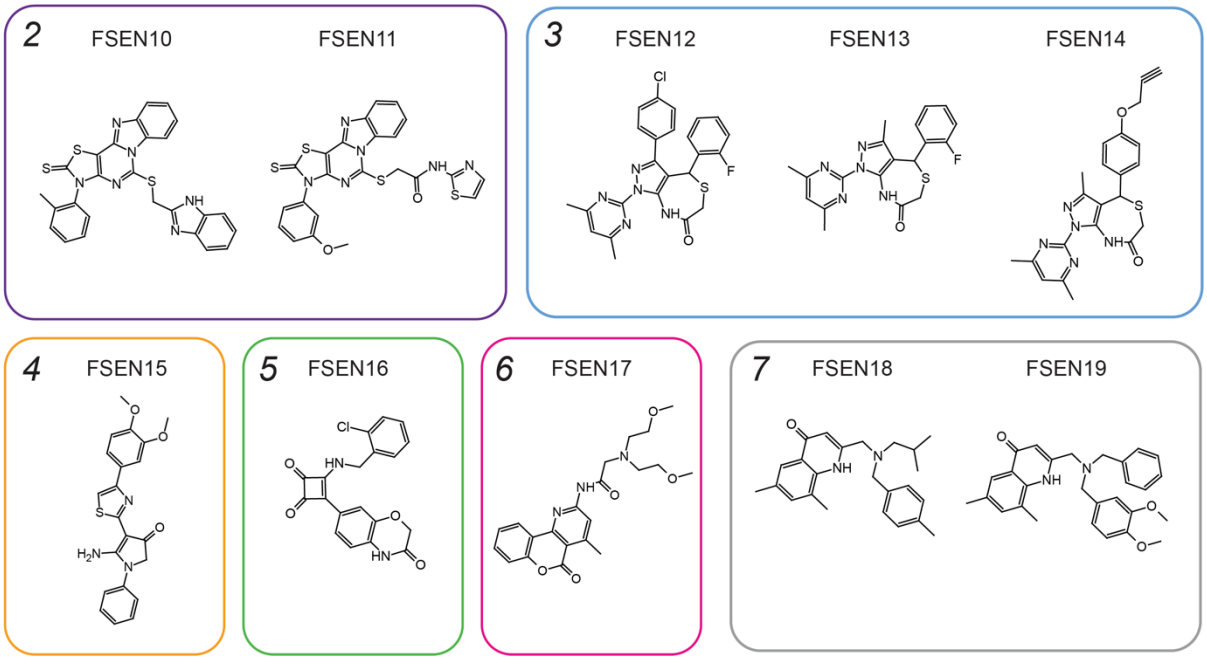

Figure 3-2 Multiple structurally distinct FSP1 inhibitor scaffolds

The structures of FSEN1-19 are shown with their calculated IC50 values from end-point assays measuring inhibition of FSP1 activity in vitro (n = 2 independent replicates) and

their calculated EC50 values from lethal fraction (AUC) quantification in $H460^{C}$ $GPX4^{KO}$ cells (n = 3 cell biological replicates).

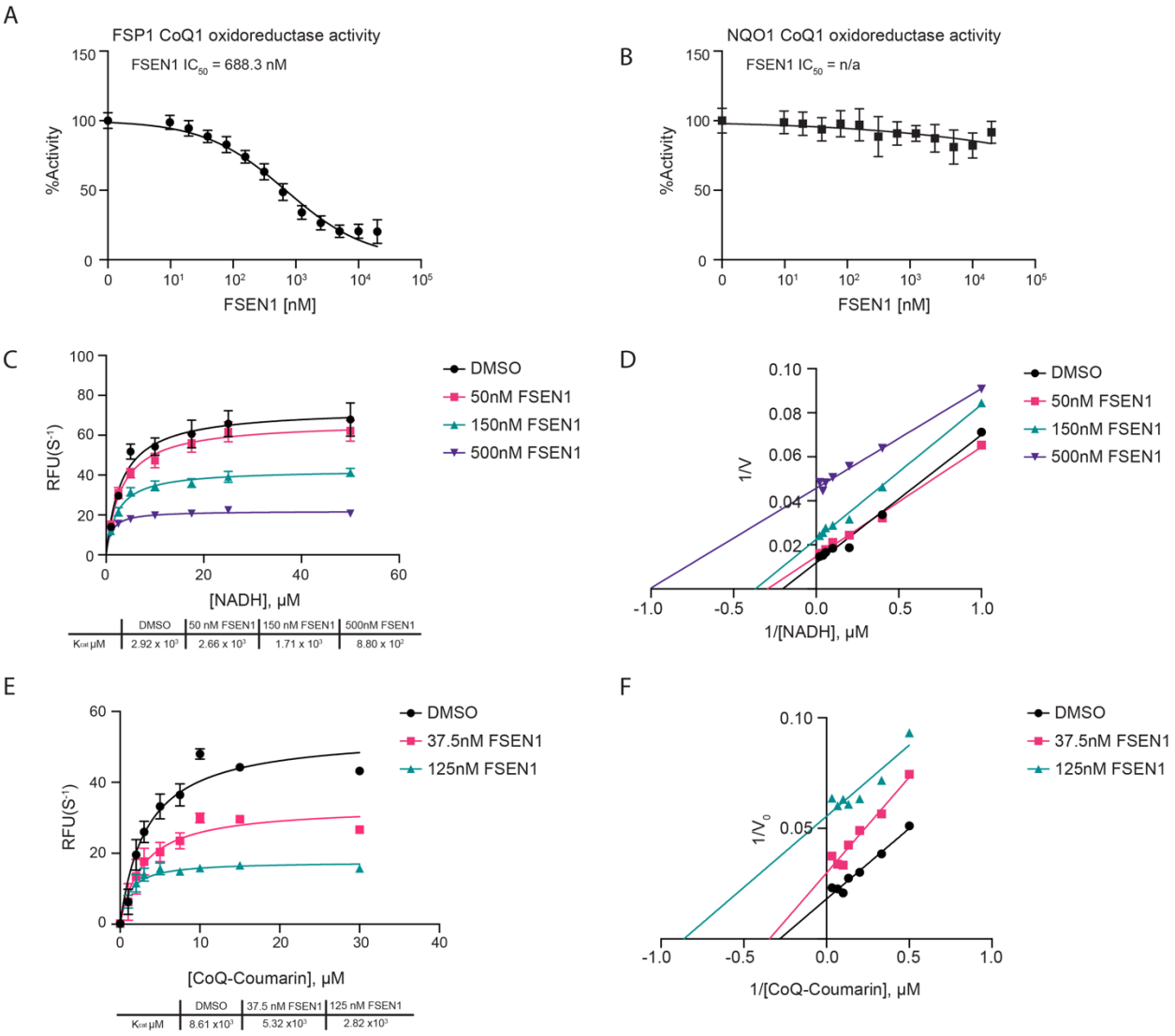

Figure 3-3 Mechanisms of inhibition of FSP1 by FSEN1

(A and B) Purified recombinant FSP1 (A) and NQO1 (B) CoQ1 oxidoreductase activities were measured in the presence of increasing concentrations of FSEN1. Data were normalized to the slopes calculated from DMSO and no protein controls. IC50 values displayed in nM were calculated from a non-linear regression curve fit. Data are mean ± SEM bars (n = 3 independent replicates). (C and D) Michaelis-Menten and Lineweaver-Burk plots of FSP1 treated with increasing concentrations of NADH in the presence of vehicle or FSEN1. 10 µM CoQ-Coumarin was used as the co-substrate for FSP1, and reduced CoQ-Coumarin fluorescence was measured as a readout of enzymatic product formation. Error bars represent linear regression standard error of initial rates (n = 3 independent replicates). Vmax and Km were calculated from the non-linear regression curve fit. (E and F) Michaelis-Menten and Lineweaver-Burk plots of FSP1 treated with increasing concentrations of CoQ-Coumarin in the presence of vehicle or FSEN1. 200

μM NADH was included as a co-substrate for FSP1, and reduced CoQ-Coumarin fluorescence was measured as the readout of enzymatic product formation. Error bars represent linear regression standard error of initial rates (n = 3 independent replicates). Vmax and Km were calculated from the non-linear regression curve fit.

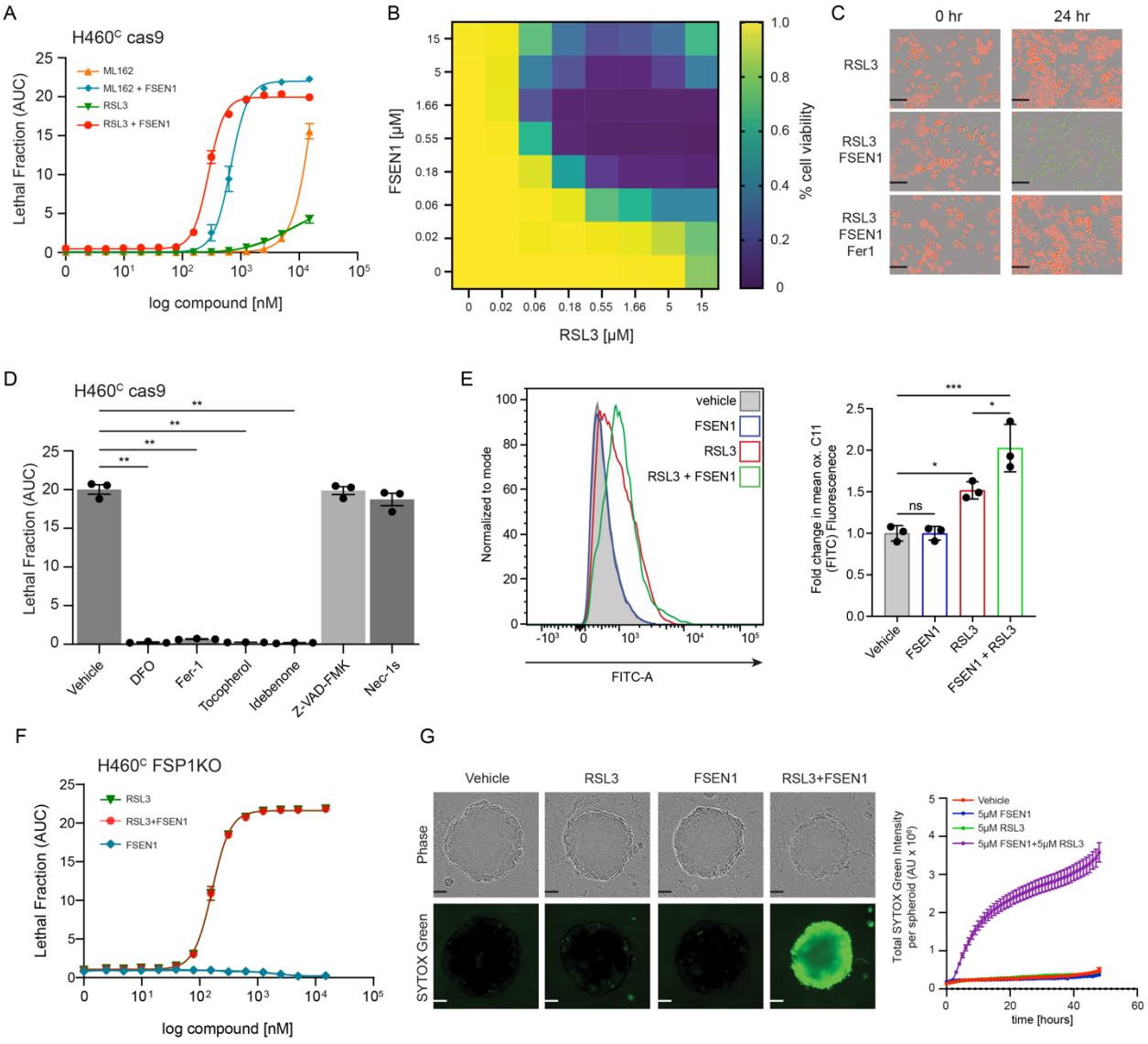

Figure 3-4 FSEN1 is synthetic lethal with GPX4 inhibitors and sensitizes cancer cells to ferroptosis

(A) Dose response of RSL3 and ML162-induced cell death in H460^{C} Cas9 cells co-treated with 1 µM FSEN1 and 2 µM Fer-1 where indicated. Data are mean ± SEM (n = 3 biological replicates). (B) Heatmap represents the fraction of viable H460^{C} Cas9 cells co-treated with increasing doses of FSEN1 and RSL3 (mean values from n = 3 biological replicates). (C) Representative images of H460^{C} Cas9 cells co-treated with 1.6 µM RSL3, 1 µM FSEN1, and 2 µM Fer-1 as indicated. Scale bar = 200 µm. Images from one of three independent experiments are shown. (D) Lethal Fraction (AUC) of 5 µM RSL3-induced cell death in H460^{C} Cas9 cells co-treated with 1 µM FSEN1 together with the indicated inhibitors of ferroptosis (Fer-1 [2 µM], DFO [100 µM], idebenone [10 µM], tocopherol [10 µM]), apoptosis (Z-VAD [10 µM]), and necroptosis (Nec-1s [1 µM]). Data are mean ± SEM (n = 3 cell biological replicates). **p < 0.01 by one-way ANOVA with Dunnett's multiple comparisons test. (E) Representative flow cytometry histogram (left panel) and

quantification (right panel) of $H460^{C}$ Cas9 cells treated with 200 nM RSL3 and/or 1 μM FSEN1 and labeled with the lipid peroxidation sensor BODIPY 581/591 C11. Green fluorescence intensity was analyzed by flow cytometry with the fluorescein isothiocyanate (FITC) channel. Data are mean ± SD (n = 3 biological replicates). *$p < 0.05$, ***$p = 0.0003$ by one-way ANOVA with Tukey's multiple comparisons test. (F) Dose response of RSL3-induced cell death in $H460^{C}$ $FSP1^{KO}$ cells co-treated with 1 μM FSEN1. Data are mean ± SEM (n = 3 biological replicates). (G) $H460^{C}$ spheroids were treated with vehicle, 5 μM FSEN1, and 5 μM RSL3 as indicated. Representative images from one of 20 independent experiments are shown. Scale bar represents 100 μm. The total intensity of the SYTOX green signal for each spheroid was quantified and the mean ± SEM plotted (n = 20 independent spheroids).

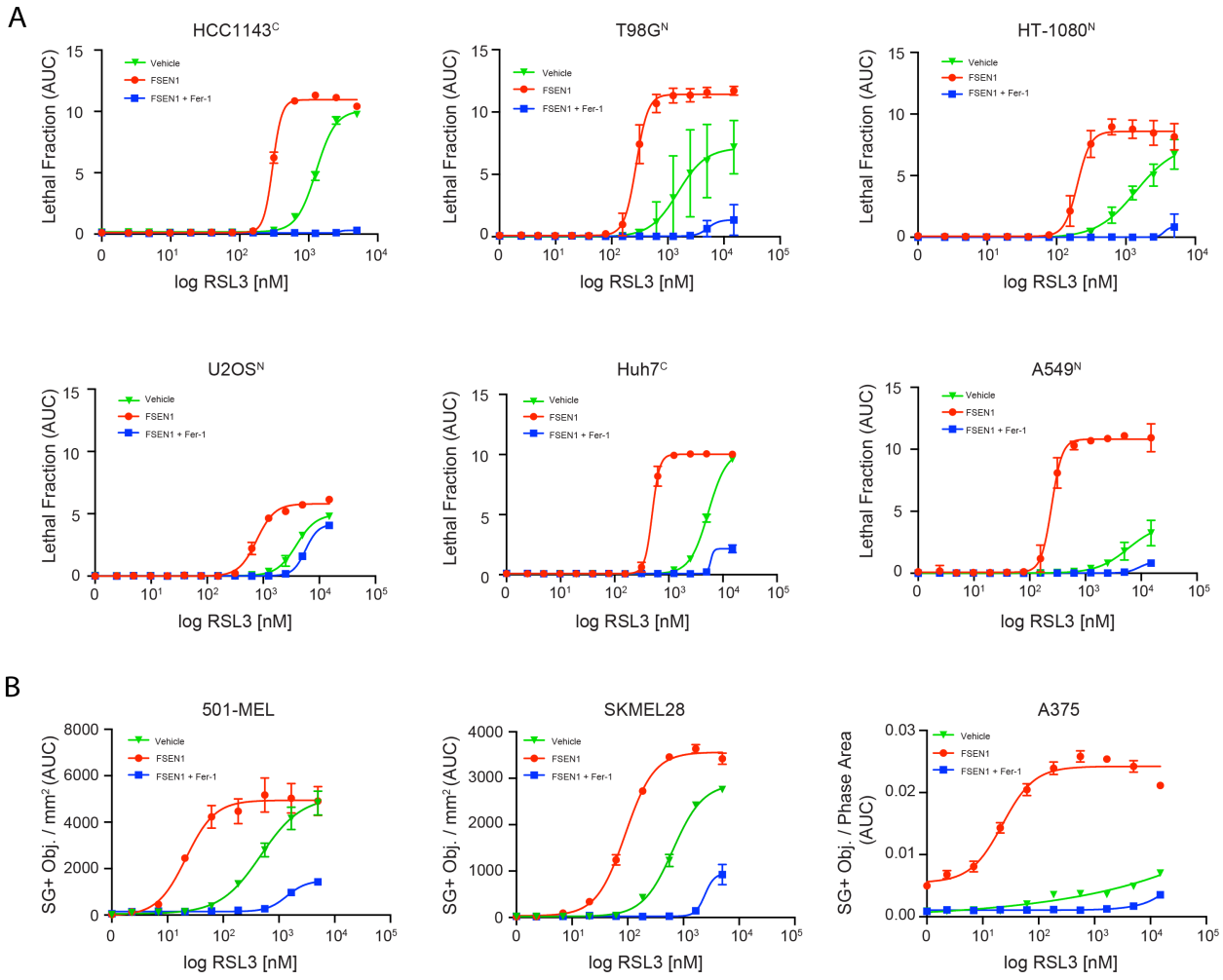

Figure 3-5 FSEN1 sensitizes cancer cells from different origins to ferroptosis

(A) Dose response of RSL3-induced cell death in the indicated cancer cell lines treated in the presence and absence of 1 μM FSEN1 and 2 μM Fer-1 as indicated. Data are mean ± SEM (n = 3 biological replicates). (B) Quantification of cell death in melanoma cell lines treated as in (A), calculated as SYTOX green positive object per mm^2. Data are mean ± SEM (n = 2 biological replicates).

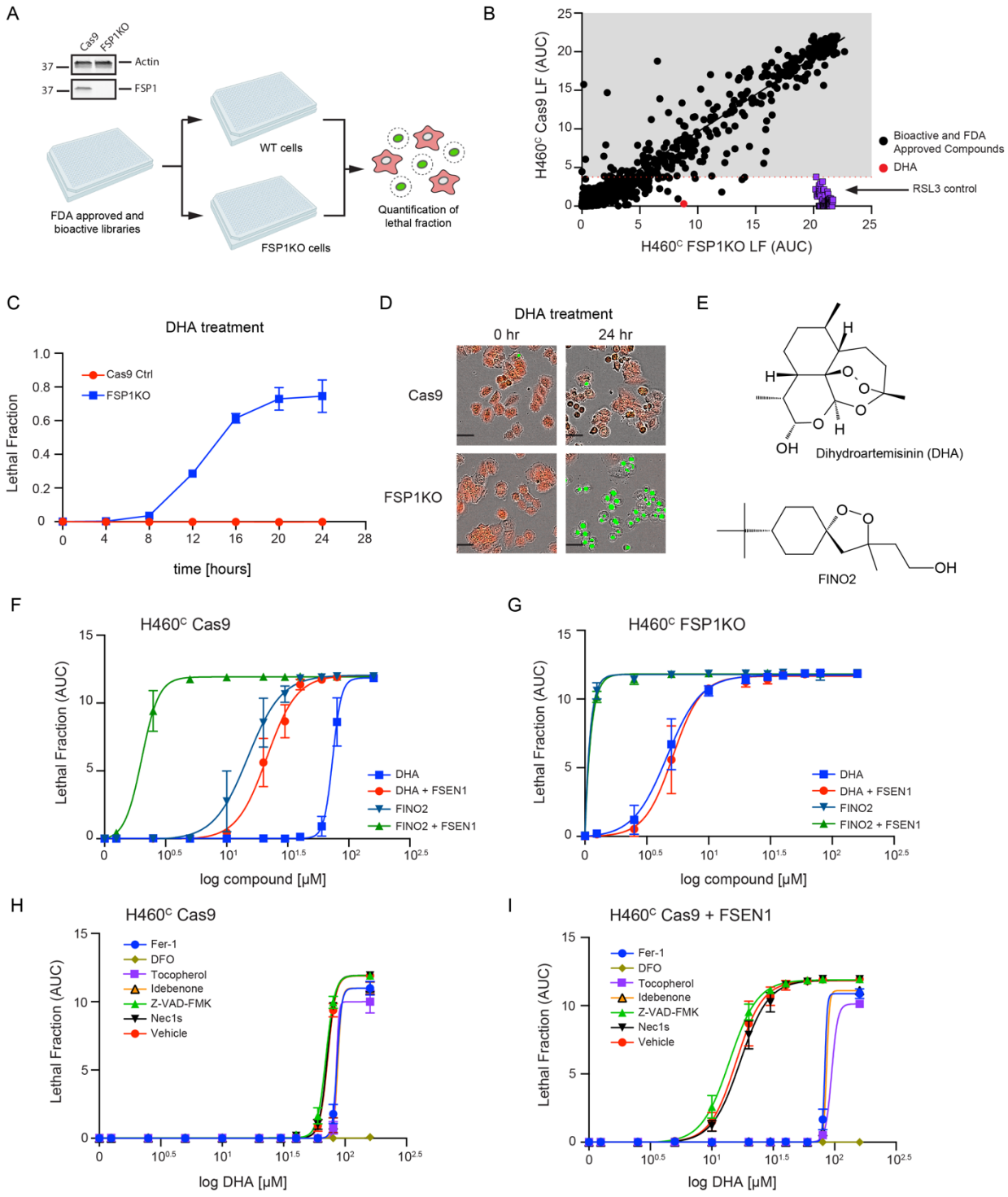

Figure 3-6 FDA library screens identify DHA as inducer of ferroptosis FSP1KO cells

(A) Western blot analysis of H460^{C} Cas9 and FSP1^{KO} cell lysates and screen schematic. H460^{C} Cas9 and FSP1^{KO} cells were incubated with 40 μM compounds and lethal fraction (LF) was quantified. (B) Scatterplot of the lethal fraction (LF) for each compound in H460^{C} Cas9 and H460^{C} FSP1^{KO} cells (n = 1 biological replicate). Red dotted line represents the

cutoff defined by the RSL3 positive control. (C) Dose response validation of LF over time comparing $H460^{C}$ Cas9 and $FSP1^{KO}$ cells treated with 40 μM DHA. (D) Representative IncuCyte images of $H460^{C}$ Cas9 and $FSP1^{KO}$ cells treated with DHA. Scale bar represents 50 μm. Images from one of two independent experiments are shown. (E) The chemical structures of DHA and FINO2. (F and G) Dose response of DHA and FINO2-induced cell death in $H460^{C}$ Cas9 (F) and $FSP1^{KO}$ (G) cells co-treated with vehicle or 1 μM FSEN1. Data are mean ± SEM (n = 2 biological replicates). (H and I) Dose response of DHA-induced cell death in $H460^{C}$ cells co-treated with vehicle (H) or 1 μM FSEN1 (I) together with the indicated inhibitors of ferroptosis (Fer-1 [2 μM], DFO [100 μM], idebenone [10 μM], tocopherol [10 μM]), apoptosis (Z-VAD [10 μM]), and necroptosis (Nec-1s [1 μM]). Data are mean ± SEM (n = 2 biological replicates).

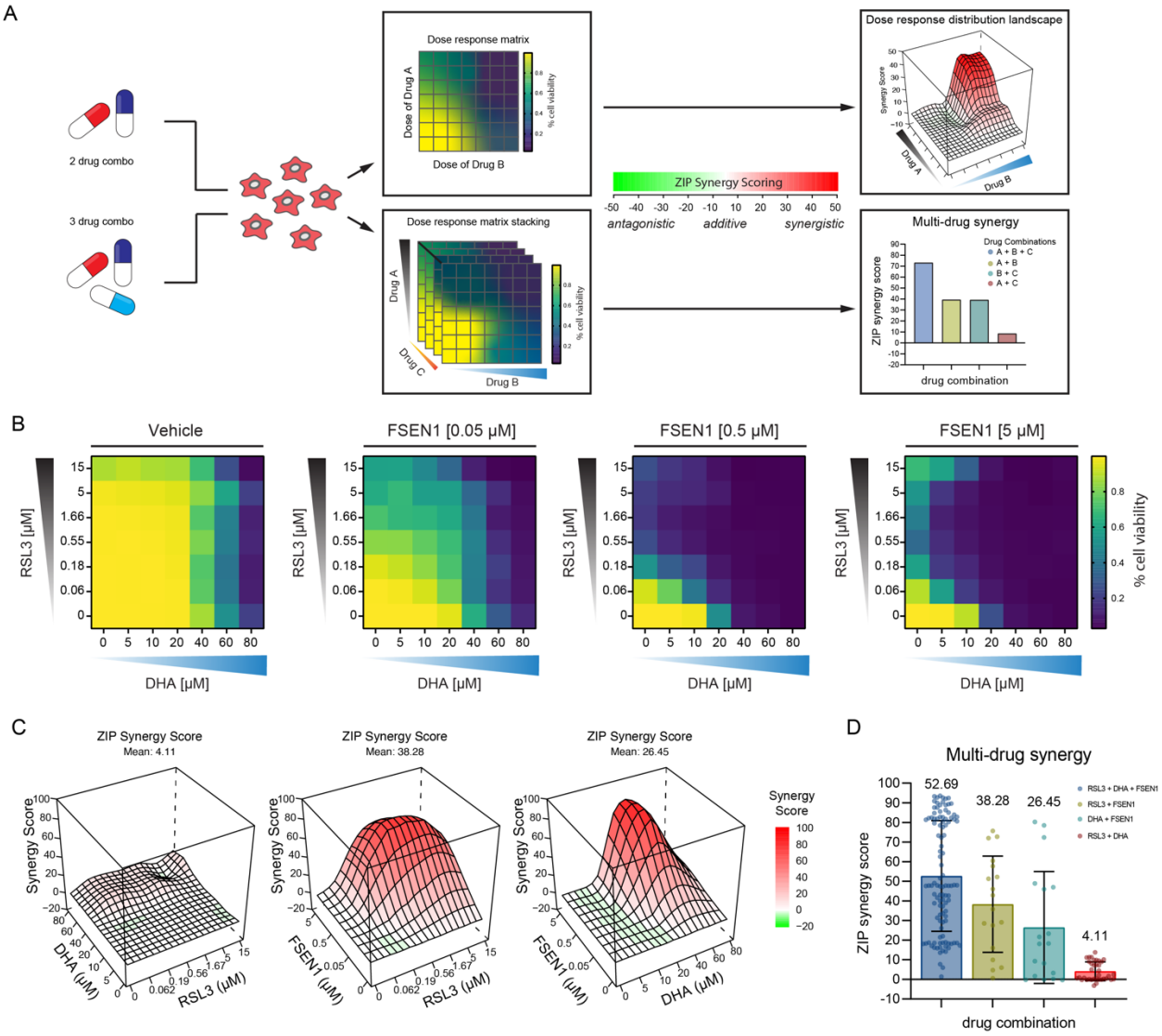

Figure 3-7 FSEN1 is synergistic with DHA

(A) Overview of the experimental design and analysis of synergy for two and three drug combinations. (B) Heat maps of the fraction of viable cells in H460^{C} Cas9 cells co-treated with vehicle and varying doses of FSEN1 (0.05, 0.5, 5 µM) in the presence of increasing concentrations of DHA and RSL3. Data are mean values (n = 3 biological replicates). (C) 3D-dose response landscape plots illustrating the distribution and depth of synergy between the different drug combinations and doses tested in H460^{C} Cas9 cells with the corresponding average ZIP synergy scores. p = 6.13x102 and represents the significance of the difference between the estimated average synergy score over the whole dose-response matrix and 0% inhibition under the null hypothesis of non-response. (D) Multi-drug synergy bar plots of H460^{C} Cas9 cells illustrating mean ZIP synergy scores for all possible drug combinations tested. Data are mean ± SEM (n = 3 biological replicates).

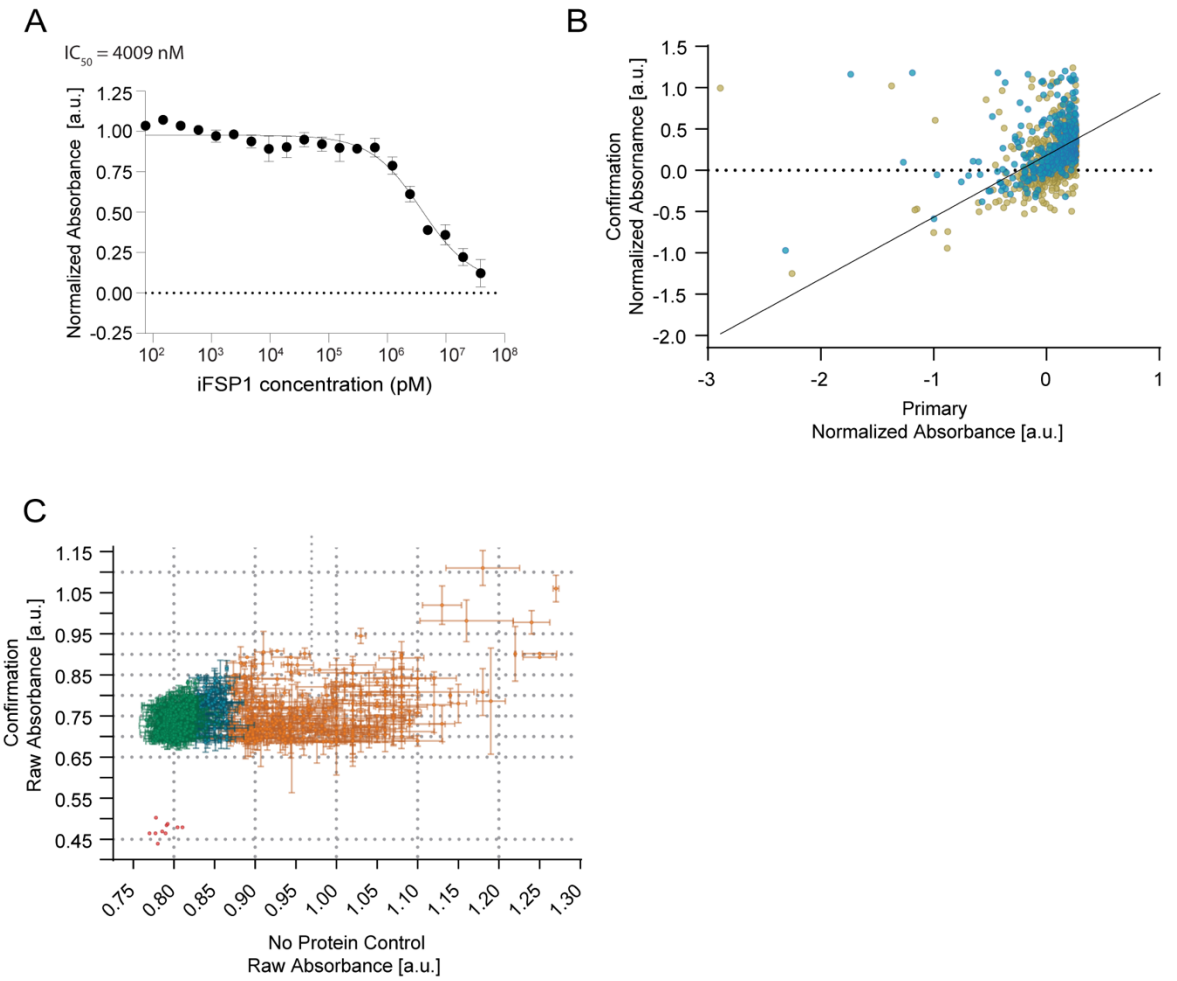

Figure 3-S1 FSP1 in vitro activity assay and screen controls (related to Figures 3-1)

(A) Dose response analyses were performed for iFSP1 using the in vitro absorbance-based assay of FSP1 activity. Data are mean ± SEM (n = 2 independent replicates). (B) 1,120 candidate inhibitors were re-tested in duplicate. The confirmation screen is plotted against the primary screen data. 743 of the 1,120 compounds were classified as confirmed “Hits”. (C) The 743 confirmed compounds (panel B) were tested in assays lacking FSP1 (i.e., no protein control). 323 compounds (green) had activity less than 5% above the DMSO average (red dots) and were selected for further validation. Potential false positives (blue) and false positives (orange) were removed from further analysis.

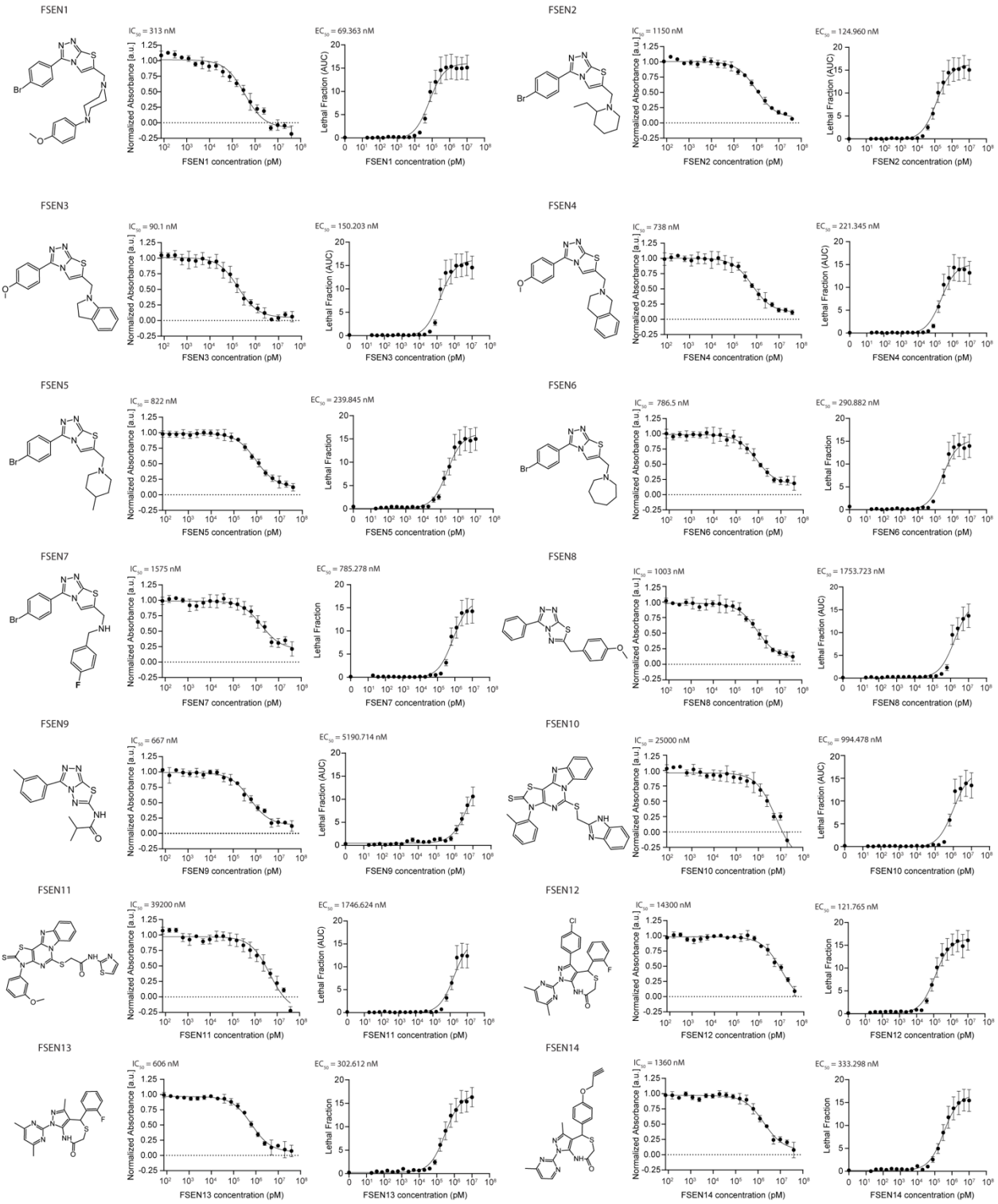

Figure 3-S2 Analysis of FSEN1-14 inhibition of FSP1 (related to Figures 3-1 and 3-2)

Dose response analyses were performed for FSEN1-14 using the in vitro absorbance-based assay of FSP1 activity and the H460^{C} GPX4^{KO} cell-based assay of ferroptosis to determine the compound's IC50 and EC50, respectively. IC50 values were calculated

from end-point assays for inhibition of FSP1 activity in vitro. Data are mean ± SEM (n = 2 independent replicates). EC50 values were calculated from lethal fraction (AUC) quantification in $H460^{C}$ $GPX4^{KO}$ cells. Data are mean ± SEM (n = 3 biological replicates). The IC50 and EC50 values calculated from these experiments are also listed in Figure 2.

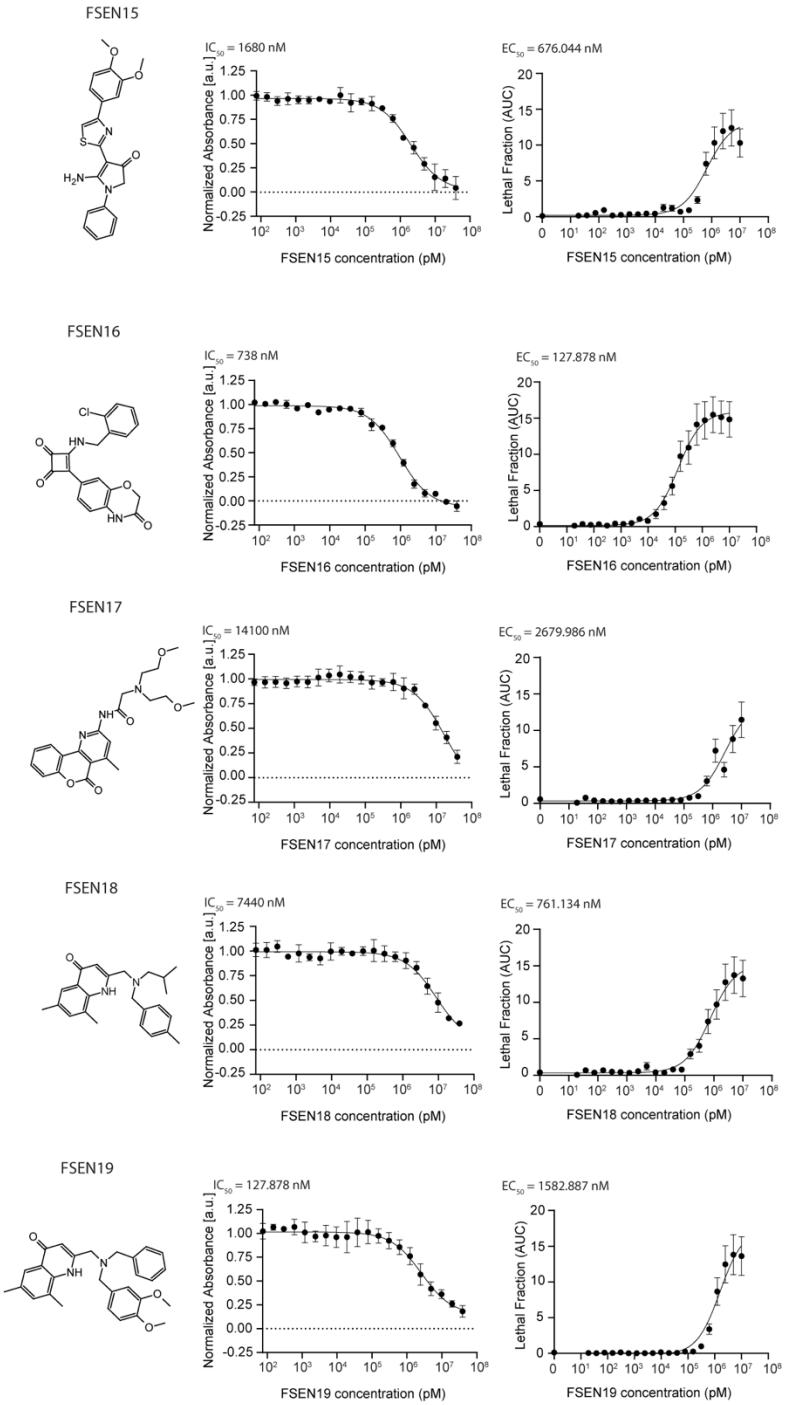

Figure 3-S3 Analysis of FSEN15-18 inhibition of FSP1 (related to Figures 3-1 and 3-2)

Dose response analyses were performed for FSEN15-19 using the in vitro absorbance-based assay of FSP1 activity and the $H460^{C}$ $GPX4^{KO}$ cell-based assay of ferroptosis to determine the compound's IC50 and EC50, respectively. IC50 values were calculated from end-point assays for inhibition of FSP1 activity in vitro. Data are mean ± SEM (n = 2 independent replicates). EC50 values were calculated from lethal fraction (AUC)

quantification in H460^{C} GPX4^{KO} cells. Data are mean ± SEM (n = 3 biological replicates). The IC50 and EC50 values calculated from these experiments are also listed in Figure 2.

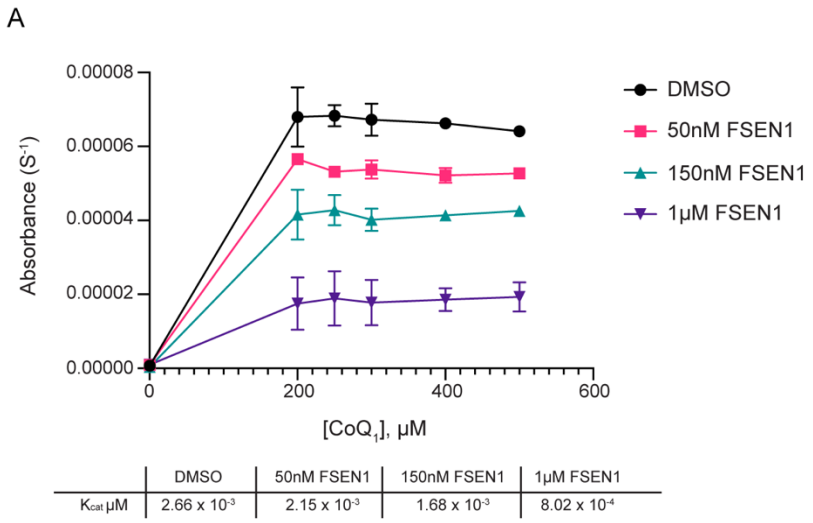

Figure 3-S4 FSEN1 FSP1 Kinetics (CoQ1) (related to Figure 3-3)

Michaelis-Menten Curve of Purified recombinant FSP1 treated with increasing concentrations of CoQ1 in the presence of vehicle or FSEN1 (0.05, 0.15, 1 µM). All NADH concentrations included 400 µM CoQ1 as co-substrate for FSP1, and NADH absorbance (355 nm) was measured as an inverse read-out of enzymatic product formation. Error bars represent SD of initial slopes, individually calculated from n = 2 independent replicates. Kcat values displayed, calculated from a non-linear regression curve fit (Vmax/FSP1 concentration [µM]).

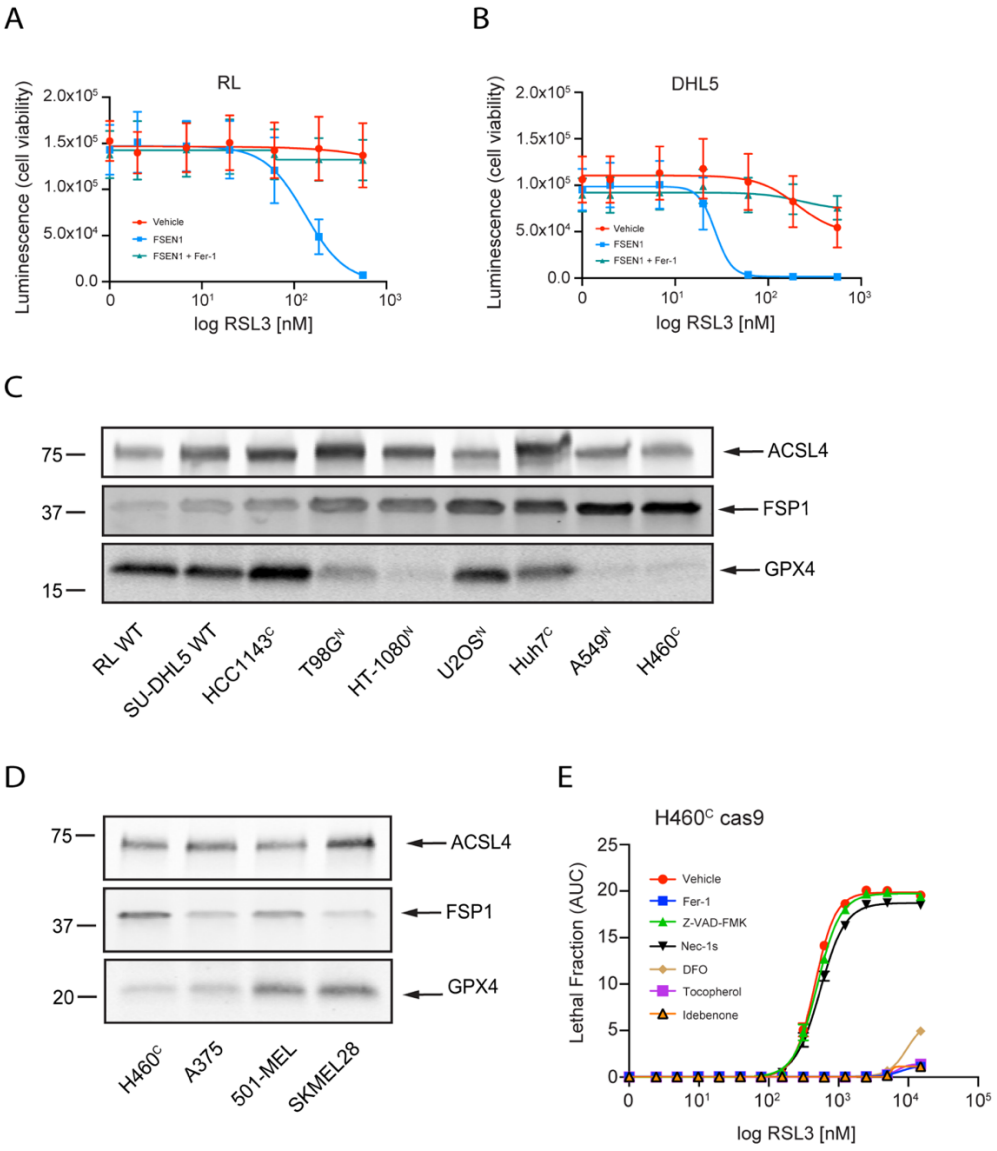

F

Cell line	Vehicle EC_{50} (nM)	+FSEN1 EC_{50} (nM)
HCC1143C	1283	300.6
T98GN	1517	272.6
HT-1080N	1401	200.6
U2OSN	3905	765.6
Huh7C	5386	493.2
A549N	5826	248
501MEL	473	21.49
SKMEL28	646.3	90.56
A375	N/A	22.45
RL	N/A	131.3
DHL5	204.8	27.03

Figure 3-S5 FSP1 inhibition triggers ferroptosis in cancer cell model (related to Figures 3-4 and 3-5)

(A,B) Dose response of RSL3 induced cell death in lymphoma cells 24 hr after co-treatment with vehicle or 1 μM FSEN1 or 1 μM FSEN1 together with 2 μM Fer-1 using the CellTiter-Glo Luminescent Cell Viability Assay. Data are mean ± SEM (n = 3 biological replicates). (C,D) Western blot analysis of cell lysates from different cancer cell lines comparing ACSL4, GPX4, and FSP1 levels. (E) Dose response of RSL3-induced cell death in $H460^{C}$ Cas9 cells co-treated with 1 μM FSEN1 together with the indicated inhibitors of ferroptosis (Fer-1 [2 μM], DFO [100 μM], idebenone [10 μM], tococopherol [10 μM]), apoptosis (Z-VAD [10 μM]), and necroptosis (Nec-1s [1 μM]). Data are mean ± SEM (n = 3 biological replicates). The Lethal Fraction (AUC) of 5 μM RSL3-induced cell death calculated from these experiments are also listed in Figure 4. (F) Corresponding EC50 values of different cancer cell lines treated with a dose response of RSL3 in the presence or absence of 1 μM FSEN1.

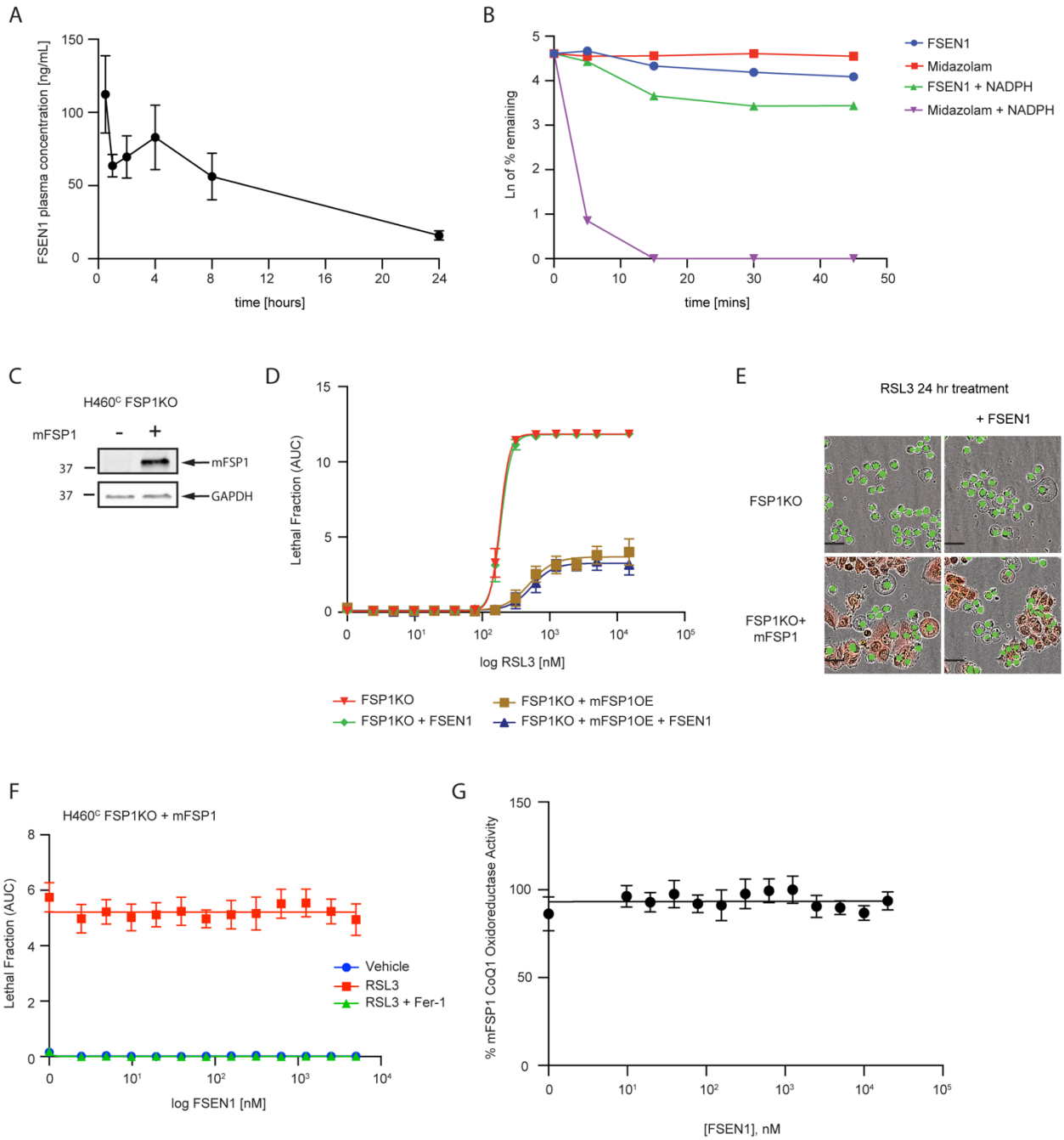

Figure 3-S6 Analysis of FSEN1 pharmacokinetics and inhibition of mouse FSP1 (related to Figures 3-3, 3-4, 3-5)

(A) Plasma concentration-time profile of FSEN1 in male BALB/c mice at 20 mg/kg (I.P.). Data are mean ± SEM (n = 5 gonadally intact adult male BALB/c mice). (B) Microsomal stability of FSEN1 in mouse liver microsomes represented as natural log of percent remaining versus incubation time. Data are median values from n = 3 independent replicates. The incubation system without NADPH is included as a negative control and midazolam is included as a positive control. (C) Western blot analysis of cell lysates from $H460^{C}$ $FSP1^{KO}$ cells and $H460^{C}$ $FSP1^{KO}$ cells stably expressing mFSP1. (D) Dose

response of RSL3-induced cell death in $H460^{C}$ $FSP1^{KO}$ and $H460^{C}$ $FSP1^{KO}$ cells stably expressing mFSP1 cells co-treated with vehicle or 1 μM FSEN1. Data are mean ± SEM (n = 3 biological replicates). (E) Representative IncuCyte images of $H460^{C}$ $FSP1^{KO}$ and $H460^{C}$ $FSP1^{KO}$ cells stably expressing mFSP1 cells co-treated treated with 1.6 μM RSL3, vehicle or 1 μM FSEN1 respectively. Scale bar represents 50 μm. Images from one of three independent experiments are shown. (F) Dose response of FSEN1 in $H460^{C}$ FSP1KO cells stably expressing mFSP1 cells co-treated with vehicle, 1 μM RSL3 or 1 μM RSL3 + 2 μM Fer-1. Data are mean ± SEM (n = 3 biological replicates). (G) Purified recombinant mFSP1 CoQ1 oxidoreductase activity measured in the presence of increasing concentrations of FSEN1. Data was normalized to the slopes calculated from DMSO and No Protein controls. Error bars represent SD of initial slopes, individually calculated from n = 3 independent replicates.

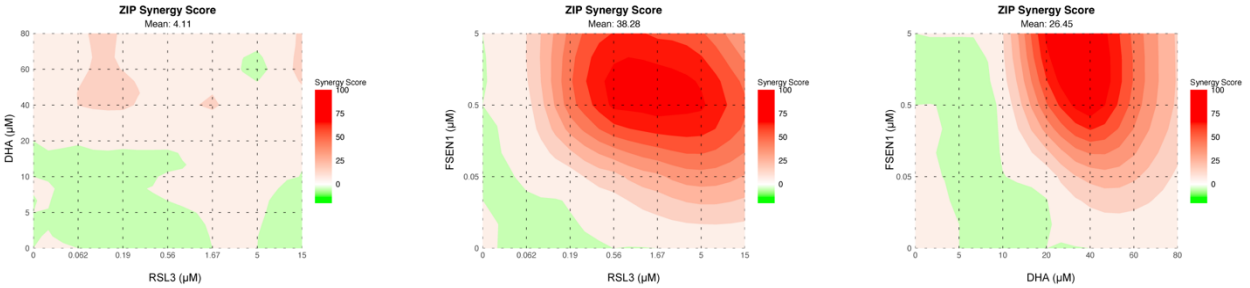

Figure 3-S7 Drug contour maps (related to Figure 3-7)

2-D-dose response contour plots illustrating the distribution of synergy between FSEN1, DHA, and RSL3 in H460^{C} Cas9 cells, based upon Figure 7C.

Chapter 4:
Concluding Remarks

4.1 Perspectives and open questions

Ferroptosis is a form regulated cell death, which depends on metabolic flux of specific cellular nutrients and metabolites. Metabolic reprogramming is a hallmark of cancer and promotes the generation of sufficient energy and biomass for cancer cell survival, proliferation, and metastasis[227]. Cancer cell metabolic reprogramming can give rise to distinct cellular metabolic profiles, such as an increase of PUFA-PLs, heightened concentrations of cellular iron pools and an imbalance in ferroptosis defense systems. This is particularly interesting because it creates a unique and targetable vulnerability to ferroptosis, presenting an exciting opportunity for innovative approaches for the development of new therapeutically relevant strategies in neoplastic diseases. Furthermore, due to the intrinsic and or acquired nature of therapeutic resistance in cancer, metabolic vulnerabilities of tumors to ferroptosis could be established by targeting underlying resistance mechanisms. The therapeutic efficacy of existing standard of care strategies that induce ferroptosis can be enhanced with co-treatment of FINs and FSENs; importantly, such combination strategies have shown excellent synergy and tolerability in preclinical models, warranting further research. Pharmacological profiles are imperative for the evaluation of ideal drug dosing regimens in patients, efficacy of treatment and any potential side effects from FINs and FSENs in normal tissues. However, a major roadblock in the field is the lack of definitive biomarkers which can be integrated into existing pathological and radiological clinical diagnostic methods. To utilize ferroptosis-inducing strategies in cancer therapies and other pathological contexts, an understanding of how metabolic flux of key metabolites can be modulated for ferroptosis induction is critical. Several obstacles must be conquered in future investigations to understand the full therapeutic potential of ferroptosis. To date, GPX4 is considered the most powerful defense mechanism against ferroptosis, and several types of therapy-resistant tumors are remarkably vulnerable to GPX4 inhibition[6,83,98]. This calls attention to the importance of GPX4 inhibitors in targeting ferroptosis vulnerability in cancer. Covalent inhibitors of GPX4, like ML210 and a chemical derivative, JKE-1674, are more selective than RSL3 and ML162 (Table 2); however, these inhibitors possess poor pharmacological properties, illustrating the limited use for clinical translation[228]. The development and optimization of selective GPX4-targeting agents with improved pharmacokinetics remain a major barrier to the use of GPX4 inhibition in cancer therapy. In this regard, uncovering the degree of currently available and in vivo-stable anticancer agents with GPX4-inhibitory activity, such as withaferin A and altretamine, should be a priority for the field and may offer an alternative to address this problem[229,230]. GPX4 is an essential gene in the mouse[105,160], and it remains to be determined whether pharmacological inhibition of GPX4 can selectively kill tumors without causing extensive toxicity in normal tissues and intolerable side effect in animal models and patients.

In addition to cancer cells, several cell types in the tumor microenvironment (TME), including immune cells that promote or suppress antitumor immunity, might also be susceptible to ferroptosis. Therefore, understanding the balance of ferroptosis vulnerabilities of cancer cells, antitumor immune cells and immunosuppressive cells remains a critical hurdle to overcome. To address these barriers, it is critically important to be cognizant of the mechanisms underlying the differential sensitivities of cancer cells

and various immune cells to ferroptosis. There remains an urgent need to develop predictive biomarkers that can accurately predict tumor responses to ferroptosis induction, especially those that can be tested directly in patients' body fluids and biopsy specimens. The development of these tools is essential for the stratification of patients with cancer and for determining treatment options with ferroptosis-inducing therapies and a more in-depth understanding of ferroptosis mechanisms will continue to provide key insights into targeting ferroptosis in cancer.

FSP1 expression strongly correlates with the resistance of cancer cell lines to ferroptosis induced by GPX4 inhibitors[89,90] and FSP1 expression is amplified in some types of cancer[144]. It was recently discovered that FSP1 is a target of the transcription factor NRF2, which is highly expressed in KEAP1 mutant lung cancers, and demonstrate resistance to GPX4 inhibition[144]. Knockout of FSP1 strongly sensitizes KEAP1 mutant lung cancer cells to ferroptosis and shRNA-depletion of FSP1 is sufficient to suppress tumor growth in a KEAP1-deficient lung cancer xenograft model[144]. Small molecule FSP1 inhibitors, such as iFSP1[90], FSEN1[47], and icFSP1[112], sensitize a variety of cancer cell lines with different tissue origins and oncogenic driver mutations to ferroptosis. These FSP1 inhibitors have shown specificity for human FSP1[47,90,231], and provide incentive to discover inhibitors of mouse FSP1 to enable in vivo studies. Several additional, structurally distinct classes of FSP1 inhibitors were recently described[47], but whether these are effective against mouse FSP1 has not been tested. A major question that remains to be addressed is the therapeutic value of FSP1 as a cancer treatment target. Genetic perturbation of FSP1[89,90,112] or chemical inhibition[47,90,144,231] has yet to show sufficient ferroptosis induction in cultured cancer cells on its own, but has demonstrated powerful synergies with other ferroptosis inducers (e.g. GPX4 inhibitors or endoperoxide-containing ferroptosis inducers)[47,89,90,144,231]. However, depletion of FSP1 alone has demonstrated the ability to suppress tumor growth in a xenograft model[144], supporting the possibility that FSP1 inhibitors could have single agent value for some cancers in vivo. It is worth noting that FSP1 KO mice are viable and do not exhibit overt tissue degeneration[225,232]. The physiological function of FSP1 is unclear, but FSP1 has been found to support glycolytic flux in adipose[225] and exercising muscle[226], thereby promoting cold- and diet-induced thermogenesis and aerobic exercise in mice. The relatively mild phenotypes in the FSP1 KO mice[225,232] suggest that FSP1 inhibition will be well tolerated in humans. This is in contrast to the more severe phenotypes following the loss of GPX4, such as embryonic lethality in GPX4 KO mice and tissue degeneration following inducible GPX4 KO[160]. FSP1 could possess therapeutic value and be targeted on its own or in combination with additional ferroptosis inducers or with existing standard of care treatments. It is possible that FSP1 inhibition will sensitize certain tissues to ferroptosis inducers. Although FSP1 KO mice demonstrate mild phenotypes, it has been shown that loss of FSP1 sensitizes mice to kidney ischemia-reperfusion injury[233]. Whether FSP1 functions in other tissues to suppress degeneration remains unclear. Studies of FSP1 and FSP1 inhibition in in vivo preclinical models of cancer and degenerative disease remain a high priority for the field.

Beyond the direct targeting of major ferroptosis governing machinery other critical questions in the field remain. Can ferroptosis be promoted through diet? Several studies

suggest that dietary factors are capable in the promotion or inhibition of ferroptosis. For example, dietary PUFAs promote ferroptosis in C. elegans[234] and in mice[235]. Dietary vitamin E can suppress the impact of damage due to loss of GPX4, and as previously mentioned, dietary selenium, and iron can influence susceptibility to ferroptosis. These findings suggest that diet of model organisms is potentially an important variable influencing susceptibility and resistance to ferroptosis and should be considered in experimentally design. It may be possible to create optimized diets for driving ferroptosis sensitivity or resistance in animals and in humans and represent an area of high interest in the field.

To summarize the key takeaways mentioned throughout this dissertation, there are five fundamental aspects of ferroptosis which are important for the field to consider going forward. First, ferroptosis is induced when specific lipids are rapidly oxidized and the cellular defense mechanisms in place are overwhelmed. This unrestrained production of lipid peroxides can be driven by ROS production; however, it is important to distinguish that ferroptosis is not synonymous with general ROS production from normal homeostatic metabolic reactions. Second, the detection for specific lipids and lipid-protein adducts that promote ferroptosis is an ongoing venture. It is important to keep in mind that oxidized lipids have varied magnitude in ferroptosis induction, whereas some lipids, such as MUFAs, extinguish ferroptosis. Third, iron is a critical micronutrient and has numerous effects beyond inducing ferroptosis, therefore iron accumulation is not synonymous with ferroptosis. The oxidation state of iron and iron complexed proteins are important for ferroptosis induction. For example, Fe^{2+} promotes ferroptosis, whereas Fe^{3+} is generally inert and stored in ferritin, however, when in the active site of lipoxygenases, Fe^{3+} provides the active form of the enzyme. Therefore, systematically mapping the redox state of iron in different biochemical contexts and how it contributes specifically to ferroptosis in each context is crucial for advancing the field. Fourth, ferroptosis is distinguishable from apoptosis, necroptosis and other forms of non-apoptotic cell death. The term “necrotic death” requires a clearer definition, and the degree to which ferroptosis can be classified as a type of necrotic death is still uncertain. Fifth, metabolism, iron regulation and ROS defenses collectively govern sensitivity and resistance to ferroptosis. Therefore, perturbing specific metabolic circuits, iron homeostatic regulation and modifying ROS levels accordingly are fundamental in modulating cellular susceptibility to ferroptosis. Ferroptosis has gained a significant amount of traction, due to the increasing amount of synergy and insight provided by the hybridization of ideas, discoveries, and experimental approaches within subdisciplines such as, metabolic circuitry, iron regulation and ROS biology.

Nevertheless, our total comprehension of ferroptosis remains fragmented – there are at least three key unanswered questions that have been proposed to drive advances in ferroptosis over the next decade. First, what is the exact execution mechanism of ferroptosis? As described above, ferroptosis is driven by the unrestrained production of oxidatively damaged PUFA-containing lipids; how, where, and when this leads to cell death is unclear. Second, uncovering each initiating mechanism and the associated context for ferroptosis will greatly enhance our comprehension of how ferroptosis fits in the broader world of biology and medicine. For example, glutamate toxicity, iron overload,

SLC7A11 suppression, GPX4 depletion, PUFA uptake and FSP1 inhibition can activate or predispose cells to ferroptosis. Suggesting a therapeutic benefit if the governing metabolic circuits are reliably identified. Third, the selective activation or inhibition in specific tissues, cells, and/or disease context is crucial for translating ferroptosis into clinically relevant therapies. For example, targeting GPX4 systematically has been shown to cause toxicities, such as kidney damage, neurodegeneration, and perturb immune functions in mouse models. Targeting FSP1 systematically could also yield unwanted side effects, however FSP1 KO mice do not exhibit a lethal phenotype, suggesting that systemic FSP1 inhibition would be tolerable. Therefore, it is important to develop a greater understanding of systemic toxicity from ferroptosis inducers and sensitizers, to identify where specific therapeutic strategies will be most effective.

Conclusions

The field of ferroptosis has enhanced our understanding of cellular mechanisms that hold sway over lipid quality control. Ferroptosis serves as an example of the devastating consequences that occur when the phospholipid quality control system fails. Many questions remain regarding the mechanism of ferroptosis and if it can be therapeutically applied in treating human cancer. Emerging data indicate the existence of multiple ferroptosis pathways that can be initiated and regulated under distinct circumstances[49]. The field has yet to completely catalog the sources and identities of the radical species that trigger ferroptosis, nor has it fully elucidated how cells detect oxidized lipids and how these detection mechanisms are utilized to suppress ferroptosis. Peroxidation of phospholipids is one example of lipid damage, and thus, ferroptosis represents the beginning of a broader field focused on lipid quality control[236–238]. Lipids are structurally diverse, and other important lipids beyond phospholipids are subject to oxidative damage (e.g., cholesterol, cardiolipin, and triacylglycerol). It is important to be cognizant of the challenges for cellular lipid quality control, including the structural diversity of lipid species, the heterogeneity in subcellular localization, the highly dynamic nature of lipid metabolism in response to different metabolic conditions and the cell type dependent contexts that influence the dynamic nature of metabolism. The field is in critical need of improved methods that can be generally integrated into existing workflows and must enhance our ability to detect and quantify damaged lipids in a temporal and spatial manner. The development of these new methods must be engineered to be applicable to all levels of experimental design with the ultimate task of being used in the clinical setting. In addition, the development of methods pertaining to the selective manipulation of specific damaged lipid species and the levels of specific damaged lipids are also of great priority. These are exciting times for the emerging field of lipid quality control. Defining additional examples of functionally important lipid damage, compartmentalized lipid quality control processes, and new methods to study lipid damage will catalyze continued progress in the field and help uncover novel strategies to combat disease.

In the era of precision oncology, the field of lipid quality control needs to be integrated into molecular tumor boards (MTBs) to optimize treatment strategies and improve clinical outcomes. Interpreting molecular-profiling data and matching patients with appropriate available molecularly targeted therapies, which can include investigational drugs, will greatly inform preclinical study directions, and could pave the way for novel therapeutic strategies. There are several opportunities where the selective control of ferroptosis can be optimized and include drug delivery, biodistribution, pharmacokinetics, dietary regimes, and selection of targets in specific metabolic contexts. Ferroptosis inducers and sensitizers are being explored for their ability to eliminate specific cell population, such as specific tumor types, and are being explored in the context of drug synergy. Further pre-clinical research is needed to validate which drug synergies are most effective in specific preclinical models. FSP1 inhibitors sensitize to ferroptosis when GPX4 is also targeted in numerous cancer cell lines. This group of molecules represent a unique opportunity to explore combinatorial strategies of ferroptosis induction. Like the FINs, it is possible that FSP1 inhibitors can act as radio and immunotherapy sensitizers enhancing the efficacy of existing therapeutic strategies for abolishing cancer. Additionally targeted protein

degradation technologies, such as PROTACs [239,240], should be further explored in the field of ferroptosis and have been mostly unexplored. This too may represent a unique opportunity in generating highly specific and effective therapeutic strategies of clinical relevance. Uncovering these mechanisms and dosing regimens will require the field to adopt a new school of thought, and answering these questions is projected to introduce critically important insights not only into ferroptosis, but also into the diverse areas of biology where it is connected.

The work in this dissertation highlights our current understanding of non-apoptotic cell death modalities and advances the field of ferroptosis. Chapter 1 provides a brief overview of the field of cell death and ferroptosis. Chapter 2 describes the genetic strategy employed to discover ferroptosis resistance factors in an osteosarcoma cell line and provides mechanistic details on the role of this gene in protecting against ferroptosis. The role of this gene is further expanded to lung cancer cell lines and investigated as a target of therapeutic relevance in preclinical mouse xenografts. Ultimately leading to a model where FSP1 functions as a plasma membrane targeted oxidoreductase catalyzing the regeneration of the lipophilic antioxidant Co-enzyme Q_{10} to quench radicalized lipid and phospholipid species in the plasma membrane, thereby mitigating ferroptotic cell death. Chapter 3 describes a small molecule drug screen strategy employed to identify novel and structurally distinct small molecule inhibitors of FSP1. Further expanded by the biochemical and cellular characterization of the lead inhibitor identified, FSEN1. Synergistic relationships between FSEN1, RSL3 and DHA are identified, characterized, and quantified in a dose response matrix and analyzed using a synergy algorithm. Chapter 4 discusses important questions and perspectives on the future of ferroptosis and the role it may play in disease and therapeutic relevance. Collectively this work demonstrates the multiple platforms used to identify ferroptosis resistance factors and efforts to uncover therapeutic relevance for treatment of aggressive forms of cancer.

References

1. Dixon SJ, Lemberg KM, Lamprecht MR, et al. Ferroptosis: an iron-dependent form of nonapoptotic cell death. *Cell*. 2012;149(5):1060-1072. doi:10.1016/j.cell.2012.03.042

2. Stockwell BR, Friedmann Angeli JP, Bayir H, et al. Ferroptosis: A regulated cell death nexus linking metabolism, redox biology, and disease. *Cell*. 2017;171(2):273-285. doi:10.1016/j.cell.2017.09.021

3. Yang WS, SriRamaratnam R, Welsch ME, et al. Regulation of ferroptotic cancer cell death by GPX4. *Cell*. 2014;156(1-2):317-331. doi:10.1016/j.cell.2013.12.010

4. Ingold I, Berndt C, Schmitt S, et al. Selenium Utilization by GPX4 Is Required to Prevent Hydroperoxide-Induced Ferroptosis. *Cell*. 2018;172(3):409-422.e21. doi:10.1016/j.cell.2017.11.048

5. Dixon SJ, Stockwell BR. The hallmarks of ferroptosis. *Annu Rev Cancer Biol*. 2019;3(1):35-54. doi:10.1146/annurev-cancerbio-030518-055844

6. Zou Y, Palte MJ, Deik AA, et al. A GPX4-dependent cancer cell state underlies the clear-cell morphology and confers sensitivity to ferroptosis. *Nat Commun*. 2019;10(1):1617. doi:10.1038/s41467-019-09277-9

7. Green DR, Galluzzi L, Kroemer G. Cell biology. Metabolic control of cell death. *Science*. 2014;345(6203):1250256. doi:10.1126/science.1250256

8. Mason EF, Rathmell JC. Cell metabolism: an essential link between cell growth and apoptosis. *Biochim Biophys Acta*. 2011;1813(4):645-654. doi:10.1016/j.bbamcr.2010.08.011

9. Hadian K, Stockwell BR. The therapeutic potential of targeting regulated non-apoptotic cell death. *Nat Rev Drug Discov*. 2023;22(9):723-742. doi:10.1038/s41573-023-00749-8

10. Kerr JF, Wyllie AH, Currie AR. Apoptosis: a basic biological phenomenon with wide-ranging implications in tissue kinetics. *Br J Cancer*. 1972;26(4):239-257. doi:10.1038/bjc.1972.33

11. Tait SWG, Ichim G, Green DR. Die another way--non-apoptotic mechanisms of cell death. *J Cell Sci*. 2014;127(Pt 10):2135-2144. doi:10.1242/jcs.093575

12. Vanden Berghe T, Linkermann A, Jouan-Lanhouet S, Walczak H, Vandenabeele P. Regulated necrosis: the expanding network of non-apoptotic cell death pathways. *Nat Rev Mol Cell Biol*. 2014;15(2):135-147. doi:10.1038/nrm3737

13. Tang D, Kang R, Berghe TV, Vandenabeele P, Kroemer G. The molecular machinery of regulated cell death. *Cell Res*. 2019;29(5):347-364. doi:10.1038/s41422-019-0164-5

14. Cao JY, Dixon SJ. Mechanisms of ferroptosis. *Cell Mol Life Sci*. 2016;73(11-12):2195-2209. doi:10.1007/s00018-016-2194-1

15. Wyllie AH, Kerr JF, Currie AR. Cell death: the significance of apoptosis. *Int Rev Cytol*. 1980;68:251-306. doi:10.1016/S0074-7696(08)62312-8

16. Fadok VA, Voelker DR, Campbell PA, Cohen JJ, Bratton DL, Henson PM. Exposure of phosphatidylserine on the surface of apoptotic lymphocytes triggers specific recognition and removal by macrophages. *J Immunol*. 1992;148(7):2207-2216.

17. Elmore S. Apoptosis: a review of programmed cell death. *Toxicol Pathol*. 2007;35(4):495-516. doi:10.1080/01926230701320337

18. Locksley RM, Killeen N, Lenardo MJ. The TNF and TNF receptor superfamilies: integrating mammalian biology. *Cell*. 2001;104(4):487-501. doi:10.1016/s0092-8674(01)00237-9

19. Ashkenazi A, Dixit VM. Death receptors: signaling and modulation. *Science*. 1998;281(5381):1305-1308. doi:10.1126/science.281.5381.1305

20. Chicheportiche Y, Bourdon PR, Xu H, et al. TWEAK, a new secreted ligand in the tumor necrosis factor family that weakly induces apoptosis. *J Biol Chem*. 1997;272(51):32401-32410. doi:10.1074/jbc.272.51.32401

21. Peter ME, Krammer PH. Mechanisms of CD95 (APO-1/Fas)-mediated apoptosis. *Curr Opin Immunol*. 1998;10(5):545-551. doi:10.1016/s0952-7915(98)80222-7

22. Suliman A, Lam A, Datta R, Srivastava RK. Intracellular mechanisms of TRAIL: apoptosis through mitochondrial-dependent and -independent pathways. *Oncogene*. 2001;20(17):2122-2133. doi:10.1038/sj.onc.1204282

23. Rubio-Moscardo F, Blesa D, Mestre C, et al. Characterization of 8p21.3 chromosomal deletions in B-cell lymphoma: TRAIL-R1 and TRAIL-R2 as candidate dosage-dependent tumor suppressor genes. *Blood*. 2005;106(9):3214-3222. doi:10.1182/blood-2005-05-2013

24. Saelens X, Festjens N, Vande Walle L, van Gurp M, van Loo G, Vandenabeele P. Toxic proteins released from mitochondria in cell death. *Oncogene*. 2004;23(16):2861-2874. doi:10.1038/sj.onc.1207523

25. Cai J, Yang J, Jones DP. Mitochondrial control of apoptosis: the role of cytochrome c. *Biochim Biophys Acta*. 1998;1366(1-2):139-149. doi:10.1016/s0005-2728(98)00109-1

26. Du C, Fang M, Li Y, Li L, Wang X. Smac, a mitochondrial protein that promotes cytochrome c-dependent caspase activation by eliminating IAP inhibition. *Cell*. 2000;102(1):33-42. doi:10.1016/s0092-8674(00)00008-8

27. van Loo G, Saelens X, van Gurp M, MacFarlane M, Martin SJ, Vandenabeele P. The role of mitochondrial factors in apoptosis: a Russian roulette with more than one bullet. *Cell Death Differ*. 2002;9(10):1031-1042. doi:10.1038/sj.cdd.4401088

28. Garrido C, Galluzzi L, Brunet M, Puig PE, Didelot C, Kroemer G. Mechanisms of cytochrome c release from mitochondria. *Cell Death Differ*. 2006;13(9):1423-1433. doi:10.1038/sj.cdd.4401950

29. Chinnaiyan AM. The apoptosome: heart and soul of the cell death machine. *Neoplasia*. 1999;1(1):5-15. doi:10.1038/sj.neo.7900003

30. Hill MM, Adrain C, Duriez PJ, Creagh EM, Martin SJ. Analysis of the composition, assembly kinetics and activity of native Apaf-1 apoptosomes. *EMBO J*. 2004;23(10):2134-2145. doi:10.1038/sj.emboj.7600210

31. Slee EA, Adrain C, Martin SJ. Executioner caspase-3, -6, and -7 perform distinct, non-redundant roles during the demolition phase of apoptosis. *J Biol Chem*. 2001;276(10):7320-7326. doi:10.1074/jbc.M008363200

32. Fink SL, Cookson BT. Apoptosis, pyroptosis, and necrosis: mechanistic description of dead and dying eukaryotic cells. *Infect Immun*. 2005;73(4):1907-1916. doi:10.1128/IAI.73.4.1907-1916.2005

33. Shan B, Pan H, Najafov A, Yuan J. Necroptosis in development and diseases. *Genes Dev*. 2018;32(5-6):327-340. doi:10.1101/gad.312561.118

34. Dhuriya YK, Sharma D. Necroptosis: a regulated inflammatory mode of cell death. *J Neuroinflammation*. 2018;15(1):199. doi:10.1186/s12974-018-1235-0

35. Holler N, Zaru R, Micheau O, et al. Fas triggers an alternative, caspase-8-independent cell death pathway using the kinase RIP as effector molecule. *Nat Immunol*. 2000;1(6):489-495. doi:10.1038/82732

36. Degterev A, Huang Z, Boyce M, et al. Chemical inhibitor of nonapoptotic cell death with therapeutic potential for ischemic brain injury. *Nat Chem Biol*. 2005;1(2):112-119. doi:10.1038/nchembio711

37. Galluzzi L, Kepp O, Chan FK-M, Kroemer G. Necroptosis: mechanisms and relevance to disease. *Annu Rev Pathol*. 2017;12:103-130. doi:10.1146/annurev-pathol-052016-100247

38. Kaiser WJ, Sridharan H, Huang C, et al. Toll-like receptor 3-mediated necrosis via TRIF, RIP3, and MLKL. *J Biol Chem*. 2013;288(43):31268-31279. doi:10.1074/jbc.M113.462341

39. Kaczmarek A, Vandenabeele P, Krysko DV. Necroptosis: the release of damage-associated molecular patterns and its physiological relevance. *Immunity*. 2013;38(2):209-223. doi:10.1016/j.immuni.2013.02.003

40. Sethi A, Horne CR, Fitzgibbon C, et al. Membrane permeabilization is mediated by distinct epitopes in mouse and human orthologs of the necroptosis effector, MLKL. *Cell Death Differ*. 2022;29(9):1804-1815. doi:10.1038/s41418-022-00965-6

41. Galluzzi L, Vitale I, Aaronson SA, et al. Molecular mechanisms of cell death: recommendations of the Nomenclature Committee on Cell Death 2018. *Cell Death Differ*. 2018;25(3):486-541. doi:10.1038/s41418-017-0012-4

42. Dixon SJ, Stockwell BR. The role of iron and reactive oxygen species in cell death. *Nat Chem Biol*. 2014;10(1):9-17. doi:10.1038/nchembio.1416

43. Skouta R, Dixon SJ, Wang J, et al. Ferrostatins inhibit oxidative lipid damage and cell death in diverse disease models. *J Am Chem Soc*. 2014;136(12):4551-4556. doi:10.1021/ja411006a

44. Dixon SJ, Patel DN, Welsch M, et al. Pharmacological inhibition of cystine-glutamate exchange induces endoplasmic reticulum stress and ferroptosis. *eLife*. 2014;3:e02523. doi:10.7554/eLife.02523

45. Lemberg K. Ferroptosis: A Novel Form of Cancer Cell Death Induced by the Small Molecule Erastin. *Columbia University*. 2011. doi:10.7916/d8n87hz3

46. Viswanathan V. Cellular features predicting susceptibility to ferroptosis: insights from cancer cell-line profiling. *Columbia University*. 2015. doi:10.7916/d8h9940v

47. Hendricks JM, Doubravsky CE, Wehri E, et al. Identification of structurally diverse FSP1 inhibitors that sensitize cancer cells to ferroptosis. *Cell Chem Biol*. 2023;30(9):1090-1103.e7. doi:10.1016/j.chembiol.2023.04.007

48. Yagoda N, von Rechenberg M, Zaganjor E, et al. RAS-RAF-MEK-dependent oxidative cell death involving voltage-dependent anion channels. *Nature*. 2007;447(7146):864-868. doi:10.1038/nature05859

49. Dixon SJ, Pratt DA. Ferroptosis: A flexible constellation of related biochemical mechanisms. *Mol Cell*. 2023;83(7):1030-1042. doi:10.1016/j.molcel.2023.03.005

50. Raimundo N, Song L, Shutt TE, et al. Mitochondrial stress engages E2F1 apoptotic signaling to cause deafness. *Cell*. 2012;148(4):716-726. doi:10.1016/j.cell.2011.12.027

51. Hamacher-Brady A, Stein HA, Turschner S, et al. Artesunate activates mitochondrial apoptosis in breast cancer cells via iron-catalyzed lysosomal reactive oxygen species production. *J Biol Chem*. 2011;286(8):6587-6601. doi:10.1074/jbc.M110.210047

52. Kim MJ, Yun GJ, Kim SE. Metabolic regulation of ferroptosis in cancer. *Biology (Basel)*. 2021;10(2). doi:10.3390/biology10020083

53. Wallace DF. The regulation of iron absorption and homeostasis. *Clin Biochem Rev*. 2016;37(2):51-62.

54. Takemoto K, Kawai H, Kuwahara T, Nishina M, Adachi S. Metal concentrations in human lung tissue, with special reference to age, sex, cause of death, emphysema and contamination of lung tissue. *Int Arch Occup Environ Health*. 1991;62(8):579-586. doi:10.1007/BF00381111

55. Díez M, Arroyo M, Cerdàn FJ, Muñoz M, Martin MA, Balibrea JL. Serum and tissue trace metal levels in lung cancer. *Oncology*. 1989;46(4):230-234. doi:10.1159/000226722

56. Sirlin CB, Reeder SB. Magnetic resonance imaging quantification of liver iron. *Magn Reson Imaging Clin N Am*. 2010;18(3):359-381, ix. doi:10.1016/j.mric.2010.08.014

57. van Eijk HG, Wiltink WF, Goossens JP, Tio TH. Proceedings: Measurement of the diurnal and nocturnal variations of the serum iron in normal human subjects, of the iron content in human liver specimens and in human skin biopsies. *Hoppe-Seyler's Z Physiol Chem*. 1974;355(10):1190.

58. Carpenter J-P, He T, Kirk P, et al. On T2* magnetic resonance and cardiac iron. *Circulation*. 2011;123(14):1519-1528. doi:10.1161/CIRCULATIONAHA.110.007641

59. Kell DB. Iron behaving badly: inappropriate iron chelation as a major contributor to the aetiology of vascular and other progressive inflammatory and degenerative diseases. *BMC Med Genomics*. 2009;2:2. doi:10.1186/1755-8794-2-2

60. Munro AW, McLean KJ, Grant JL, Makris TM. Structure and function of the cytochrome P450 peroxygenase enzymes. *Biochem Soc Trans*. 2018;46(1):183-196. doi:10.1042/BST20170218

61. Fang Y, Chen X, Tan Q, Zhou H, Xu J, Gu Q. Inhibiting Ferroptosis through Disrupting the NCOA4-FTH1 Interaction: A New Mechanism of Action. *ACS Cent Sci*. 2021;7(6):980-989. doi:10.1021/acscentsci.0c01592

62. Schneider M, Wortmann M, Mandal PK, et al. Absence of glutathione peroxidase 4 affects tumor angiogenesis through increased 12/15-lipoxygenase activity. *Neoplasia*. 2010;12(3):254-263. doi:10.1593/neo.91782

63. Seiler A, Schneider M, Förster H, et al. Glutathione peroxidase 4 senses and translates oxidative stress into 12/15-lipoxygenase dependent- and AIF-mediated cell death. *Cell Metab*. 2008;8(3):237-248. doi:10.1016/j.cmet.2008.07.005

64. Wagner BA, Buettner GR, Burns CP. Free radical-mediated lipid peroxidation in cells: oxidizability is a function of cell lipid bis-allylic hydrogen content. *Biochemistry*. 1994;33(15):4449-4453. doi:10.1021/bi00181a003

65. Dixon SJ, Winter GE, Musavi LS, et al. Human haploid cell genetics reveals roles for lipid metabolism genes in nonapoptotic cell death. *ACS Chem Biol*. 2015;10(7):1604-1609. doi:10.1021/acschembio.5b00245

66. Doll S, Proneth B, Tyurina YY, et al. ACSL4 dictates ferroptosis sensitivity by shaping cellular lipid composition. *Nat Chem Biol*. 2017;13(1):91-98. doi:10.1038/nchembio.2239

67. Kagan VE, Mao G, Qu F, et al. Oxidized arachidonic and adrenic PEs navigate cells to ferroptosis. *Nat Chem Biol*. 2017;13(1):81-90. doi:10.1038/nchembio.2238

68. Savaskan NE, Ufer C, Kühn H, Borchert A. Molecular biology of glutathione peroxidase 4: from genomic structure to developmental expression and neural function. *Biol Chem*. 2007;388(10):1007-1017. doi:10.1515/BC.2007.126

69. Buettner GR. The pecking order of free radicals and antioxidants: lipid peroxidation, alpha-tocopherol, and ascorbate. *Arch Biochem Biophys*. 1993;300(2):535-543. doi:10.1006/abbi.1993.1074

70. Conrad M, Pratt DA. The chemical basis of ferroptosis. *Nat Chem Biol*. 2019;15(12):1137-1147. doi:10.1038/s41589-019-0408-1

71. Dalleau S, Baradat M, Guéraud F, Huc L. Cell death and diseases related to oxidative stress: 4-hydroxynonenal (HNE) in the balance. *Cell Death Differ*. 2013;20(12):1615-1630. doi:10.1038/cdd.2013.138

72. Barrera G. Oxidative stress and lipid peroxidation products in cancer progression and therapy. *ISRN Oncol*. 2012;2012:137289. doi:10.5402/2012/137289

73. Shimada K, Skouta R, Kaplan A, et al. Global survey of cell death mechanisms reveals metabolic regulation of ferroptosis. *Nat Chem Biol*. 2016;12(7):497-503. doi:10.1038/nchembio.2079

74. Matsunaga T, Shinoda Y, Inoue Y, Endo S, El-Kabbani O, Hara A. Protective effect of rat aldo-keto reductase (AKR1C15) on endothelial cell damage elicited by 4-hydroxy-2-nonenal. *Chem Biol Interact*. 2011;191(1-3):364-370. doi:10.1016/j.cbi.2010.12.018

75. Sun X, Ou Z, Chen R, et al. Activation of the p62-Keap1-NRF2 pathway protects against ferroptosis in hepatocellular carcinoma cells. *Hepatology*. 2016;63(1):173-184. doi:10.1002/hep.28251

76. Kuang F, Liu J, Xie Y, Tang D, Kang R. MGST1 is a redox-sensitive repressor of ferroptosis in pancreatic cancer cells. *Cell Chem Biol*. 2021;28(6):765-775.e5. doi:10.1016/j.chembiol.2021.01.006

77. Sviderskiy VO, Terzi EM, Possemato R. Iron–sulfur cluster metabolism impacts iron homeostasis, ferroptosis sensitivity, and human disease. In: Tang D, ed. *Ferroptosis in Health and Disease*. Springer International Publishing; 2019:215-237. doi:10.1007/978-3-030-26780-3_12

78. Hayano M, Yang WS, Corn CK, Pagano NC, Stockwell BR. Loss of cysteinyl-tRNA synthetase (CARS) induces the transsulfuration pathway and inhibits ferroptosis induced by cystine deprivation. *Cell Death Differ*. 2016;23(2):270-278. doi:10.1038/cdd.2015.93

79. Wallis KF, Morehead LC, Bird JT, Byrum SD, Miousse IR. Differences in cell death in methionine versus cysteine depletion. *Environ Mol Mutagen*. 2021;62(3):216-226. doi:10.1002/em.22428

80. Zhang Y, Swanda RV, Nie L, et al. mTORC1 couples cyst(e)ine availability with GPX4 protein synthesis and ferroptosis regulation. *Nat Commun*. 2021;12(1):1589. doi:10.1038/s41467-021-21841-w

81. Yi J, Zhu J, Wu J, Thompson CB, Jiang X. Oncogenic activation of PI3K-AKT-mTOR signaling suppresses ferroptosis via SREBP-mediated lipogenesis. *Proc Natl Acad Sci USA*. 2020;117(49):31189-31197. doi:10.1073/pnas.2017152117

82. Magtanong L, Ko P-J, To M, et al. Exogenous Monounsaturated Fatty Acids Promote a Ferroptosis-Resistant Cell State. *Cell Chem Biol*. 2019;26(3):420-432.e9. doi:10.1016/j.chembiol.2018.11.016

83. Zou Y, Henry WS, Ricq EL, et al. Plasticity of ether lipids promotes ferroptosis susceptibility and evasion. *Nature*. 2020;585(7826):603-608. doi:10.1038/s41586-020-2732-8

84. Chen D, Chu B, Yang X, et al. iPLA2β-mediated lipid detoxification controls p53-driven ferroptosis independent of GPX4. *Nat Commun*. 2021;12(1):3644. doi:10.1038/s41467-021-23902-6

85. Sun W-Y, Tyurin VA, Mikulska-Ruminska K, et al. Phospholipase iPLA2β averts ferroptosis by eliminating a redox lipid death signal. *Nat Chem Biol*. 2021;17(4):465-476. doi:10.1038/s41589-020-00734-x

86. Tan SK, Mahmud I, Fontanesi F, et al. Obesity-Dependent Adipokine Chemerin Suppresses Fatty Acid Oxidation to Confer Ferroptosis Resistance. *Cancer Discov*. 2021;11(8):2072-2093. doi:10.1158/2159-8290.CD-20-1453

87. Polewski MD, Reveron-Thornton RF, Cherryholmes GA, Marinov GK, Cassady K, Aboody KS. Increased Expression of System xc- in Glioblastoma Confers an Altered Metabolic State and Temozolomide Resistance. *Mol Cancer Res*. 2016;14(12):1229-1242. doi:10.1158/1541-7786.MCR-16-0028

88. Chen H, Peng F, Xu J, Wang G, Zhao Y. Increased expression of GPX4 promotes the tumorigenesis of thyroid cancer by inhibiting ferroptosis and predicts poor clinical outcomes. *Aging (Albany NY)*. 2023;15(1):230-245. doi:10.18632/aging.204473

89. Bersuker K, Hendricks JM, Li Z, et al. The CoQ oxidoreductase FSP1 acts parallel to GPX4 to inhibit ferroptosis. *Nature*. 2019;575(7784):688-692. doi:10.1038/s41586-019-1705-2

90. Doll S, Freitas FP, Shah R, et al. FSP1 is a glutathione-independent ferroptosis suppressor. *Nature*. 2019;575(7784):693-698. doi:10.1038/s41586-019-1707-0

91. Forman HJ, Zhang H, Rinna A. Glutathione: overview of its protective roles, measurement, and biosynthesis. *Mol Aspects Med*. 2009;30(1-2):1-12. doi:10.1016/j.mam.2008.08.006

92. Aquilano K, Baldelli S, Ciriolo MR. Glutathione: new roles in redox signaling for an old antioxidant. *Front Pharmacol*. 2014;5:196. doi:10.3389/fphar.2014.00196

93. Koppula P, Zhang Y, Zhuang L, Gan B. Amino acid transporter SLC7A11/xCT at the crossroads of regulating redox homeostasis and nutrient dependency of cancer. *Cancer Commun (Lond)*. 2018;38(1):12. doi:10.1186/s40880-018-0288-x

94. Liu X, Olszewski K, Zhang Y, et al. Cystine transporter regulation of pentose phosphate pathway dependency and disulfide stress exposes a targetable

metabolic vulnerability in cancer. *Nat Cell Biol*. 2020;22(4):476-486. doi:10.1038/s41556-020-0496-x

95. Koppula P, Zhuang L, Gan B. Cystine transporter SLC7A11/xCT in cancer: ferroptosis, nutrient dependency, and cancer therapy. *Protein Cell*. 2021;12(8):599-620. doi:10.1007/s13238-020-00789-5

96. Jiang L, Kon N, Li T, et al. Ferroptosis as a p53-mediated activity during tumour suppression. *Nature*. 2015;520(7545):57-62. doi:10.1038/nature14344

97. Zhang Y, Shi J, Liu X, et al. BAP1 links metabolic regulation of ferroptosis to tumour suppression. *Nat Cell Biol*. 2018;20(10):1181-1192. doi:10.1038/s41556-018-0178-0

98. Viswanathan VS, Ryan MJ, Dhruv HD, et al. Dependency of a therapy-resistant state of cancer cells on a lipid peroxidase pathway. *Nature*. 2017;547(7664):453-457. doi:10.1038/nature23007

99. Brigelius-Flohé R, Maiorino M. Glutathione peroxidases. *Biochim Biophys Acta*. 2013;1830(5):3289-3303. doi:10.1016/j.bbagen.2012.11.020

100. Brigelius-Flohé R, Flohé L. Regulatory phenomena in the glutathione peroxidase superfamily. *Antioxid Redox Signal*. 2020;33(7):498-516. doi:10.1089/ars.2019.7905

101. Pushpa-Rekha TR, Burdsall AL, Oleksa LM, Chisolm GM, Driscoll DM. Rat phospholipid-hydroperoxide glutathione peroxidase. cDNA cloning and identification of multiple transcription and translation start sites. *J Biol Chem*. 1995;270(45):26993-26999. doi:10.1074/jbc.270.45.26993

102. Pfeifer H, Conrad M, Roethlein D, et al. Identification of a specific sperm nuclei selenoenzyme necessary for protamine thiol cross-linking during sperm maturation. *FASEB J*. 2001;15(7):1236-1238. doi:10.1096/fj.00-0655fje

103. Seibt TM, Proneth B, Conrad M. Role of GPX4 in ferroptosis and its pharmacological implication. *Free Radic Biol Med*. 2019;133:144-152. doi:10.1016/j.freeradbiomed.2018.09.014

104. Ursini F, Maiorino M, Valente M, Ferri L, Gregolin C. Purification from pig liver of a protein which protects liposomes and biomembranes from peroxidative degradation and exhibits glutathione peroxidase activity on phosphatidylcholine hydroperoxides. *Biochim Biophys Acta*. 1982;710(2):197-211. doi:10.1016/0005-2760(82)90150-3

105. Yant LJ, Ran Q, Rao L, et al. The selenoprotein GPX4 is essential for mouse development and protects from radiation and oxidative damage insults. *Free Radic Biol Med*. 2003;34(4):496-502. doi:10.1016/s0891-5849(02)01360-6

106. Conrad M, Moreno SG, Sinowatz F, et al. The nuclear form of phospholipid hydroperoxide glutathione peroxidase is a protein thiol peroxidase contributing to sperm chromatin stability. *Mol Cell Biol*. 2005;25(17):7637-7644. doi:10.1128/MCB.25.17.7637-7644.2005

107. Liang H, Yoo S-E, Na R, Walter CA, Richardson A, Ran Q. Short form glutathione peroxidase 4 is the essential isoform required for survival and somatic mitochondrial functions. *J Biol Chem*. 2009;284(45):30836-30844. doi:10.1074/jbc.M109.032839

108. Schneider M, Förster H, Boersma A, et al. Mitochondrial glutathione peroxidase 4 disruption causes male infertility. *FASEB J*. 2009;23(9):3233-3242. doi:10.1096/fj.09-132795

109. Imai H, Hakkaku N, Iwamoto R, et al. Depletion of selenoprotein GPx4 in spermatocytes causes male infertility in mice. *J Biol Chem*. 2009;284(47):32522-32532. doi:10.1074/jbc.M109.016139

110. Li Z, Ferguson L, Deol KK, et al. Ribosome stalling during selenoprotein translation exposes a ferroptosis vulnerability. *Nat Chem Biol*. 2022;18(7):751-761. doi:10.1038/s41589-022-01033-3

111. Crane FL. Discovery of ubiquinone (coenzyme Q) and an overview of function. *Mitochondrion*. 2007;7 Suppl:S2-7. doi:10.1016/j.mito.2007.02.011

112. Mishima E, Ito J, Wu Z, et al. A non-canonical vitamin K cycle is a potent ferroptosis suppressor. *Nature*. 2022;608(7924):778-783. doi:10.1038/s41586-022-05022-3

113. Jin D-Y, Chen X, Liu Y, et al. A genome-wide CRISPR-Cas9 knockout screen identifies FSP1 as the warfarin-resistant vitamin K reductase. *Nat Commun*. 2023;14(1):828. doi:10.1038/s41467-023-36446-8

114. Stefely JA, Pagliarini DJ. Biochemistry of mitochondrial coenzyme Q biosynthesis. *Trends Biochem Sci*. 2017;42(10):824-843. doi:10.1016/j.tibs.2017.06.008

115. Kalén A, Norling B, Appelkvist EL, Dallner G. Ubiquinone biosynthesis by the microsomal fraction from rat liver. *Biochim Biophys Acta*. 1987;926(1):70-78. doi:10.1016/0304-4165(87)90183-8

116. Turunen M, Olsson J, Dallner G. Metabolism and function of coenzyme Q. *Biochim Biophys Acta*. 2004;1660(1-2):171-199. doi:10.1016/j.bbamem.2003.11.012

117. Takahashi T, Okamoto T, Mori K, Sayo H, Kishi T. Distribution of ubiquinone and ubiquinol homologues in rat tissues and subcellular fractions. *Lipids*. 1993;28(9):803-809. doi:10.1007/BF02536234

118. Morré DJ, Morré DM. Non-mitochondrial coenzyme Q. *Biofactors*. 2011;37(5):355-360. doi:10.1002/biof.156

119. Deshwal S, Onishi M, Tatsuta T, et al. Mitochondria regulate intracellular coenzyme Q transport and ferroptotic resistance via STARD7. *Nat Cell Biol*. 2023;25(2):246-257. doi:10.1038/s41556-022-01071-y

120. Mugoni V, Postel R, Catanzaro V, et al. Ubiad1 is an antioxidant enzyme that regulates eNOS activity by CoQ10 synthesis. *Cell*. 2013;152(3):504-518. doi:10.1016/j.cell.2013.01.013

121. Kraft VAN, Bezjian CT, Pfeiffer S, et al. GTP Cyclohydrolase 1/Tetrahydrobiopterin Counteract Ferroptosis through Lipid Remodeling. *ACS Cent Sci*. 2020;6(1):41-53. doi:10.1021/acscentsci.9b01063

122. Soula M, Weber RA, Zilka O, et al. Metabolic determinants of cancer cell sensitivity to canonical ferroptosis inducers. *Nat Chem Biol*. 2020;16(12):1351-1360. doi:10.1038/s41589-020-0613-y

123. Thöny B, Auerbach G, Blau N. Tetrahydrobiopterin biosynthesis, regeneration and functions. *Biochem J*. 2000;347 Pt 1(Pt 1):1-16.

124. Bykov VJN, Eriksson SE, Bianchi J, Wiman KG. Targeting mutant p53 for efficient cancer therapy. *Nat Rev Cancer*. 2018;18(2):89-102. doi:10.1038/nrc.2017.109

125. Bieging KT, Mello SS, Attardi LD. Unravelling mechanisms of p53-mediated tumour suppression. *Nat Rev Cancer*. 2014;14(5):359-370. doi:10.1038/nrc3711

126. Chu B, Kon N, Chen D, et al. ALOX12 is required for p53-mediated tumour suppression through a distinct ferroptosis pathway. *Nat Cell Biol*. 2019;21(5):579-591. doi:10.1038/s41556-019-0305-6

127. Lei G, Zhang Y, Hong T, et al. Ferroptosis as a mechanism to mediate p53 function in tumor radiosensitivity. *Oncogene*. 2021;40(20):3533-3547. doi:10.1038/s41388-021-01790-w

128. Wang Y, Yang L, Zhang X, et al. Epigenetic regulation of ferroptosis by H2B monoubiquitination and p53. *EMBO Rep*. 2019;20(7):e47563. doi:10.15252/embr.201847563

129. Ou Y, Wang S-J, Li D, Chu B, Gu W. Activation of SAT1 engages polyamine metabolism with p53-mediated ferroptotic responses. *Proc Natl Acad Sci USA*. 2016;113(44):E6806-E6812. doi:10.1073/pnas.1607152113

130. Zhang Y, Qian Y, Zhang J, et al. Ferredoxin reductase is critical for p53-dependent tumor suppression via iron regulatory protein 2. *Genes Dev*. 2017;31(12):1243-1256. doi:10.1101/gad.299388.117

131. Jennis M, Kung C-P, Basu S, et al. An African-specific polymorphism in the TP53 gene impairs p53 tumor suppressor function in a mouse model. *Genes Dev*. 2016;30(8):918-930. doi:10.1101/gad.275891.115

132. Wang S-J, Li D, Ou Y, et al. Acetylation Is Crucial for p53-Mediated Ferroptosis and Tumor Suppression. *Cell Rep*. 2016;17(2):366-373. doi:10.1016/j.celrep.2016.09.022

133. Tarangelo A, Magtanong L, Bieging-Rolett KT, et al. p53 Suppresses Metabolic Stress-Induced Ferroptosis in Cancer Cells. *Cell Rep*. 2018;22(3):569-575. doi:10.1016/j.celrep.2017.12.077

134. Xie Y, Zhu S, Song X, et al. The tumor suppressor p53 limits ferroptosis by blocking DPP4 activity. *Cell Rep*. 2017;20(7):1692-1704. doi:10.1016/j.celrep.2017.07.055

135. Carbone M, Yang H, Pass HI, Krausz T, Testa JR, Gaudino G. BAP1 and cancer. *Nat Rev Cancer*. 2013;13(3):153-159. doi:10.1038/nrc3459

136. Ventii KH, Devi NS, Friedrich KL, et al. BRCA1-associated protein-1 is a tumor suppressor that requires deubiquitinating activity and nuclear localization. *Cancer Res*. 2008;68(17):6953-6962. doi:10.1158/0008-5472.CAN-08-0365

137. Carbone M, Harbour JW, Brugarolas J, et al. Biological mechanisms and clinical significance of BAP1 mutations in human cancer. *Cancer Discov*. 2020;10(8):1103-1120. doi:10.1158/2159-8290.CD-19-1220

138. Cancer Genome Atlas Research Network. Comprehensive genomic characterization of squamous cell lung cancers. *Nature*. 2012;489(7417):519-525. doi:10.1038/nature11404

139. Cancer Genome Atlas Research Network. Comprehensive molecular profiling of lung adenocarcinoma. *Nature*. 2014;511(7511):543-550. doi:10.1038/nature13385

140. Baird L, Yamamoto M. The Molecular Mechanisms Regulating the KEAP1-NRF2 Pathway. *Mol Cell Biol*. 2020;40(13). doi:10.1128/MCB.00099-20

141. Kensler TW, Wakabayashi N, Biswal S. Cell survival responses to environmental stresses via the Keap1-Nrf2-ARE pathway. *Annu Rev Pharmacol Toxicol*. 2007;47:89-116. doi:10.1146/annurev.pharmtox.46.120604.141046

142. Dodson M, Castro-Portuguez R, Zhang DD. NRF2 plays a critical role in mitigating lipid peroxidation and ferroptosis. *Redox Biol*. 2019;23:101107. doi:10.1016/j.redox.2019.101107

143. Sasaki H, Sato H, Kuriyama-Matsumura K, et al. Electrophile response element-mediated induction of the cystine/glutamate exchange transporter gene expression. *J Biol Chem*. 2002;277(47):44765-44771. doi:10.1074/jbc.M208704200

144. Koppula P, Lei G, Zhang Y, et al. A targetable CoQ-FSP1 axis drives ferroptosis- and radiation-resistance in KEAP1 inactive lung cancers. *Nat Commun*. 2022;13(1):2206. doi:10.1038/s41467-022-29905-1

145. Wu W, Li D, Feng X, et al. A pan-cancer study of selenoprotein genes as promising targets for cancer therapy. *BMC Med Genomics*. 2021;14(1):78. doi:10.1186/s12920-021-00930-1

146. Ubellacker JM, Tasdogan A, Ramesh V, et al. Lymph protects metastasizing melanoma cells from ferroptosis. *Nature*. 2020;585(7823):113-118. doi:10.1038/s41586-020-2623-z

147. Chen L, Na R, Danae McLane K, et al. Overexpression of ferroptosis defense enzyme Gpx4 retards motor neuron disease of SOD1G93A mice. *Sci Rep*. 2021;11(1):12890. doi:10.1038/s41598-021-92369-8

148. Wang T, Tomas D, Perera ND, et al. Ferroptosis mediates selective motor neuron death in amyotrophic lateral sclerosis. *Cell Death Differ*. 2022;29(6):1187-1198. doi:10.1038/s41418-021-00910-z

149. Southon A, Szostak K, Acevedo KM, et al. CuII (atsm) inhibits ferroptosis: Implications for treatment of neurodegenerative disease. *Br J Pharmacol*. 2020;177(3):656-667. doi:10.1111/bph.14881

150. Tan S, Schubert D, Maher P. Oxytosis: A novel form of programmed cell death. *Curr Top Med Chem*. 2001;1(6):497-506. doi:10.2174/1568026013394741

151. Jiang X, Stockwell BR, Conrad M. Ferroptosis: mechanisms, biology and role in disease. *Nat Rev Mol Cell Biol*. 2021;22(4):266-282. doi:10.1038/s41580-020-00324-8

152. Albrecht P, Lewerenz J, Dittmer S, Noack R, Maher P, Methner A. Mechanisms of oxidative glutamate toxicity: the glutamate/cystine antiporter system xc- as a neuroprotective drug target. *CNS Neurol Disord Drug Targets*. 2010;9(3):373-382. doi:10.2174/187152710791292567

153. Hadian K, Stockwell BR. A roadmap to creating ferroptosis-based medicines. *Nat Chem Biol*. 2021;17(11):1113-1116. doi:10.1038/s41589-021-00853-z

154. Kobayashi S, Harada Y, Homma T, Yokoyama C, Fujii J. Characterization of a rat monoclonal antibody raised against ferroptotic cells. *J Immunol Methods*. 2021;489:112912. doi:10.1016/j.jim.2020.112912

155. Zheng H, Jiang L, Tsuduki T, Conrad M, Toyokuni S. Embryonal erythropoiesis and aging exploit ferroptosis. *Redox Biol*. 2021;48:102175. doi:10.1016/j.redox.2021.102175

156. Yamada S, Kumazawa S, Ishii T, et al. Immunochemical detection of a lipofuscin-like fluorophore derived from malondialdehyde and lysine. *J Lipid Res*. 2001;42(8):1187-1196. doi:10.1016/S0022-2275(20)31568-6

157. Feng H, Schorpp K, Jin J, et al. Transferrin receptor is a specific ferroptosis marker. *Cell Rep*. 2020;30(10):3411-3423.e7. doi:10.1016/j.celrep.2020.02.049

158. Jin J, Schorpp K, Samaga D, Unger K, Hadian K, Stockwell BR. Machine Learning Classifies Ferroptosis and Apoptosis Cell Death Modalities with TfR1 Immunostaining. *ACS Chem Biol*. 2022;17(3):654-660. doi:10.1021/acschembio.1c00953

159. Zilka O, Shah R, Li B, et al. On the Mechanism of Cytoprotection by Ferrostatin-1 and Liproxstatin-1 and the Role of Lipid Peroxidation in Ferroptotic Cell Death. *ACS Cent Sci*. 2017;3(3):232-243. doi:10.1021/acscentsci.7b00028

160. Friedmann Angeli JP, Schneider M, Proneth B, et al. Inactivation of the ferroptosis regulator Gpx4 triggers acute renal failure in mice. *Nat Cell Biol*. 2014;16(12):1180-1191. doi:10.1038/ncb3064

161. Carlson BA, Tobe R, Yefremova E, et al. Glutathione peroxidase 4 and vitamin E cooperatively prevent hepatocellular degeneration. *Redox Biol*. 2016;9:22-31. doi:10.1016/j.redox.2016.05.003

162. Bueno DC, Canto RFS, de Souza V, et al. New probucol analogues inhibit ferroptosis, improve mitochondrial parameters, and induce glutathione peroxidase in HT22 cells. *Mol Neurobiol*. 2020;57(8):3273-3290. doi:10.1007/s12035-020-01956-9

163. Takahashi N, Duprez L, Grootjans S, et al. Necrostatin-1 analogues: critical issues on the specificity, activity and in vivo use in experimental disease models. *Cell Death Dis*. 2012;3(11):e437. doi:10.1038/cddis.2012.176

164. Alim I, Caulfield JT, Chen Y, et al. Selenium drives a transcriptional adaptive program to block ferroptosis and treat stroke. *Cell*. 2019;177(5):1262-1279.e25. doi:10.1016/j.cell.2019.03.032

165. Krainz T, Gaschler MM, Lim C, Sacher JR, Stockwell BR, Wipf P. A Mitochondrial-Targeted Nitroxide Is a Potent Inhibitor of Ferroptosis. *ACS Cent Sci*. 2016;2(9):653-659. doi:10.1021/acscentsci.6b00199

166. Zhang Y, Tan H, Daniels JD, et al. Imidazole ketone erastin induces ferroptosis and slows tumor growth in a mouse lymphoma model. *Cell Chem Biol*. 2019;26(5):623-633.e9. doi:10.1016/j.chembiol.2019.01.008

167. Badgley MA, Kremer DM, Maurer HC, et al. Cysteine depletion induces pancreatic tumor ferroptosis in mice. *Science*. 2020;368(6486):85-89. doi:10.1126/science.aaw9872

168. Kremer DM, Nelson BS, Lin L, et al. GOT1 inhibition promotes pancreatic cancer cell death by ferroptosis. *Nat Commun*. 2021;12(1):4860. doi:10.1038/s41467-021-24859-2

169. Takahashi N, Cho P, Selfors LM, et al. 3D Culture Models with CRISPR Screens Reveal Hyperactive NRF2 as a Prerequisite for Spheroid Formation via Regulation of Proliferation and Ferroptosis. *Mol Cell*. 2020;80(5):828-844.e6. doi:10.1016/j.molcel.2020.10.010

170. Lei G, Zhang Y, Koppula P, et al. The role of ferroptosis in ionizing radiation-induced cell death and tumor suppression. *Cell Res*. 2020;30(2):146-162. doi:10.1038/s41422-019-0263-3

171. Ye LF, Chaudhary KR, Zandkarimi F, et al. Radiation-Induced Lipid Peroxidation Triggers Ferroptosis and Synergizes with Ferroptosis Inducers. *ACS Chem Biol*. 2020;15(2):469-484. doi:10.1021/acschembio.9b00939

172. Wang W, Green M, Choi JE, et al. CD8+ T cells regulate tumour ferroptosis during cancer immunotherapy. *Nature*. 2019;569(7755):270-274. doi:10.1038/s41586-019-1170-y

173. Hangauer MJ, Viswanathan VS, Ryan MJ, et al. Drug-tolerant persister cancer cells are vulnerable to GPX4 inhibition. *Nature*. 2017;551(7679):247-250. doi:10.1038/nature24297

174. Song K, Minami JK, Huang A, et al. Plasticity of extrachromosomal and intrachromosomal BRAF amplifications in overcoming targeted therapy dosage challenges. *Cancer Discov*. 2022;12(4):1046-1069. doi:10.1158/2159-8290.CD-20-0936

175. Wang F, Graham ET, Naowarojna N, et al. PALP: A rapid imaging technique for stratifying ferroptosis sensitivity in normal and tumor tissues in situ. *Cell Chem Biol*. 2022;29(1):157-170.e6. doi:10.1016/j.chembiol.2021.11.001

176. Wu J, Minikes AM, Gao M, et al. Intercellular interaction dictates cancer cell ferroptosis via NF2-YAP signalling. *Nature*. 2019;572(7769):402-406. doi:10.1038/s41586-019-1426-6

177. Lee J-Y, Nam M, Son HY, et al. Polyunsaturated fatty acid biosynthesis pathway determines ferroptosis sensitivity in gastric cancer. *Proc Natl Acad Sci USA*. 2020;117(51):32433-32442. doi:10.1073/pnas.2006828117

178. Venkatesh D, O'Brien NA, Zandkarimi F, et al. MDM2 and MDMX promote ferroptosis by PPARα-mediated lipid remodeling. *Genes Dev*. 2020;34(7-8):526-543. doi:10.1101/gad.334219.119

179. Wu M, Xu L-G, Li X, Zhai Z, Shu H-B. AMID, an apoptosis-inducing factor-homologous mitochondrion-associated protein, induces caspase-independent apoptosis. *J Biol Chem*. 2002;277(28):25617-25623. doi:10.1074/jbc.M202285200

180. Ohiro Y, Garkavtsev I, Kobayashi S, et al. A novel p53-inducible apoptogenic gene, PRG3, encodes a homologue of the apoptosis-inducing factor (AIF). *FEBS Lett*. 2002;524(1-3):163-171. doi:10.1016/s0014-5793(02)03049-1

181. Bersuker K, Peterson CWH, To M, et al. A Proximity Labeling Strategy Provides Insights into the Composition and Dynamics of Lipid Droplet Proteomes. *Dev Cell*. 2018;44(1):97-112.e7. doi:10.1016/j.devcel.2017.11.020

182. Yang WS, Kim KJ, Gaschler MM, Patel M, Shchepinov MS, Stockwell BR. Peroxidation of polyunsaturated fatty acids by lipoxygenases drives ferroptosis. *Proc Natl Acad Sci USA*. 2016;113(34):E4966-75. doi:10.1073/pnas.1603244113

183. Marshall KR, Gong M, Wodke L, et al. The human apoptosis-inducing protein AMID is an oxidoreductase with a modified flavin cofactor and DNA binding activity. *J Biol Chem*. 2005;280(35):30735-30740. doi:10.1074/jbc.M414018200

184. Arroyo A, Navarro F, Navas P, Villalba JM. Ubiquinol regeneration by plasma membrane ubiquinone reductase. *Protoplasma*. 1998;205(1-4):107-113. doi:10.1007/BF01279300

185. Rees MG, Seashore-Ludlow B, Cheah JH, et al. Correlating chemical sensitivity and basal gene expression reveals mechanism of action. *Nat Chem Biol*. 2016;12(2):109-116. doi:10.1038/nchembio.1986

186. Nguyen TB, Louie SM, Daniele JR, et al. DGAT1-Dependent Lipid Droplet Biogenesis Protects Mitochondrial Function during Starvation-Induced Autophagy. *Dev Cell*. 2017;42(1):9-21.e5. doi:10.1016/j.devcel.2017.06.003

187. Tribble DL, van den Berg JJ, Motchnik PA, et al. Oxidative susceptibility of low density lipoprotein subfractions is related to their ubiquinol-10 and alpha-tocopherol content. *Proc Natl Acad Sci USA*. 1994;91(3):1183-1187. doi:10.1073/pnas.91.3.1183

188. Stocker R, Bowry VW, Frei B. Ubiquinol-10 protects human low density lipoprotein more efficiently against lipid peroxidation than does alpha-tocopherol. *Proc Natl Acad Sci USA*. 1991;88(5):1646-1650. doi:10.1073/pnas.88.5.1646

189. Stevenson J, Krycer JR, Phan L, Brown AJ. A practical comparison of ligation-independent cloning techniques. *PLoS ONE*. 2013;8(12):e83888. doi:10.1371/journal.pone.0083888

190. Inoue T, Heo WD, Grimley JS, Wandless TJ, Meyer T. An inducible translocation strategy to rapidly activate and inhibit small GTPase signaling pathways. *Nat Methods*. 2005;2(6):415-418. doi:10.1038/nmeth763

191. Macdonald JL, Pike LJ. A simplified method for the preparation of detergent-free lipid rafts. *J Lipid Res*. 2005;46(5):1061-1067. doi:10.1194/jlr.D400041-JLR200

192. Morgens DW, Deans RM, Li A, Bassik MC. Systematic comparison of CRISPR/Cas9 and RNAi screens for essential genes. *Nat Biotechnol*. 2016;34(6):634-636. doi:10.1038/nbt.3567

193. Morgens DW, Wainberg M, Boyle EA, et al. Genome-scale measurement of off-target activity using Cas9 toxicity in high-throughput screens. *Nat Commun*. 2017;8:15178. doi:10.1038/ncomms15178

194. Leto DE, Morgens DW, Zhang L, et al. Genome-wide CRISPR Analysis Identifies Substrate-Specific Conjugation Modules in ER-Associated Degradation. *Mol Cell*. 2019;73(2):377-389.e11. doi:10.1016/j.molcel.2018.11.015

195. Unable to find information for 2859933.

196. Tang PH, Miles MV, DeGrauw A, Hershey A, Pesce A. HPLC analysis of reduced and oxidized coenzyme Q(10) in human plasma. *Clin Chem*. 2001;47(2):256-265. doi:10.1093/clinchem/47.2.256

197. Mao C, Liu X, Zhang Y, et al. DHODH-mediated ferroptosis defence is a targetable vulnerability in cancer. *Nature*. 2021;593(7860):586-590. doi:10.1038/s41586-021-03539-7

198. Barayeu U, Schilling D, Eid M, et al. Hydropersulfides inhibit lipid peroxidation and ferroptosis by scavenging radicals. *Nat Chem Biol*. 2023;19(1):28-37. doi:10.1038/s41589-022-01145-w

199. Wu Z, Khodade VS, Chauvin J-PR, Rodriguez D, Toscano JP, Pratt DA. Hydropersulfides Inhibit Lipid Peroxidation and Protect Cells from Ferroptosis. *J Am Chem Soc*. 2022;144(34):15825-15837. doi:10.1021/jacs.2c06804

200. Anandhan A, Dodson M, Schmidlin CJ, Liu P, Zhang DD. Breakdown of an ironclad defense system: the critical role of NRF2 in mediating ferroptosis. *Cell Chem Biol*. 2020;27(4):436-447. doi:10.1016/j.chembiol.2020.03.011

201. Labrie M, Brugge JS, Mills GB, Zervantonakis IK. Therapy resistance: opportunities created by adaptive responses to targeted therapies in cancer. *Nat Rev Cancer*. 2022;22(6):323-339. doi:10.1038/s41568-022-00454-5

202. Rodriguez R, Schreiber SL, Conrad M. Persister cancer cells: Iron addiction and vulnerability to ferroptosis. *Mol Cell*. 2022;82(4):728-740. doi:10.1016/j.molcel.2021.12.001

203. Zhang L, Hobeika CS, Khabibullin D, et al. Hypersensitivity to ferroptosis in chromophobe RCC is mediated by a glutathione metabolic dependency and cystine import via solute carrier family 7 member 11. *Proc Natl Acad Sci USA*. 2022;119(28):e2122840119. doi:10.1073/pnas.2122840119

204. Timmerman LA, Holton T, Yuneva M, et al. Glutamine sensitivity analysis identifies the xCT antiporter as a common triple-negative breast tumor therapeutic target. *Cancer Cell*. 2013;24(4):450-465. doi:10.1016/j.ccr.2013.08.020

205. Alborzinia H, Flórez AF, Kreth S, et al. MYCN mediates cysteine addiction and sensitizes neuroblastoma to ferroptosis. *Nat Cancer*. 2022;3(4):471-485. doi:10.1038/s43018-022-00355-4

206. Alborzy H, Chen Z, Yildiz U, et al. Selenocysteine metabolism is a targetable vulnerability in MYCN-amplified cancers. *BioRxiv*. May 18, 2022. doi:10.1101/2022.05.17.492172

207. Floros KV, Cai J, Jacob S, et al. MYCN-Amplified Neuroblastoma Is Addicted to Iron and Vulnerable to Inhibition of the System Xc-/Glutathione Axis. *Cancer Res*. 2021;81(7):1896-1908. doi:10.1158/0008-5472.CAN-20-1641

208. Lu Y, Yang Q, Su Y, et al. MYCN mediates TFRC-dependent ferroptosis and reveals vulnerabilities in neuroblastoma. *Cell Death Dis*. 2021;12(6):511. doi:10.1038/s41419-021-03790-w

209. Stockwell BR, Jiang X. The chemistry and biology of ferroptosis. *Cell Chem Biol*. 2020;27(4):365-375. doi:10.1016/j.chembiol.2020.03.013

210. Rojo de la Vega M, Chapman E, Zhang DD. NRF2 and the hallmarks of cancer. *Cancer Cell*. 2018;34(1):21-43. doi:10.1016/j.ccell.2018.03.022

211. Sporn MB, Liby KT. NRF2 and cancer: the good, the bad and the importance of context. *Nat Rev Cancer*. 2012;12(8):564-571. doi:10.1038/nrc3278

212. Forcina GC, Conlon M, Wells A, Cao JY, Dixon SJ. Systematic quantification of population cell death kinetics in mammalian cells. *Cell Syst*. 2017;4(6):600-610.e6. doi:10.1016/j.cels.2017.05.002

213. Yang W-H, Ding C-KC, Sun T, et al. The hippo pathway effector TAZ regulates ferroptosis in renal cell carcinoma. *Cell Rep*. 2019;28(10):2501-2508.e4. doi:10.1016/j.celrep.2019.07.107

214. Unger C, Kramer N, Walzl A, Scherzer M, Hengstschläger M, Dolznig H. Modeling human carcinomas: physiologically relevant 3D models to improve anti-cancer drug development. *Adv Drug Deliv Rev*. 2014;79-80:50-67. doi:10.1016/j.addr.2014.10.015

215. Krishna S, Bustamante L, Haynes RK, Staines HM. Artemisinins: their growing importance in medicine. *Trends Pharmacol Sci*. 2008;29(10):520-527. doi:10.1016/j.tips.2008.07.004

216. Lin R, Zhang Z, Chen L, et al. Dihydroartemisinin (DHA) induces ferroptosis and causes cell cycle arrest in head and neck carcinoma cells. *Cancer Lett*. 2016;381(1):165-175. doi:10.1016/j.canlet.2016.07.033

217. Nie J, Lin B, Zhou M, Wu L, Zheng T. Role of ferroptosis in hepatocellular carcinoma. *J Cancer Res Clin Oncol*. 2018;144(12):2329-2337. doi:10.1007/s00432-018-2740-3

218. Yi R, Wang H, Deng C, et al. Dihydroartemisinin initiates ferroptosis in glioblastoma through GPX4 inhibition. *Biosci Rep*. 2020;40(6). doi:10.1042/BSR20193314

219. Gaschler MM, Andia AA, Liu H, et al. FINO2 initiates ferroptosis through GPX4 inactivation and iron oxidation. *Nat Chem Biol*. 2018;14(5):507-515. doi:10.1038/s41589-018-0031-6

220. Ianevski A, Giri AK, Aittokallio T. SynergyFinder 2.0: visual analytics of multi-drug combination synergies. *Nucleic Acids Res*. 2020;48(W1):W488-W493. doi:10.1093/nar/gkaa216

221. Lei G, Zhuang L, Gan B. Targeting ferroptosis as a vulnerability in cancer. *Nat Rev Cancer*. 2022;22(7):381-396. doi:10.1038/s41568-022-00459-0

222. Zhu T, Shi L, Yu C, et al. Ferroptosis Promotes Photodynamic Therapy: Supramolecular Photosensitizer-Inducer Nanodrug for Enhanced Cancer Treatment. *Theranostics*. 2019;9(11):3293-3307. doi:10.7150/thno.32867

223. Liu T, Liu W, Zhang M, et al. Ferrous-Supply-Regeneration Nanoengineering for Cancer-Cell-Specific Ferroptosis in Combination with Imaging-Guided Photodynamic Therapy. *ACS Nano*. 2018;12(12):12181-12192. doi:10.1021/acsnano.8b05860

224. Chen Y-C, Oses-Prieto JA, Pope LE, Burlingame AL, Dixon SJ, Renslo AR. Reactivity-Based Probe of the Iron(II)-Dependent Interactome Identifies New Cellular Modulators of Ferroptosis. *J Am Chem Soc*. 2020;142(45):19085-19093. doi:10.1021/jacs.0c06709

225. Nguyen HP, Yi D, Lin F, et al. Aifm2, a NADH Oxidase, Supports Robust Glycolysis and Is Required for Cold- and Diet-Induced Thermogenesis. *Mol Cell*. 2020;77(3):600-617.e4. doi:10.1016/j.molcel.2019.12.002

226. Nguyen HP, Villivalam SD, Jung BC, et al. AIFM2 Is Required for High-Intensity Aerobic Exercise in Promoting Glucose Utilization. *Diabetes*. 2022;71(10):2084-2093. doi:10.2337/db21-1114

227. DeBerardinis RJ, Chandel NS. Fundamentals of cancer metabolism. *Sci Adv*. 2016;2(5):e1600200. doi:10.1126/sciadv.1600200

228. Eaton JK, Furst L, Ruberto RA, et al. Selective covalent targeting of GPX4 using masked nitrile-oxide electrophiles. *Nat Chem Biol*. 2020;16(5):497-506. doi:10.1038/s41589-020-0501-5

229. Hassannia B, Wiernicki B, Ingold I, et al. Nano-targeted induction of dual ferroptotic mechanisms eradicates high-risk neuroblastoma. *J Clin Invest*. 2018;128(8):3341-3355. doi:10.1172/JCI99032

230. Woo JH, Shimoni Y, Yang WS, et al. Elucidating compound mechanism of action by network perturbation analysis. *Cell*. 2015;162(2):441-451. doi:10.1016/j.cell.2015.05.056

231. Nakamura T, Hipp C, Santos Dias Mourão A, et al. Phase separation of FSP1 promotes ferroptosis. *Nature*. 2023;619(7969):371-377. doi:10.1038/s41586-023-06255-6

232. Mei J, Webb S, Zhang B, Shu HB. The p53-inducible apoptotic protein AMID is not required for normal development and tumor suppression. *Oncogene*. 2006;25(6):849-856. doi:10.1038/sj.onc.1209121

233. Tonnus W, Meyer C, Steinebach C, et al. Dysfunction of the key ferroptosis-surveilling systems hypersensitizes mice to tubular necrosis during acute kidney injury. *Nat Commun*. 2021;12(1):4402. doi:10.1038/s41467-021-24712-6

234. Perez MA, Magtanong L, Dixon SJ, Watts JL. Dietary lipids induce ferroptosis in caenorhabditiselegans and human cancer cells. *Dev Cell*. 2020;54(4):447-454.e4. doi:10.1016/j.devcel.2020.06.019

235. Dierge E, Debock E, Guilbaud C, et al. Peroxidation of n-3 and n-6 polyunsaturated fatty acids in the acidic tumor environment leads to ferroptosis-mediated anticancer effects. *Cell Metab*. 2021;33(8):1701-1715.e5. doi:10.1016/j.cmet.2021.05.016

236. Kagan VE, Bayir HA, Belikova NA, et al. Cytochrome c/cardiolipin relations in mitochondria: a kiss of death. *Free Radic Biol Med*. 2009;46(11):1439-1453. doi:10.1016/j.freeradbiomed.2009.03.004

237. Greenberg ME, Sun M, Zhang R, Febbraio M, Silverstein R, Hazen SL. Oxidized phosphatidylserine-CD36 interactions play an essential role in macrophage-dependent phagocytosis of apoptotic cells. *J Exp Med*. 2006;203(12):2613-2625. doi:10.1084/jem.20060370

238. Tyurin VA, Balasubramanian K, Winnica D, et al. Oxidatively modified phosphatidylserines on the surface of apoptotic cells are essential phagocytic “eat-me” signals: cleavage and inhibition of phagocytosis by Lp-PLA2. *Cell Death Differ*. 2014;21(5):825-835. doi:10.1038/cdd.2014.1

239. Pettersson M, Crews CM. PROteolysis TArgeting Chimeras (PROTACs) - Past, present and future. *Drug Discov Today Technol*. 2019;31:15-27. doi:10.1016/j.ddtec.2019.01.002

240. Ding Y, Fei Y, Lu B. Emerging new concepts of degrader technologies. *Trends Pharmacol Sci*. 2020;41(7):464-474. doi:10.1016/j.tips.2020.04.005 Sciwheel inserting bibliography...